Nanostructured Thermoelectric Oxides for Energy Harvesting Applications

Dissertation by:

Anas Ibrahim Abutaha

In Partial Fulfillment of the Requirements for the Degree of

DOCTOR OF PHILOSOPHY

King Abdullah University of Science and Technology

Thuwal, Kingdom of Saudi Arabia

March 2015

The dissertation of Anas Ibrahim Abutaha is approved by the examination committee.

Committee Chairperson [Prof. Husam Alshareef]

Committee Member [Prof. Xixiang Zhang]

Committee Member [Prof. Boon Ooi]

Committee Member [Prof. Udo Schwingenshlogl]

Committee Member [Dr. Aurelien Manchon]

ABSTRACT

Nanostructured Thermoelectric Oxides for Energy Harvesting Applications

Anas Ibrahim Abutaha

As the world strives to adapt to the increasing demand for electrical power, sustainable energy sources are attracting significant interest. Around 60% of energy utilized in the world is wasted as heat. Different industrial processes, home heating, and exhausts in cars, all generate a huge amount of unused waste heat. With such a huge potential, there is also significant interest in discovering inexpensive technologies for power generation from waste heat. As a result, thermoelectric materials have become important for many renewable energy research programs. While significant advancements have been done in improving the thermoelectric properties of the conventional heavy-element based materials (such as Bi_2Te_3 *and PbTe), high-temperature applications of thermoelectrics are still limited to one materials system, namely SiGe, since the traditional thermoelectric materials degrade and oxidize at high temperature. Therefore, oxide thermoelectrics emerge as a promising class of materials since they can operate at higher temperatures and in harsher environments compared to non-oxide thermoelectrics. Furthermore, oxides are abundant and friendly to the environment. Among oxides, crystalline* $SrTiO_3$ *and ZnO are promising thermoelectric materials.*

The main objective of this work is therefore to pursue focused investigations of $SrTiO_3$ *and ZnO thin films and superlattices grown by pulsed laser deposition (PLD), with the goal of optimizing their thermoelectric properties by following different strategies.*

First, the effect of laser fluence on the thermoelectric properties of La doped epitaxial $SrTiO_3$ *films is discussed. Films grown at higher laser fluences exhibit better thermoelectric performance. Second, the role of crystal orientation in determining the thermoelectric properties of epitaxial Al doped ZnO (AZO) films is explained. Vertically aligned (c-axis) AZO films have superior thermoelectric properties compared to other films with different crystal orientations. Third, additional B-site doping of A-site doped* $SrTiO_3$ *films leads to a prominent reduction in the lattice thermal conductivity without limiting the electrical transport, and hence an improvement in the figure of merit is noticed. Fourth and last, the enhancement of thermoelectric properties of thermally robust, high quality* $SrTiO_3$*-based superlattices is discussed. Beside the randomly distributed oxygen vacancies and extrinsic dopants, the structure of* $SrTiO_3$*-based superlattices increases the scattering of phonons at the interfaces between the alternative layers, and hence reducing the thermal conductivity, which leads to a notable enhancement in the figure of merit.*

ACKNOWLEDGEMENTS

"In the Name of Allah, the Most Gracious, the Most Merciful"

I would like to express my sincere gratitude to my advisor Prof. Husam N. Alshareef for this precious opportunity and letting me work under his supervision. Joining his Functional Nanomaterials and Devices Lab at King Abdullah University of Science and Technology (KAUST) is one of the best things that have happened to me. I really appreciate his endless support and kind guidance during my PhD research.

I would like also to express my gratitude to Dr. S.R. Sarath Kumar who also mentored me during my research. I would like to thank him for giving me the opportunity of learning from him, from his expertise, and knowledge. I will not forget many discussions and conversions, which lead to better understanding and learning. My appreciation also goes to my friends and colleagues at the Functional Nanomaterials and Devices Laboratory, and the core Laboratories at KAUST. I would also like to express my gratitude and appreciation to my committee members, Prof. Xixiang Zhang, Prof. Udo Schwingenshlogl, Prof. Boon Ooi, and Dr. Aurelien Munchon for their valuable time.

Words cannot describe how grateful I am for my parents, Suad Herbawi and Ibrahim Abutaha. After Allah's Endless Grace, all what I have today would not have been possible without their prayers, love, support, and sacrifice. Last but not least, my hearty gratitude goes to my better half, my wife, Tala Abu-Ghazaleh, for her patience, understanding, and support during my PhD study.

TABLE OF CONTENTS

LIST OF ABBREVIATIONS

AFM	Atomic Force Microscope
AZO	Al doped ZnO
FWHM	Full Width at Half Maximum
LAO	$LaAlO_3$
MFC	Mass Flow Controller
PF	Power Factor
PLD	Pulsed Laser Deposition
PPMS	Physical Properties Measurement System
PVD	Physical Vapor Deposition
rpm	round per minute
sccm	standard cubic centimeters per minute
SEM	Scanning Electron Microscope
SLs	Superlattices
SLTNO	La and Nb doped $SrTiO_3$
SLTO	La doped $SrTiO_3$
SPTNO	Pr and Nb doped $SrTiO_3$
SPTO	Pr doped $SrTiO_3$
STNO	Nb doped $SrTiO_3$
STO	$SrTiO_3$ (Strontium Titanate)
TE	Thermoelectric
TEs	Thermoelectrics

TEM	Transmission Electron Microscope
UV	Ultraviolet
XRD	X-ray Diffraction

LIST OF ILLUSTRATIONS

Chapter 1.

Introduction

The huge increase in the global energy consumption, and the negative effects on environment caused by many current energy conversion technologies, have led to significant research interests in developing alternative energy conversion systems. One of the untapped, low-cost, and sustainable energy sources is heat. More than half of the primary energy utilized in many areas is wasted in form of heat. Thermoelectric (TE) devices can be used to convert waste heat into useful electrical power with no harmful emissions compared to traditional power generators, which operate on fossil fuel. Furthermore, TE devices have long lifetime, no moving parts, reliable use, and low operation cost. Potential applications include recovery of waste heat from power plants, industrial processes, melting furnaces, engine exhaust streams, space applications, and many others.

So far, TE devices have been fabricated by utilizing heavy metal alloys, such as Bi_2Te_3 and PbTe, due to their relatively high efficiencies. However, these materials are composed of toxic, naturally rare, and heavy elements and can melt or be oxidized at high temperatures in air. Therefore, these materials can be used in limited environments, such as deep space exploration missions. To overcome these challenges, alternative TE materials should be explored. Metal oxides represent a promising solution from this point of view.

Metal oxides are considered as interesting candidates for high-temperature TE applications due to their stability, lack of toxicity, and low cost. Furthermore, by doping these oxides, high electrical conductivity and Seebeck coefficient can be obtained compared to traditional TE materials. Nevertheless, oxides are known with their relatively high lattice thermal conductivity due to the strong bonding between cations and anions, and the small mass of oxygen. So, the real challenge that encounters researchers in oxide TEs is to reduce the lattice thermal conductivity of oxides without deteriorating their decent electrical transport.

The main objective of this research work is to understand the TE properties of *n*-type metal oxides, namely $SrTiO_3$ (STO) and ZnO thin films and superlattices (SLs), and to discover different approaches for optimizing the TE performance. All films and SLs are studied by several characterization tools in order to explore their crystal structures, and to interpret their related TE properties accordingly.

The dissertation is organized as follows:

Chapter 2. Theoretical background and recent progress in TEs are presented. The chapter presents the definition of TE figure of merit (*ZT*). Fundamentals of electrical and thermal transports are discussed in this chapter. Introduction to crystal and electronic band structures of STO and ZnO is presented. The chapter concludes with the recent progress achieved in state-of-the-art TE materials, as well as comprehensive reviews on best reported *ZT* values for STO and ZnO based materials.

Chapter 3. This chapter discusses the experimental procedures used in the fabrication and characterization of thin films and SLs. The operation principles of the experimental setup used for measuring the electrical conductivity and Seebeck coefficient are also discussed. The chapter presents also the 3ω method used for measuring the thermal conductivity of the specimens. Finally, the characterization techniques used in this work are reviewed.

Chapter 4. The effect of the laser fluence on high-temperature thermoelectric properties of the La^{3+} doped $SrTiO_3$ (SLTO) thin films is clarified. In this chapter, it is confirmed that films are epitaxially grown on the substrate. Furthermore, it is shown that oxygen vacancies can be tuned by varying the fluence of the ablating laser. Depending on the measured physical properties, the oxygen vacancies play a vital role in determining the thermoelectric properties of the films. Film grown at the highest laser fluence shows the best TE properties.

Chapter 5. This chapter shows how the thermoelectric properties of highly oriented Al^{3+} doped zinc oxide (AZO) thin films can be improved by controlling their crystal orientation. The crystal orientation of the AZO films can be changed by changing the temperature of the laser deposition process on $LaAlO_3$ <001> substrates. The change in surface termination of the $LaAlO_3$ substrate with temperature controls the orientation of AZO films. The anisotropic nature of electrical conductivity and Seebeck coefficient of the AZO films shows a favored thermoelectric performance in c-axis oriented films.

Chapter 6. The chapter demonstrates that the thermoelectric properties of epitaxial strontium titanate (STO) thin films can be improved by additional B-site doping of A-site doped STO. The additional B-site doping results in increased electrical conductivity, but at the expense of Seebeck coefficient. However, doping on both sites of the STO lattice significantly reduces the lattice thermal conductivity of STO by adding more densely and strategically distributed phononic scattering centers that attack a wider phonon spectra. The additional B-site doping limits the trade-off relationship between electrical conductivity and total thermal conductivity of A-site doped STO, leading to an improvement in room-temperature thermoelectric figure of merit, ZT.

Chapter 7. This chapter discusses the TE properties of metal oxide superlattices, composed from alternative layers of Pr^{3+} doped $SrTiO_{3-\delta}$ (SPTO) and Nb^{5+} doped $SrTiO_{3-\delta}$ (STNO). Excellent stability is established for these superlattices by maintaining the crystal structure and reproducing the TE properties after long-time (20 hours) annealing at high temperature (~1000 K). The introduction of oxygen vacancies as well as extrinsic dopants (Pr^{3+} and Nb^{5+}), with different masses and ionic radii, at different lattice sites in SPTO and STNO layers, respectively, results in a substantial reduction of thermal conductivity via scattering a wider range of phonon spectrum without limiting the electrical transport and thermopower, and hence leading to an enhancement in ZT.

Chapter 8. The main conclusions, remaining challenges, and future perspectives for optimizing the TE properties of oxide thin films are addressed in this chapter.

Chapter 2.

Theoretical Background and Literature Review

2.1. Thermoelectric Effects

The most fundamental phenomenon in thermoelectricity is the *Seebeck effect*. In 1821, Thomas Seebeck observed that a compass needle would be deflected by two different metals joined at two different places in a closed loop, with a temperature difference between the junctions, due to a flowing current in the loop. This effect was called later as *Seebeck effect*. In other words, if the two junctions are held at different temperatures (T and $T + \Delta T$), then the high-thermal-energy electrons flow to the colder edge (Figure 2.1(a)). This flow of electrons establishes an electric field ($\vec{E}$), and hence a voltage difference (ΔV) builds up proportional to the temperature difference (ΔT), to oppose the flowing electrons (Figure 2.1(b)) [1]. The ratio $\Delta V/\Delta T$ is related to an intrinsic property of the materials called Seebeck coefficient (S), or the thermopower. S is very low for metals (a few microvolts per degree Kelvin) and is much higher for semiconductors (a few hundred microvolts per degree Kelvin) [2].

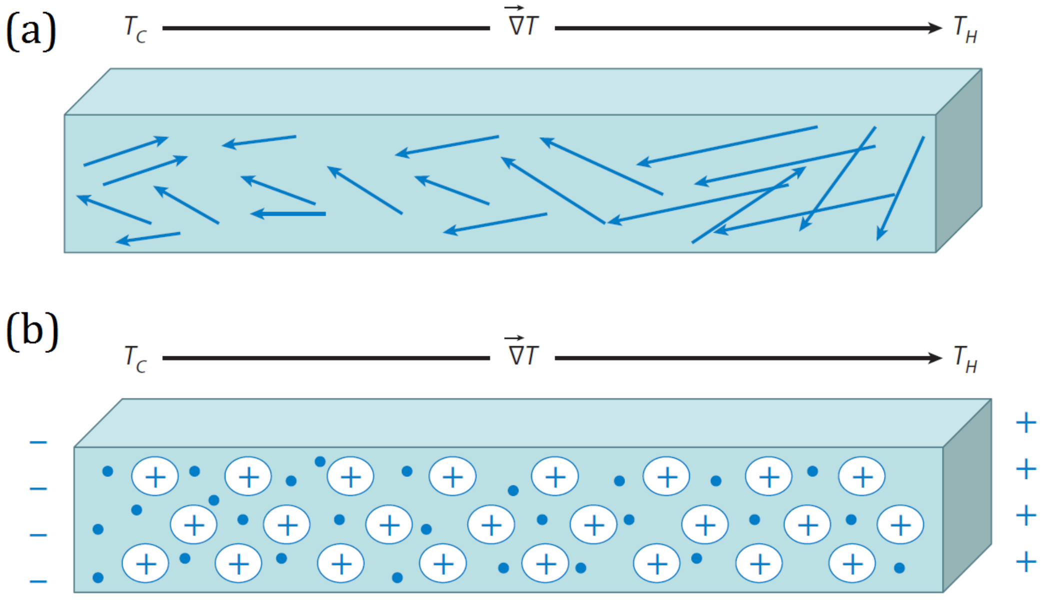

Figure 2.1. Illustrations of Seebeck effect when a material is subjected to an external temperature gradient ($\vec{\nabla}T$). (a) Longer mean free path for the more energetic electrons. (b) To oppose the diffusion of the energetic electrons, an electric field ($\vec{E}$) is developed from the hot edge (T_H) to the cold one (T_C). Since the electrons are negatively charged, $\vec{E}$ will be established in the opposite direction of $\vec{\nabla}T$, and hence S will have a negative sign as it is included in the relation: $\vec{E} = S\,\vec{\nabla}T$ [1].

The real TE device consists of a pair of *n*-type and *p*-type semiconductors connected electrically in series and thermally in parallel as shown in Figure 2.2(a) and (b). In Seebeck effect, if a thermal gradient is maintained between the two metal junctions (top and bottom), the electrons in the *n*-type leg and the holes in the *p*-type leg will diffuse to the cold junction, creating a potential difference, which can be used to power an external load (Figure 2.2(a)). On the other hand, when the same system is connected to a power supply, an electric current will flow through its legs by pushing electrons and holes from the top metal junction to the bottom one. The moving electrons and holes will carry heat away from the top junction keeping it colder than other one, and this effect is called *Peltier effect*, discovered by Jean Peltier in 1835 (Figure 2.2(b)). For each material, the cooling effect is represented by the Peltier coefficient (Π) which relates the heat carried by the charge carriers to the electrical current (I) through $Q = \Pi \times I$ [3]. In 1851, Thomson (Lord Kelvin) found the fundamental relationship between the Seebeck and Peltier coefficients by considering an experiment in which a closed-loop thermocouple is under a thermal gradient. The resulting Seebeck voltage induced currents in the circuit, and Peltier cooling at junctions should result in a self-consistent description.

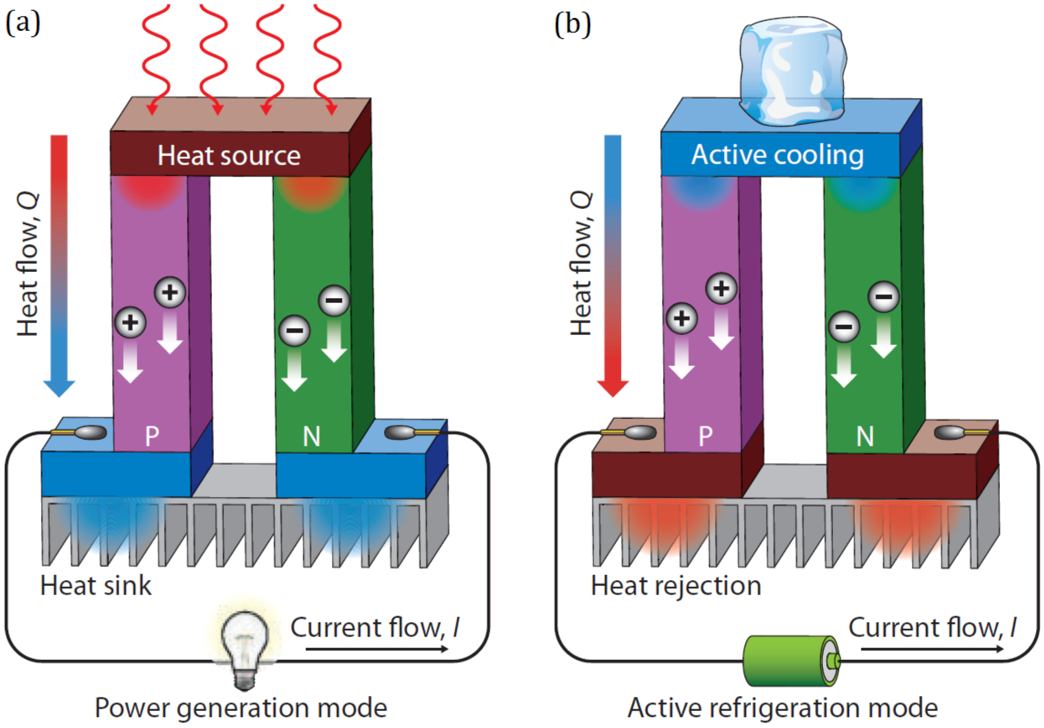

Figure 2.2. Schematic diagrams for (a) power generation mode (Seebeck effect) and (b) refrigeration mode (Peltier effect) [4].

2.2. Figure of Merit and Transport Properties

The performance of a TE material can be measured by the dimensionless figure of merit, ZT. ZT is defined by the equation [5]:

$$ZT = \frac{\sigma S^2 T}{\lambda_l + \lambda_e}, \tag{2.1}$$

where σ is the electrical conductivity, S is the Seebeck coefficient, T is the absolute temperature, and λ_l and λ_e are the lattice and electronic contributions to thermal conductivity, respectively. From the equation above, we can easily see that high ZT values can be achieved with a high S and high σ with low λ_l and λ_e. Unfortunately, all of the physical parameters that describe ZT cannot be treated independently and the correlations between them are complicated. Many researchers in the field of TE research are striving to get $ZT \geq 3$ in order to involve the TE materials in a wider range of applications. The efficiency (η) [6] of TE materials for power generation is defined as the output of electrical power (P) divided by the thermal power (Q) supplied:

$$\eta = \frac{P}{Q} = \frac{T_H - T_C}{T_H} = \frac{\sqrt{1+ZT}-1}{\sqrt{1+ZT}+\frac{T_C}{T_H}}, \tag{2.2}$$

where T_H and T_C are the temperatures of the hot and cold sides of the sample, respectively.

Figure 2.3 reviews some possible heat sources for TE applications, such as industrial waste, solar geothermal, nuclear and coal, along with the efficiency of several thermal-to-electric conversion technologies, such as organic Rankine, Kalina cycle, Stirling, Brayton and steam Rankine. Figure 2.3 states that the existing, practical mechanical systems are much more efficient than TEs. For instance, the maximum reported *ZT* [7] for *n*-type TE materials is 2.6 so far, provides less efficiency than traditional energy-conversion technologies regardless of what temperature range is of interest. Nevertheless, obtaining $ZT \geq 3$ can notably expand the range and enhance the performance of niche applications, which is an important goal that the TE community is now striving to achieve.

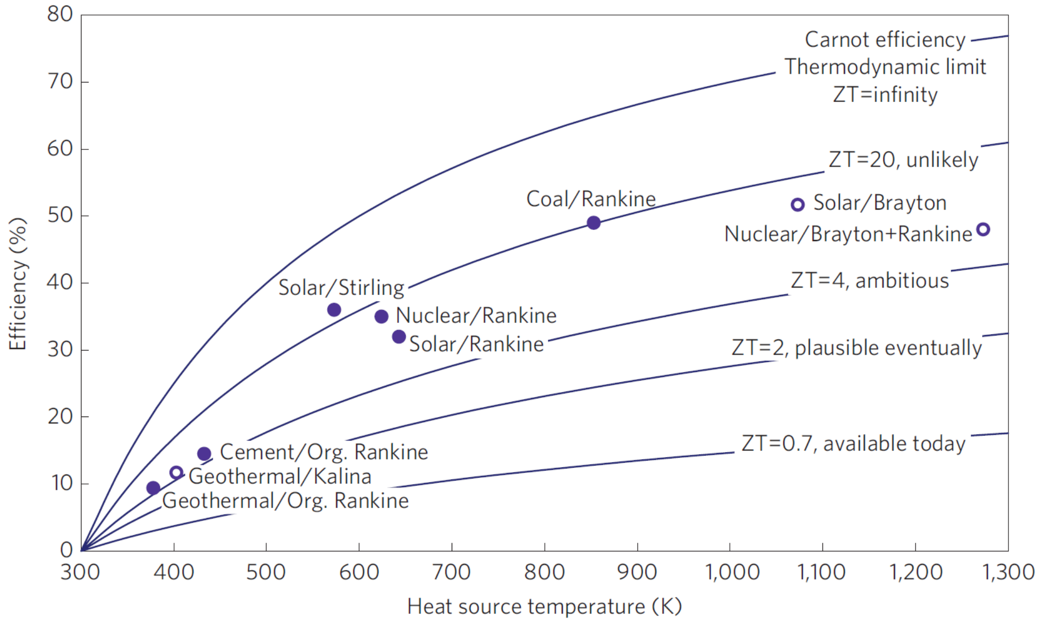

Figure 2.3. Efficiency of several heat engines compared with an estimate of TE performance at different values of *ZT* [8].

In the following sections, the optimum conditions of the physical quantities (σ, S, and λ) that describe *ZT* are discussed. It is important to note that these conditions are inferred from the best TE materials, and they can be regarded as reasonable guidelines in optimizing novel TE materials. However, due to the immanent trade-off relationship between those physical parameters, some of these guidelines are not valid for all TE materials. Several reviews published in the past decade highlighted the possible approaches for enhancing the TE performance of many materials [1, 3, 9-14].

2.2.1. Electronic Transport

Boltzmann transport theory establishes a general understanding of the electronic and thermal transport properties in a vast majority of solids by connecting between the band structure calculations and transport coefficients [15]. Applying Boltzmann transport formulas under the relaxation time approximation, the σ and S can be expressed as [3]:

$$\sigma = \int \sigma(E) \left(-\frac{\partial f}{\partial E}\right) dE, \tag{2.3}$$

$$S = -\frac{k_B}{e} \frac{\int \sigma(E) \frac{(E-E_F)}{k_B T} \left(-\frac{\partial f}{\partial E}\right) dE}{\int \sigma(E) \left(-\frac{\partial f}{\partial E}\right) dE}, \tag{2.4}$$

where the transport distribution function (differential conductivity),

$$\sigma(E) = e^2 \, \tau(E) \, v_x^2(E) \, g(E). \tag{2.5}$$

Here e is the electronic charge, E_F is Fermi energy, k_B is Boltzmann coefficient, T is the absolute temperature, v is the carrier velocity, $\tau(E)$ is the momentum relaxation time, and $g(E)$ is the density of states (DOS). $\sigma(E)$ defines the electrical conductivity of electrons with energy E to the total electrical conductivity. For metals or degenerate semiconductors, S can be approximated by Mott's formula with respect to the transport distribution function at $E=E_F$ as the following:

$$S = \frac{\pi^2 k_B^2 T}{3e} \frac{1}{\sigma(E)} \frac{d\sigma(E)}{dE}. \tag{2.6}$$

During the past decades, different approaches were proposed to suppress the strong correlation between S and σ, which provided several clues on ideal crystal and band structure for selecting the TE candidates of materials. For example, Figure 2.4(a) and (b) illustrate two hypothetical electronic DOS diagrams. In Figure 2.4(a), the DOS varies rapidly near E_F unlike the one in Figure 2.4(b) where almost no change. Based on Equation 2.6, the system in Figure 2.4 (b) with rapidly changing DOS is expected to have a larger TE power factor (*PF*). In other words, S of a material is a measure of the asymmetry of electronic structure near Fermi level.

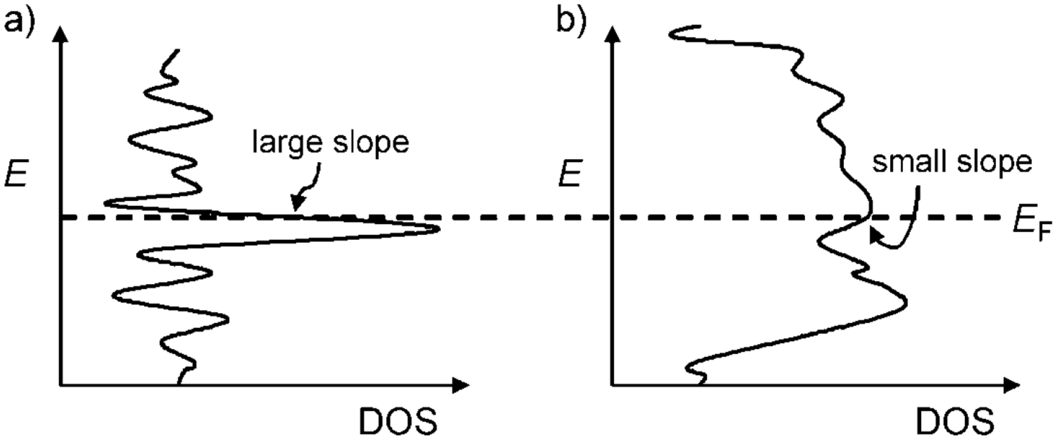

Figure 2.4. Hypothetical density of states with (a) large slope (derivative in Equation 2.6) and (b) small slope at Fermi level [13].

On the other hand, one can optimize the TE performance of a material by introducing complexities in DOS within a small energy interval (a few keV) at Fermi level. For instance, compounds with complex structures and compositions are expected to possess complex electronic structures, and hence good TE performance

[13]. Figure 2.5(a) and (b) show two examples of semiconductors having simple and complex electronic structures, respectively. It can be expected that materials with complex structures can have higher *PF* than those with simpler electronic structures at the same carrier concentration in both types. In other words, the degeneracy of band valleys needs to be high in order to have high *PF* since each band valley, if populated by electrons, contributes a certain S and σ. The presence of a huge number of such valleys in a material band structure could result in increased *ZT* because the total *PF* derives from the total contributions from all valleys [13].

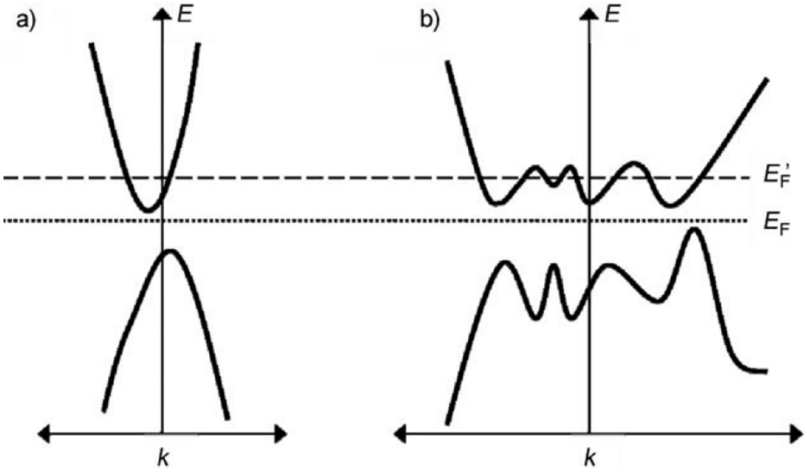

Figure 2.5. Hypothetic electronic band structures of (a) single-valley and (b) multi-valley systems. When system in (b) is n-doped, more valleys will be populated by electrons. The *PF* depends on the number of populated valleys, and hence system in (b) will have higher *PF* [13].

2.2.2. Thermal Transport

Thermal conductivity (λ) is the ability of a material to conduct heat, which has two contributions, one from the electrical charge carriers (λ_e) and the other from the lattice vibrations (λ_l). The total thermal conductivity is the summation of both contributions:

$$\lambda = \lambda_e + \lambda_l. \tag{2.7}$$

Metals possess high λ, which is attributed to the contribution of large number of electrons. Hence, λ_e has the major impact on λ in metals while λ_l has smaller effect. According to the Wiedemann-Franz relation, λ_e is proportional to σ for metals at a certain temperature ($L = 2.45\times10^{-8}$ W Ω K^{-2}) [16]:

$$\lambda_e = L\,\sigma\,T. \tag{2.8}$$

On the other hand, λ_l is given by [16]:

$$\lambda_l = \frac{1}{3}\,v_s\,C_V\,l, \tag{2.9}$$

where v_s is the velocity of sound, C_V is the specific heat at constant volume, and l is the mean free path of the phonons (quantized vibrations of lattice). In semiconductors, λ_l is usually much greater than λ_e. Since the best TE materials are predicted to be semiconductors with small band gaps, one challenge is to reduce λ_l without reducing *PF*. One possible approach is to introduce a wide range distribution of nano-, meso- and microstructures that can effectively scatter wide range of phonon spectra, which leads to a substantial reduction in λ_l without limiting *PF*, and hence enhancing *ZT*. Figure 2.6 shows a schematic diagram of possible mechanisms of phonon scattering in a TE material along with electronic transport of hot and cold electrons. Atomic defects (e.g. extrinsic dopants) can actively scatter short-wavelength phonons, but larger embedded defects, such as interfaces and grain boundaries, are needed to scatter mid- and long-wavelength phonons.

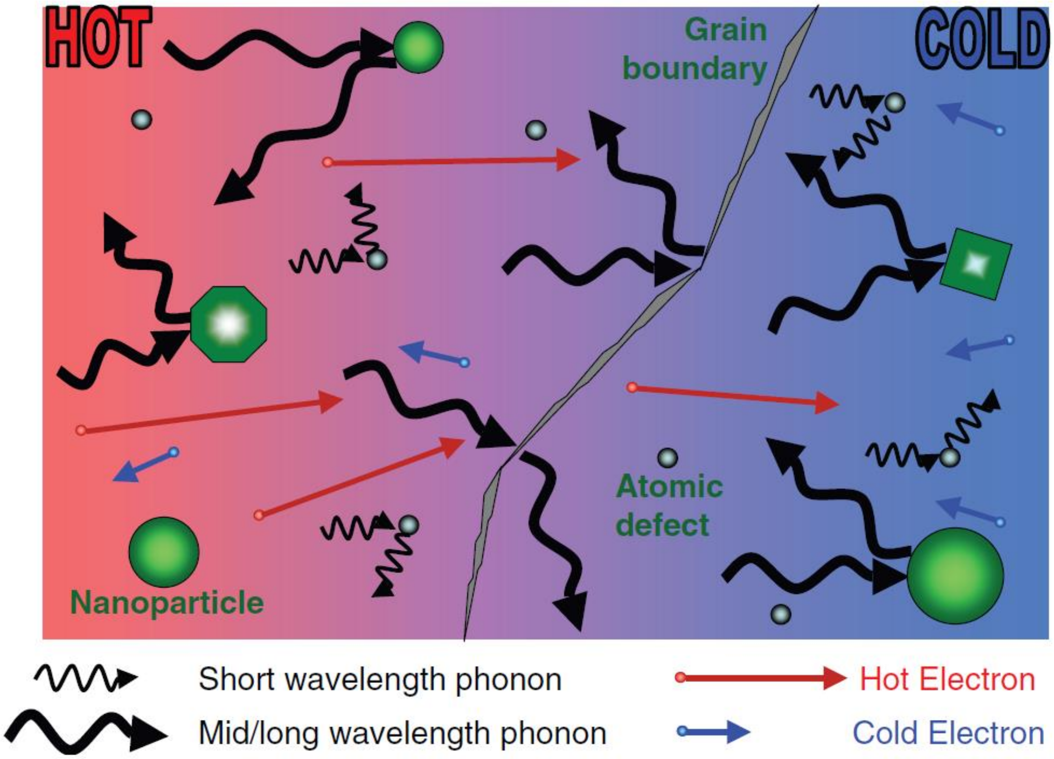

Figure 2.6. Schematic diagram illustrating various phonon scattering mechanisms within a TE material, along with electronic transport of hot and cold electrons. Atomic defects are effective at scattering short wavelength phonons, but larger embedded nanoparticles are required to scatter mid- and long-wavelength phonons effectively. Grain boundaries can also play an effective role in scattering these longer-wavelength phonons [10].

Figure 2.7 shows the contribution of different phonon modes to the accumulative λ_l of PbTe system. Around ~25% of λ_l value of PbTe is contributed by phonons with mean free paths of less than 5 nm, which can be mainly attributed to scattering by extrinsic dopants (atomic scale) or dislocations, and about 55% of λ_l is given by phonon modes with mean free paths between 5–100 nm, which can be scattered by nanoparticles embedded in PbTe lattice. The remaining ~20% of λ_l is contributed by phonon modes with mean free paths of 0.1–1 μm. Grains in meso- and microscale structures can scatter a considerable percentage of these additional phonons. Consequently, introducing structures with different length-scales (atomic, nano-, meso-, and microscale) in one material could substantially scatter a broad spectrum of phonons [17].

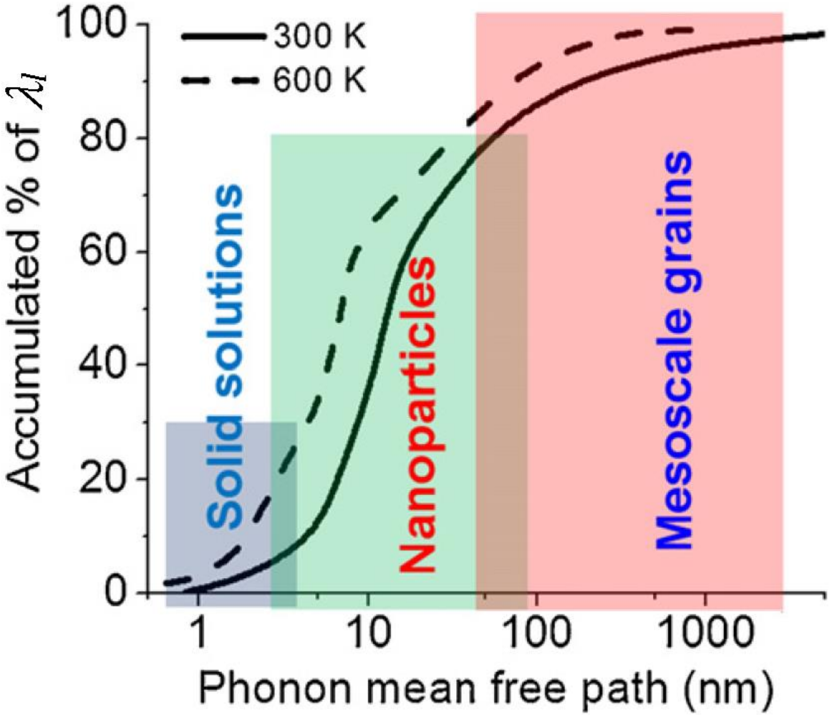

Figure 2.7. The accumulative lattice thermal conductivity as a function of phonon mean free path for PbTe at different temperatures. Atomic-scale dopants and nanoscale particles can effectively scatter short-wavelength phonons while mesoscale grains can scatter long-wavelength phonons [17].

In this work, wide size distribution of phonon scattering centers were introduced in the films and SLs in order to attack a wide range of phonon spectra, and hence reducing λ_l. For instance, various extrinsic dopants, having different ionic radii and atomic masses, were embedded at different lattice sites of STO films, and notable reduction in λ_l was observed as it will be discussed in Chapter 6. Another approach is to create clusters of oxygen vacancies in the films and SLs during the growth process. These clusters have size of few nanometers, which can effectively scatter midwavelength phonons [18]. Furthermore, fabricating superlattices with tunable number of interfaces could scatter long-wavelength phonons, especially in the in-plane direction [19].

2.2.3. Concentration of Charge Carriers

As the doping concentration increases, σ increases and the S decreases. Therefore there exists an optimum PF versus doping concentration at relatively high doping concentrations and Fermi levels close to, or inside the conduction band (degenerate limit). Ioffe addressed that good TE materials have a sweet spot of carrier concentration in the range of 10^{18}–10^{20} cm^{-3}, corresponding to degenerate semiconductors or semimetals [2].

Figure 2.8(a) shows ZT as a function of carrier concentration (n). Since σ and λ have a trade-off relationship with S, ZT maximizes at a certain value of n depending on the materials to be studied. The best ZT materials are found in doped semiconductors [3]. Insulators have poor σ while metals have relatively low S. In addition, λ of a metal, which is dominated by electrons, is proportional to σ, as dictated by the Wiedemann-Franz law. It is thus hard to attain high ZT in conventional metals. In semiconductors, λ is dominated by λ_l. Therefore, λ_l can be reduced without causing too much reduction of σ [20]. A reduced λ_l directly improves ZT, and additionally allows re-optimization of the carrier concentration for additional ZT improvement (Figure 2.8(b)).

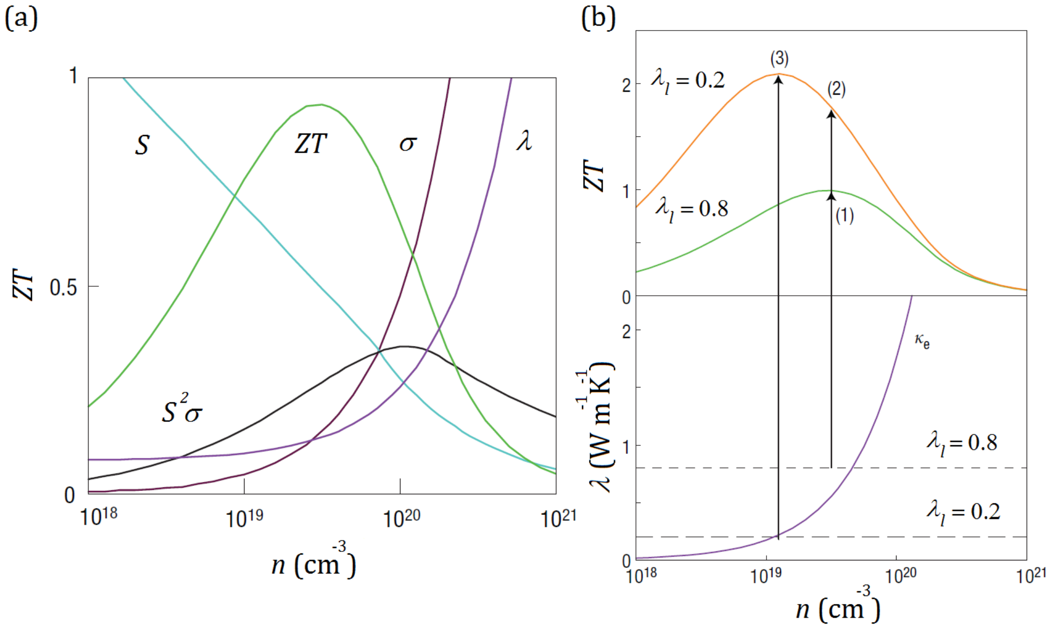

Figure 2.8. (a) Maximizing ZT needs a compromise of λ (plotted on the y axis from 0 to a top value of 10 W m^{-1} K^{-1}) and S (0 to 500 μV K^{-1}) with σ (0 to 5000 S cm^{-1}). Good TE materials are typically heavily doped semiconductors with n between 10^{19} and 10^{21} carriers per cm^3. Trends shown were modelled from Bi_2Te_3, based on empirical data in Reference [21]. (b) Reducing $\boldsymbol{\lambda_l}$ leads to a two-fold benefit for ZT. An optimized ZT of 0.8 is shown at point (1) for a model system (Bi_2Te_3) with a $\boldsymbol{\lambda_l}$ of 0.8 W m^{-1} K^{-1} and $\boldsymbol{\lambda_e}$ that is a function of n (purple). Reducing $\boldsymbol{\lambda_l}$ to 0.2 W m^{-1} K^{-1} directly increases the ZT to point (2). Additionally, lowering $\boldsymbol{\lambda}$ allows n to be re-optimized (reduced), leading to both a decrease in $\boldsymbol{\lambda_e}$ and a larger S. The re-optimized ZT is shown at point (3). This figure was reproduced from Reference [22].

2.3. Oxides and Literature Review

Traditional TE materials, such as Bi_2Te_3, PbTe, are composed of naturally rare, toxic, and heavy elements that can melt or be oxidized at high temperatures in air. Thus, these materials cannot be employed for extensive applications for waste heat recovery in air. To solve these problems, novel TE materials with high ZT composed of nontoxic, naturally abundant, light, and cheap elements should be developed. Metal oxides possess these requirements, and they are highly promising candidates from this point of view [23-25]. Nevertheless, metal oxides exhibit relatively low ZT

compared to traditional TE materials because of their relatively high λ. Reduction of λ without limiting PF is very crucial to improve ZT. Among metal oxides, crystalline STO and ZnO are attractive materials for waste heat recovery, particularly at high temperatures. In this work, different approaches were followed to improve the TE performance of doped STO- and ZnO-based thin films. In the following sections, brief backgrounds of STO and ZnO are presented. Recent progress made in TE research done for traditional TE materials, STO, and ZnO is also presented.

2.3.1. Strontium Titanate

The room-temperature crystal structure of STO is a cubic perovskite (ABO_3) with $Pm\bar{3}m$ space group, a lattice constant of a = 3.905 Å, and a theoretical density of 5.11 g cm^{-3}. Sr^{2+} ion occupies the corner position (A-site) of the perovskite structure and is surrounded by twelve O^{2-} ions located at the centers of the cubic faces as shown in Figure 2.9(a). Ti^{4+} ion occupies the center of the cube (B-site), surrounded by six O^{2-} ions, and hence forming a TiO_6 octahedral unit. STO is an indirect band-gap material as shown in Figure 2.9(b). The indirect and direct band gaps were experimentally determined as 3.25 and 3.75 eV, respectively [26]. The conduction bands in STO are mainly composed of Ti 3d orbitals consisting of triply degenerate orbitals ($3d_{xy}$, $3d_{yz}$, and $3d_{xz}$) while the upper valence band is composed of O 2p states, hybridized with Ti and Sr states [26].

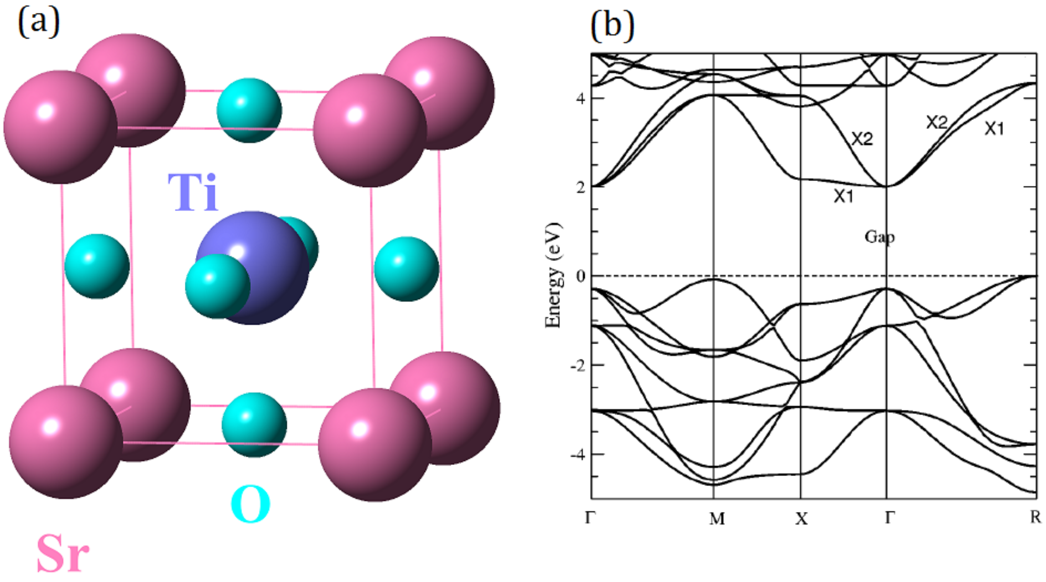

Figure 2.9. (a) A perovskite crystal structure of STO unit cell. (b) Electronic band structure of undoped STO [27].

The effective mass (m^*) of electrons in STO is relatively large [28], possibly due to the *d*-band nature, which should be responsible for the large S in STO. As a result of the possibly achievable, high σ and S, *PF* of a doped STO single crystal is high enough to compete with that of conventional TE materials like Bi_2Te_3 [29, 30]. Another attractive feature that makes STO a promising candidate for high-temperature TE applications is its high melting point of 2353 K. Furthermore, σ of STO can be easily tuned from insulating to metallic by substitutional doping of Sr^{2+} and Ti^{4+} cations with extrinsic dopants in A-site and B-site, respectively. Like other oxides, STO has high λ which is the main reason behind its low *ZT*, and hence more efforts should be investigated in this direction in order to enhance the TE performance of STO.

2.3.2. Zinc Oxide

ZnO possesses a wurtzite crystal structure with space group of $P6_3mc$ symmetry and a theoretical density of 5.606 g cm^{-3}. The lattice constants of ZnO crystal are 5.2098 Å and 3.2539 Å along c-axis and a-axis, respectively. In ZnO, both O^{2-} and Zn^{2+} ions form hexagonal-close-packed type sublattices (Figure 2.10(a)). The oxygen and zinc planes are stacked alternatively on each other along c-axis in lattice. Since ZnO lacks symmetry in its structure, it is a polar crystal with either O^{2-} or Zn^{2+} terminated surfaces [31].

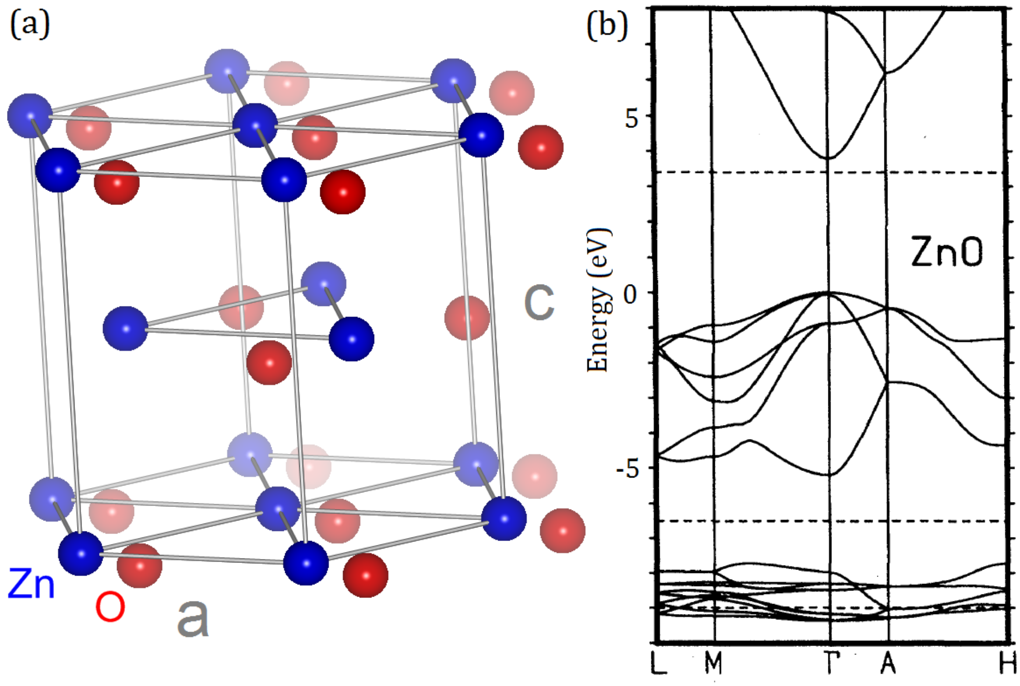

Figure 2.10. A wurtzite crystal structure of ZnO. (b) Electronic band structure of ZnO [32].

ZnO is a well-studied conductive oxide with a direct band gap of 3.3 eV (Figure 2.10(b)). Due to the small electronegativity between Zn^{2+} and O^{2-} ions, ZnO has a more covalent character compared to other metal oxides. According to this characteristic of ZnO, m^* of the free electrons is relatively low (0.38 m_0, where m_0 is the free electron mass), and comparable to those of Ge (0.55 m_0) and Bi_2Te_3 (0.58 m_0) [33]. Small m^* of electrons in ZnO systems could help in getting high values of mobility, and hence higher σ, but lower S, as it will be discussed later in Chapter 5.

2.3.3. Literature Review

2.3.3.1. Literature Review on Traditional TE materials

In the 1950s, alloys of Bi_2Te_3 were discovered to have $ZT \sim 1$ near room temperature [10], and they have played a vital role in the field of TEs. While each physical quantity that describes ZT (S, σ, and κ) can individually be tuned by several orders of magnitude, the strong coupling between these properties has made it extremely challenging to increase $ZT > 1$ despite five decades of active research (See Figure 2.11). The TE community is widely targeting $ZT \geq 3$ to make these solid-state systems competitive with traditional energy conversion systems. Recently, promising ZT values have been achieved for chalcogenide crystals, such as SrTe ($ZT \sim 2.2$) and SnSe ($ZT \sim 2.6$) [7, 34]. Despite these attractive results, for instance, SnSe does not seem to be utilized for real-life applications since it has displayed its high ZT only along one crystallographic direction at high temperature [35].

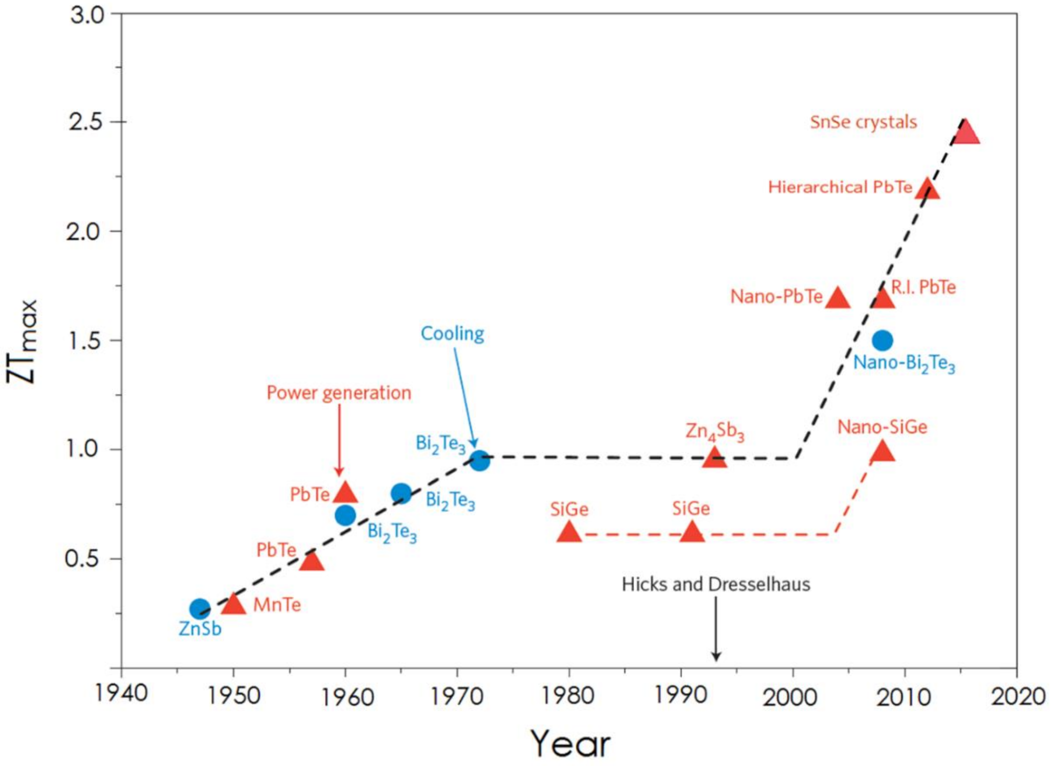

Figure 2.11. The improvement of the maximum *ZT* over time. Blue circles represent data for materials used in TE refrigeration, and red triangles represent data for materials used in TE power generation. The black dashed line is an eye-guide. This figure was reproduced from Reference [36].

2.3.3.2. Literature Review on TE Oxides

ZT of oxides is still lagging behind the current state-of-the-art TE materials [17, 22]. Nevertheless, oxides possess several distinguished characteristics from fundamental and application points of view as discussed previously. For instance, oxides can sustain at high temperature gradients due to its high chemical and thermal robustness (See Figure 2.12(a)), which is beneficial for a high Carnot efficiency [1]. In addition, oxides are known by their chemical versatility, and diversity of crystal structures, which allows a flexibility of compositional and structural tailoring. Finally, oxides are not costly in terms of raw materials and nontoxicity compared to heavy-metal-alloy TE materials, such as Te based materials as shown in Figure 2.12(b).

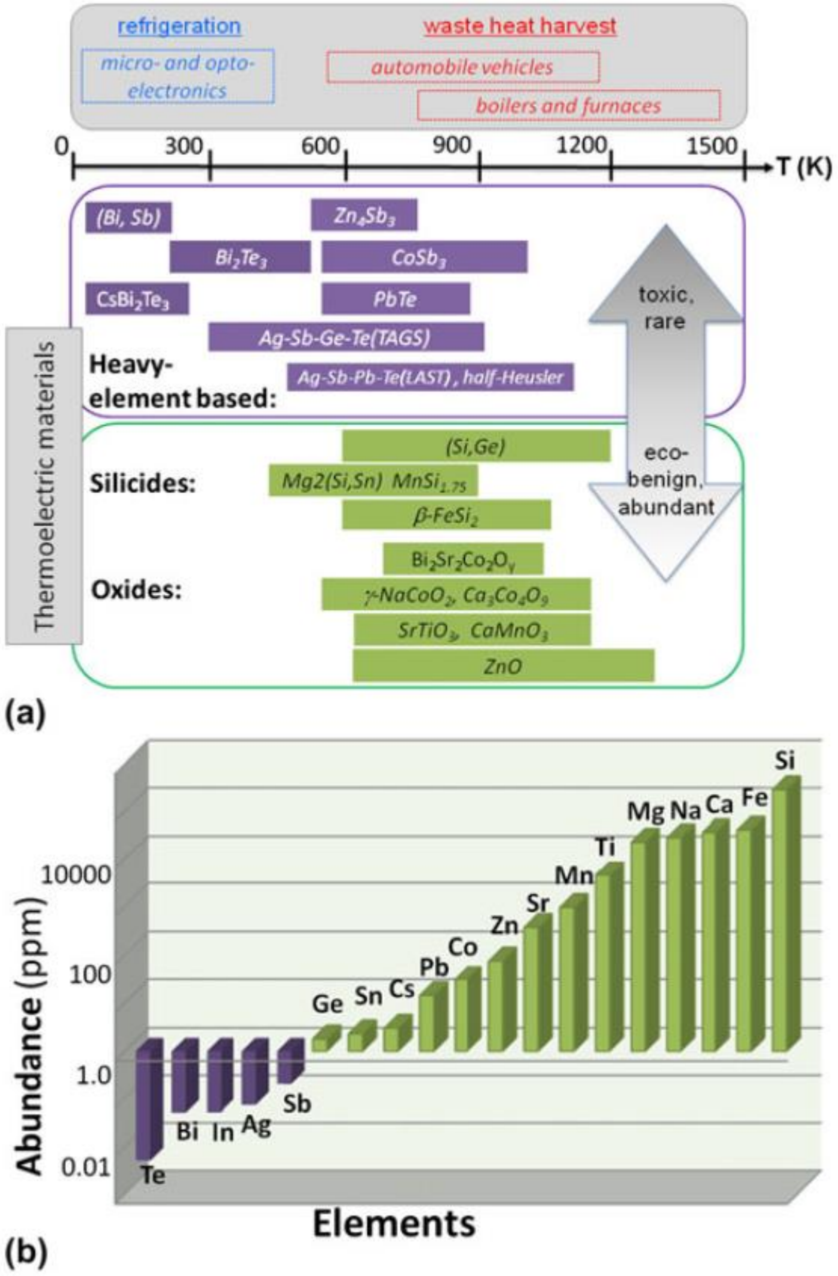

Figure 2.12. (a) Schematic representation for comparing various TE materials for applications of waste-heat recovery and refrigeration, in terms of the temperature of operation and the abundance and environmental friendliness of constituent elements. (b) The abundance of elements used in TE materials, the elements shown in purple-colored columns are less than 1 ppm (part per million). [24]

Figure 2.13 (a) and (b) summarize the ZT evolution of STO and ZnO based TE materials known up to date. As discussed earlier, the crucial challenge that encounters research in TE oxides is to reduce λ_l without limiting the decent PF. Different approaches were followed to reduce λ_l by using nano-structures, such as superlattices (SL*s*) [20, 37], nano-cubes [38], and nano-inclusions [39], while maintaining the high PF of the final structures. The maximum achieved ZT ($\sim$0.42) at 1190 K, for STO based materials, was reported by Kovalevsky *et al.* [40], by introducing rare-earth dopants to A-site. On the other hand, the best achieved ZT ($\sim$0.65) at 1247 K, for ZnO based materials, was reported by Ohtaki *et al*. [41], by dually doping bulk ZnO with Al^{3+} and Ga^{3+}.

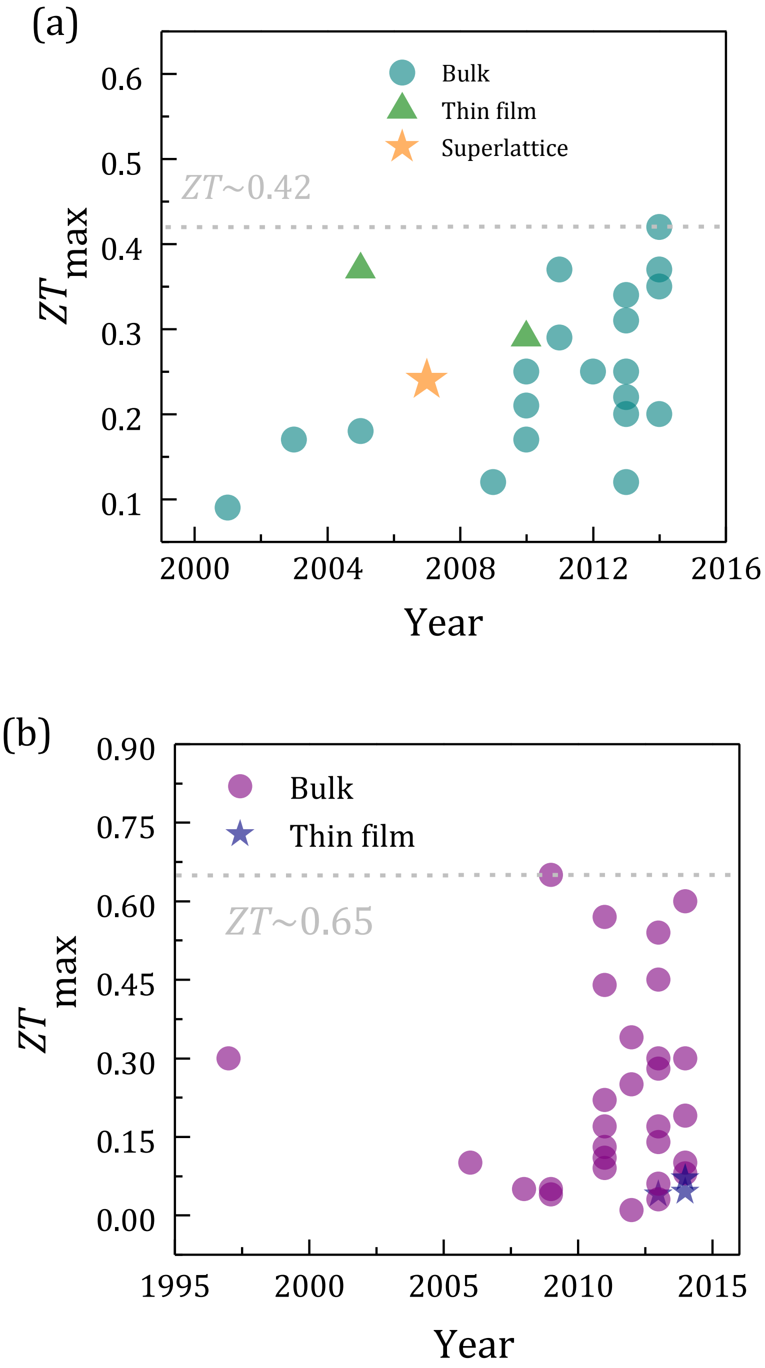

Figure 2.13. (a) Literature reviews of maximum *ZT* values obtained for STO [29, 30, 37, 40, 42-61] and (b) ZnO materials known up to date [41, 62-93].

2.4. References

1. T.M. Tritt,*"Thermoelectric Phenomena, Materials, and Applications",* Annual Review of Materials Research, 41, 433 (2011).
2. A. Ioffe, *"Semiconductor Thermoelements and Thermoelectric Cooling"*. Infosearch Limited (1957).
3. A. Shakouri,*"Recent Developments in Semiconductor Thermoelectric Physics and Materials",* Annual Review of Materials Research, 41, 399 (2011).
4. J.-F. Li, W.-S. Liu, L.-D. Zhao, and M. Zhou,*"High-performance nanostructured thermoelectric materials",* NPG Asia Mater, 2, 152 (2010).
5. H.J. Goldsmid, *"Theory of Thermoelectric Refrigeration and Generation"*, Springer Berlin Heidelberg, 7-21 (2010).
6. H. Goldsmid, *"Conversion Efficiency and Figure-of-Merit"*, CRC Press (1995).
7. L.-D. Zhao, S.-H. Lo, Y. Zhang, H. Sun, G. Tan, C. Uher, C. Wolverton, V.P. Dravid, and M.G. Kanatzidis,*"Ultralow thermal conductivity and high thermoelectric figure of merit in SnSe crystals",* Nature, 508, 373 (2014).
8. C.B. Vining,*"An inconvenient truth about thermoelectrics",* Nat Mater, 8, 83 (2009).
9. X.F. Zheng, C.X. Liu, Y.Y. Yan, and Q. Wang,*"A review of thermoelectrics research – Recent developments and potentials for sustainable and renewable energy applications",* Renewable and Sustainable Energy Reviews, 32, 486 (2014).
10. C.J. Vineis, A. Shakouri, A. Majumdar, and M.G. Kanatzidis,*"Nanostructured Thermoelectrics: Big Efficiency Gains from Small Features",* Advanced Materials, 22, 3970 (2010).
11. P. Pichanusakorn and P. Bandaru,*"Nanostructured thermoelectrics",* Materials Science and Engineering: R: Reports, 67, 19 (2010).
12. Y. Lan, A.J. Minnich, G. Chen, and Z. Ren,*"Enhancement of Thermoelectric Figure-of-Merit by a Bulk Nanostructuring Approach",* Advanced Functional Materials, 20, 357 (2010).
13. J.R. Sootsman, D.Y. Chung, and M.G. Kanatzidis,*"New and Old Concepts in Thermoelectric Materials",* Angewandte Chemie International Edition, 48, 8616 (2009).
14. A.J. Minnich, M.S. Dresselhaus, Z.F. Ren, and G. Chen,*"Bulk nanostructured thermoelectric materials: current research and future prospects",* Energy & Environmental Science, 2, 466 (2009).
15. J.M. Ziman, *"Principles of the Theory of Solids"*. Cambridge University Press (1972).
16. N.D.M. N. W. Ashcroft, *"Solid State Physics"*. (1976).
17. J. He, M.G. Kanatzidis, and V.P. Dravid,*"High performance bulk thermoelectrics via a panoscopic approach",* Materials Today, 16, 166 (2013).
18. C. Yu, M.L. Scullin, M. Huijben, R. Ramesh, and A. Majumdar,*"Thermal conductivity reduction in oxygen-deficient strontium titanates",* Applied

Physics Letters, 92, 191911 (2008).

19. G. Chen,*"Size and interface effects on thermal conductivity of superlattices and periodic Thin-film structures",* Journal of Heat Transfer, 119, 220 (1997).
20. R. Venkatasubramanian,*"Lattice thermal conductivity reduction and phonon localizationlike behavior in superlattice structures",* Physical Review B, 61, 3091 (2000).
21. D.M. Rowe and G. Min,*"α-in σ plot as a thermoelectric material performance indicator",* Journal of Materials Science Letters, 14, 617 (1995).
22. G.J. Snyder and E.S. Toberer,*"Complex thermoelectric materials",* Nat Mater, 7, 105 (2008).
23. J.W. Fergus,*"Oxide materials for high temperature thermoelectric energy conversion",* Journal of the European Ceramic Society, 32, 525 (2012).
24. J. He, Y. Liu, and R. Funahashi,*"Oxide thermoelectrics: The challenges, progress, and outlook",* Journal of Materials Research, 26, 1762 (2011).
25. K. Koumoto, Y. Wang, R. Zhang, A. Kosuga, and R. Funahashi,*"Oxide Thermoelectric Materials: A Nanostructuring Approach",* Annual Review of Materials Research, 40, 363 (2010).
26. K. van Benthem, C. Elsässer, and R.H. French,*"Bulk electronic structure of* $SrTiO_3$*: Experiment and theory",* Journal of Applied Physics, 90, 6156 (2001).
27. W. Luo, W. Duan, S.G. Louie, and M.L. Cohen,*"Structural and electronic properties of n-doped and p-doped* $SrTiO_3$*",* Physical Review B, 70, 214109 (2004).
28. H.P.R. Frederikse, W.R. Thurber, and W.R. Hosler,*"Electronic Transport in Strontium Titanate",* Physical Review, 134, A442 (1964).
29. S. Ohta, T. Nomura, H. Ohta, and K. Koumoto,*"High-temperature carrier transport and thermoelectric properties of heavily La- or Nb-doped* $SrTiO_3$ *single crystals",* Journal of Applied Physics, 97, 034106 (2005).
30. T. Okuda, K. Nakanishi, S. Miyasaka, and Y. Tokura,*"Large thermoelectric response of metallic perovskites:* $Sr_{1-x}La_xTiO_3$*",* Physical Review B, 63, 113104 (2001).
31. Ü. Özgür, Y.I. Alivov, C. Liu, A. Teke, M.A. Reshchikov, S. Doğan, V. Avrutin, S.-J. Cho, and H. Morkoç,*"A comprehensive review of ZnO materials and devices",* Journal of Applied Physics, 98, 041301 (2005).
32. D. Vogel, P. Krüger, and J. Pollmann,*"Ab initio electronic-structure calculations for II-VI semiconductors using self-interaction-corrected pseudopotentials",* Physical Review B, 52, R14316 (1995).
33. K. Koumoto, *"Thermoelectrics Handbook-Macro to Nano: Oxide Thermoelectrics"*, CRC Press, Chapter 35 (2005).
34. K. Biswas, J. He, I.D. Blum, C.-I. Wu, T.P. Hogan, D.N. Seidman, V.P. Dravid, and M.G. Kanatzidis,*"High-performance bulk thermoelectrics with all-scale hierarchical architectures",* Nature, 489, 414 (2012).
35. J.P. Heremans,*"Thermoelectricity: The ugly duckling",* Nature, 508, 327 (2014).
36. J.P. Heremans, M.S. Dresselhaus, L.E. Bell, and D.T. Morelli,*"When thermoelectrics reached the nanoscale",* Nat Nano, 8, 471 (2013).

37. H. Ohta, S. Kim, Y. Mune, T. Mizoguchi, K. Nomura, S. Ohta, T. Nomura, Y. Nakanishi, Y. Ikuhara, M. Hirano, H. Hosono, and K. Koumoto,*"Giant thermoelectric Seebeck coefficient of a two-dimensional electron gas in* $SrTiO_3$*",* Nat Mater, 6, 129 (2007).
38. Y. Kinemuchi, K.-i. Mimura, A. Towata, and K. Kato,*"Thermoelectric Properties of Rare Earth-Doped* $SrTiO_3$ *Nanocubes",* Journal of Electronic Materials, 42, 1 (2013).
39. H.C. N. Wang, H. He, W. Norimatsu, M. Kusunoki & K. Koumoto,*"Enhanced thermoelectric performance of Nb-doped* $SrTiO_3$ *by nano-inclusion with low thermal conductivity",* Scientific Reports, 3, 3449 (2013).
40. A.V. Kovalevsky, A.A. Yaremchenko, S. Populoh, P. Thiel, D.P. Fagg, A. Weidenkaff, and J.R. Frade,*"Towards a high thermoelectric performance in rare-earth substituted* $SrTiO_3$*: effects provided by strongly-reducing sintering conditions",* Physical Chemistry Chemical Physics, 16, 26946 (2014).
41. M. Ohtaki, K. Araki, and K. Yamamoto,*"High Thermoelectric Performance of Dually Doped ZnO Ceramics",* Journal of Electronic Materials, 38, 1234 (2009).
42. G.H. Zheng, Z.X. Dai, H.B. Li, H.Q. Wang, Y.Q. Li, X.F. Xu, B.T. Huang, Y.Q. Ma, and G. Li,*"Improving the Thermoelectric Properties of* $Sr_{0.9}La_{0.1}TiO_3$ *by Ag Addition",* Journal of Low Temperature Physics, 174, 128 (2014).
43. L. Li, Y. Liu, X. Qin, D. Li, J. Zhang, C. Song, and L. Wang,*"Enhanced thermoelectric performance of highly dense and fine-grained* $(Sr_{1-x}Gd_x)TiO_{3-\delta}$ *ceramics synthesized by sol–gel process and spark plasma sintering",* Journal of Alloys and Compounds, 588, 562 (2014).
44. G.H. Zheng, Z.H. Yuan, Z.X. Dai, H.Q. Wang, H.B. Li, Y.Q. Ma, and G. Li,*"Improvement of the Thermoelectric Properties of* $(Sr_{0.9}La_{0.1})_3Ti_2O_7$ *by Ag Addition",* Journal of Low Temperature Physics, 173, 80 (2013).
45. Y. Wang, C. Wan, X. Zhang, L. Shen, K. Koumoto, A. Gupta, and N. Bao,*"Influence of excess SrO on the thermoelectric properties of heavily doped* $SrTiO_3$ *ceramics",* Applied Physics Letters, 102, 183905 (2013).
46. T. Teranishi, Y. Ishikawa, H. Hayashi, A. Kishimoto, M. Katayama, and Y. Inada,*"Thermoelectric Efficiency of Reduced* $SrTiO_3$ *Ceramics Modified with La and Nb",* Journal of the American Ceramic Society, 96, 2852 (2013).
47. J. Liu, C.L. Wang, Y. Li, W.B. Su, Y.H. Zhu, J.C. Li, and L.M. Mei,*"Influence of rare earth doping on thermoelectric properties of* $SrTiO_3$ *ceramics",* Journal of Applied Physics, 114, 223714 (2013).
48. M.H. Lee, J.-S. Rhyee, M. Vaseem, Y.-B. Hahn, S.-D. Park, H. Jin Kim, S.-J. Kim, H.J. Lee, and C. Kim,*"Thermoelectric properties of* $SrTiO_3$ *nano-particles dispersed indium selenide bulk composites",* Applied Physics Letters, 102, 223901 (2013).
49. A.V. Kovalevsky, A.A. Yaremchenko, S. Populoh, A. Weidenkaff, and J.R. Frade,*"Enhancement of thermoelectric performance in strontium titanate by praseodymium substitution",* Journal of Applied Physics, 113, 053704 (2013).
50. F. Dang, C. Wan, N.-H. Park, K. Tsuruta, W.-S. Seo, and K. Koumoto,*"Thermoelectric Performance of* $SrTiO_3$ *Enhanced by Nanostructuring Self-Assembled Particulate Film of Nanocubes",* ACS Applied

Materials & Interfaces, 5, 10933 (2013).

51. J. Liu, C.L. Wang, H. Peng, W.B. Su, H.C. Wang, J.C. Li, J.L. Zhang, and L.M. Mei,*"Thermoelectric Properties of Dy-Doped* $SrTiO_3$ *Ceramics",* Journal of Electronic Materials, 41, 3073 (2012).
52. H.C. Wang, C.L. Wang, W.B. Su, J. Liu, Y. Sun, H. Peng, and L.M. Mei,*"Doping Effect of La and Dy on the Thermoelectric Properties of* $SrTiO_3$*",* Journal of the American Ceramic Society, 94, 838 (2011).
53. H.C. Wang, C.L. Wang, W.B. Su, J. Liu, H. Peng, Y. Sun, J.L. Zhang, M.L. Zhao, J.C. Li, N. Yin, and L.M. Mei,*"Synthesis and thermoelectric performance of Ta doped* $Sr_{0.9}La_{0.1}TiO_3$ *ceramics",* Ceramics International, 37, 2609 (2011).
54. Y. Wang, K. Lee, H. Hyuga, H. Kita, H. Ohta, and K. Koumoto,*"Enhancement of thermoelectric performance in rare earth-doped* $Sr_3Ti_2O_7$ *by symmetry restoration of* TiO_6 *octahedra",* Journal of Electroceramics, 24, 76 (2010).
55. N. Wang, H. Li, Y. Ba, Y. Wang, C. Wan, K. Fujinami, and K. Koumoto,*"Effects of YSZ Additions on Thermoelectric Properties of Nb-Doped Strontium Titanate",* Journal of Electronic Materials, 39, 1777 (2010).
56. N. Wang, L. Han, H. He, Y. Ba, and K. Koumoto,*"Effects of mesoporous silica addition on thermoelectric properties of Nb-doped SrTiO3",* Journal of Alloys and Compounds, 497, 308 (2010).
57. J. Ravichandran, W. Siemons, D.W. Oh, J.T. Kardel, A. Chari, H. Heijmerikx, M.L. Scullin, A. Majumdar, R. Ramesh, and D.G. Cahill,*"High-temperature thermoelectric response of double-doped* $SrTiO_3$ *epitaxial films",* Physical Review B, 82, 165126 (2010).
58. Y. Wang, K.H. Lee, H. Ohta, and K. Koumoto,*"Thermoelectric properties of electron doped* $SrO(SrTiO_3)_n(n=1,2)$ *ceramics",* Journal of Applied Physics, 105, 103701 (2009).
59. S. Ohta, T. Nomura, H. Ohta, M. Hirano, H. Hosono, and K. Koumoto,*"Large thermoelectric performance of heavily Nb-doped* $SrTiO_3$ *epitaxial film at high temperature",* Applied Physics Letters, 87, 092108 (2005).
60. H. Muta, K. Kurosaki, and S. Yamanaka,*"Thermoelectric properties of rare earth doped* $SrTiO_3$*",* Journal of Alloys and Compounds, 350, 292 (2003).
61. A.M. Dehkordi, S. Bhattacharya, J. He, H.N. Alshareef, and T.M. Tritt,*"Significant enhancement in thermoelectric properties of polycrystalline Pr-doped* $SrTiO_{3-\delta}$ *ceramics originating from nonuniform distribution of Pr dopants",* Applied Physics Letters, 104, 193902 (2014).
62. S. Saini, P. Mele, H. Honda, K. Matsumoto, K. Miyazaki, L.M. Luna, and P.E. Hopkins,*"Influence of Postdeposition Cooling Atmosphere on Thermoelectric Properties of 2% Al-Doped ZnO Thin Films Grown by Pulsed Laser Deposition",* Journal of Electronic Materials, 1 (2014).
63. H. Cheng, X.J. Xu, H.H. Hng, and J. Ma,*"Characterization of Al-doped ZnO thermoelectric materials prepared by RF plasma powder processing and hot press sintering",* Ceramics International, 35, 3067 (2009).
64. L. Zhang, T. Tosho, N. Okinaka, and T. Akiyama,*"Thermoelectric Properties of Solution Combustion Synthesized Al-Doped ZnO",* Materials Transactions, 49, 2868 (2008).

65. Y.K. Hisashi Kaga, Satoshi Tanaka, Atsushi Makiya, Zenji Kato, Keizo Uematsu and Koji Watari,*"Preparation and Thermoelectric Property of Highly Oriented Al-Doped ZnO Ceramics by a High Magnetic Field",* Japanese Journal of Applied Physics, 45, L1212 (2006).
66. Y. Kinemuchi, M. Mikami, K. Kobayashi, K. Watari, and Y. Hotta,*"Thermoelectric Properties of Nanograined ZnO",* Journal of Electronic Materials, 39, 2059 (2010).
67. T. Tsubota, M. Ohtaki, K. Eguchi, and H. Arai,*"Thermoelectric properties of Al-doped ZnO as a promising oxide material for high-temperature thermoelectric conversion",* Journal of Materials Chemistry, 7, 85 (1997).
68. H. Yamaguchi, Y. Chonan, M. Oda, T. Komiyama, T. Aoyama, and S. Sugiyama,*"Thermoelectric Properties of ZnO Ceramics Co-Doped with Al and Transition Metals",* Journal of Electronic Materials, 40, 723 (2011).
69. X. Qu, W. Wang, S. Lv, and D. Jia,*"Thermoelectric properties and electronic structure of Al-doped ZnO",* Solid State Communications, 151, 332 (2011).
70. M. Ohtaki and K. Araki,*"Thermoelectric properties and thermopower enhancement of Al-doped ZnO with nanosized pore structure",* Journal of the Ceramic Society of Japan, 119, 813 (2011).
71. Y. Liu, Z. Zhang, X. Wei, Q. Li, and L.-M. Peng,*"Simultaneous Electrical and Thermoelectric Parameter Retrieval via Two Terminal Current–Voltage Measurements on Individual ZnO Nanowires",* Advanced Functional Materials, 21, 3900 (2011).
72. P. Jood, R.J. Mehta, Y. Zhang, G. Peleckis, X. Wang, R.W. Siegel, T. Borca-Tasciuc, S.X. Dou, and G. Ramanath,*"Al-Doped Zinc Oxide Nanocomposites with Enhanced Thermoelectric Properties",* Nano Letters, 11, 4337 (2011).
73. K.-H. Jung, K. Hyoung Lee, W.-S. Seo, and S.-M. Choi,*"An enhancement of a thermoelectric power factor in a Ga-doped ZnO system: A chemical compression by enlarged Ga solubility",* Applied Physics Letters, 100, 253902 (2012).
74. N. Vogel-Schäuble, R. Dujardin, A. Weidenkaff, and M. Aguirre,*"Influence of Thermal Aging Phenomena on Thermoelectric Properties of Al-Substituted ZnO",* Journal of Electronic Materials, 41, 1606 (2012).
75. T. Teranishi, Y. Mori, H. Hayashi, and A. Kishimoto,*"Thermoelectric Property of Polycrystalline Aluminum-Doped Zinc Oxide Enhanced by Micropore Foaming",* Journal of the American Ceramic Society, 95, 690 (2012).
76. H. Colder, E. Guilmeau, C. Harnois, S. Marinel, R. Retoux, and E. Savary,*"Preparation of Ni-doped ZnO ceramics for thermoelectric applications",* Journal of the European Ceramic Society, 31, 2957 (2011).
77. L. Han, N.V. Nong, L.T. Hung, T. Holgate, N. Pryds, M. Ohtaki, and S. Linderoth,*"The influence of α- and γ-Al_2O_3 phases on the thermoelectric properties of Al-doped ZnO",* Journal of Alloys and Compounds, 555, 291 (2013).
78. L. Han, L. Hung, N. van Nong, N. Pryds, and S. Linderoth,*"The Influence of Spark Plasma Sintering Temperature on the Microstructure and Thermoelectric Properties of Al,Ga Dual-Doped ZnO",* Journal of Electronic

Materials, 42, 1573 (2013).

79. S.-M. Choi, K. Lee, K.-H. Jung, Y. Lim, and W.-S. Seo,*"Effects of Process Variable Control on the Thermoelectric Properties of the Zn0.98Ga(Al)0.02O System",* Journal of Electronic Materials, 42, 2056 (2013).
80. J.F. Tomoyuki ENDO, Yamato HAYASHI and Hirotsugu TAKIZAWA,*"Fabrication of* $(Zn_{1-x}Al_xO)_5In_2O_3$ *by microwave irradiation and thermoelectric characterization",* Journal of the Ceramic Society of Japan, 121, 416 (2013).
81. M. Søndergaard, E.D. Bøjesen, K.A. Borup, S. Christensen, M. Christensen, and B.B. Iversen,*"Sintering and annealing effects on ZnO microstructure and thermoelectric properties",* Acta Materialia, 61, 3314 (2013).
82. N.N. Wang, H.X. Xin, D. Li, X.J. Li, J. Zhang, and X.Y. Qin,*"High temperature thermoelectric properties of Nb-doped ZnO ceramics",* Journal of Physics and Chemistry of Solids, 74, 1811 (2013).
83. M. Ruoho, V. Pale, M. Erdmanis, and I. Tittonen,*"Influence of aluminium doping on thermoelectric performance of atomic layer deposited ZnO thin films",* Applied Physics Letters, 103, 203903 (2013).
84. P. Fan, Y.-z. Li, Z.-h. Zheng, Q.-y. Lin, J.-t. Luo, G.-x. Liang, M.-q. Zhang, and M.-c. Chen,*"Thermoelectric properties optimization of Al-doped ZnO thin films prepared by reactive sputtering Zn–Al alloy target",* Applied Surface Science, 284, 145 (2013).
85. Z.-H. Wu, H.-Q. Xie, and Y.-B. Zhai,*"Enhanced thermoelectric figure of merit in nanostructured ZnO by nanojunction effect",* Applied Physics Letters, 103, 243901 (2013).
86. H. Takemoto, K. Fugane, P. Yan, J. Drennan, M. Saito, T. Mori, and H. Yamamura,*"Reduction of thermal conductivity in dually doped ZnO by design of three-dimensional stacking faults",* RSC Advances, 4, 2661 (2014).
87. P. Jood, R.J. Mehta, Y. Zhang, T. Borca-Tasciuc, S.X. Dou, D.J. Singh, and G. Ramanath,*"Heavy element doping for enhancing thermoelectric properties of nanostructured zinc oxide",* RSC Advances, 4, 6363 (2014).
88. L. Han, N. Van Nong, W. Zhang, L.T. Hung, T. Holgate, K. Tashiro, M. Ohtaki, N. Pryds, and S. Linderoth,*"Effects of morphology on the thermoelectric properties of Al-doped ZnO",* RSC Advances, 4, 12353 (2014).
89. J. Loureiro, N. Neves, R. Barros, T. Mateus, R. Santos, S. Filonovich, S. Reparaz, C.M. Sotomayor-Torres, F. Wyczisk, L. Divay, R. Martins, and I. Ferreira,*"Transparent aluminium zinc oxide thin films with enhanced thermoelectric properties",* Journal of Materials Chemistry A, 2, 6649 (2014).
90. Y. Zhao, B. Chen, A. Miner, and S. Priya,*"Low thermal conductivity of Al-doped ZnO with layered and correlated grains",* RSC Advances, 4, 18370 (2014).
91. N. Vogel-Schäuble, T. Jaeger, Y.E. Romanyuk, S. Populoh, C. Mix, G. Jakob, and A. Weidenkaff,*"Thermal conductivity of thermoelectric Al-substituted ZnO thin films",* physica status solidi (RRL) – Rapid Research Letters, 7, 364 (2013).
92. L. Brockway, V. Vasiraju, M.K. Sunkara, and S. Vaddiraju,*"Engineering Efficient Thermoelectrics from Large-Scale Assemblies of Doped ZnO Nanowires: Nanoscale Effects and Resonant-Level Scattering",* ACS Applied Materials &

Interfaces, 6, 14923 (2014).

93. W.H. Nam, Y.S. Lim, S.-M. Choi, W.-S. Seo, and J.Y. Lee,*"High-temperature charge transport and thermoelectric properties of a degenerately Al-doped ZnO nanocomposite",* Journal of Materials Chemistry, 22, 14633 (2012).

Chapter 3.

Experimental Procedures

This chapter is dedicated to review all experimental procedures used in this work. Most of the experimental tasks were performed at Prof. Husam N. Alshareef's *Functional Nanomaterials and Devices Laboratory*, including the growth of thin films and superlattices by pulsed laser deposition (PLD), TE transport measurements, and thermal conductivity measurement. The specimens were characterized using the facilities at *KAUST core labs*. The chapter is divided into three main sections: Growth of Thin Films and Superlattices, Transport Measurements, and Materials Characterization.

3.1 Growth of Thin Films and Superlattices

3.1.1. Pulsed Laser Deposition

Pulsed laser deposition (PLD) is one type of physical vapor deposition (PVD) methods. Due to its capability in growing stoichiometric, uniform, and multilayered films, PLD was selected to grow the thin films and SLs in this work. The first ever PLD experiment was carried out by smith and Turner in 1965, shortly after the invention of the pulsed ruby laser, in order to grow thin films of semiconductors and dielectrics [1]. However, twenty years later, PLD received more attention and came into widespread use in the applications of thin film technology. The stimulant finding was the discovery of high-quality superconducting films grown by low oxygen pressure

PLD without the necessity of further processing steps [2].

The main components of the PLD system are shown in the schematic representation in Figure 3.1. An ultraviolet (UV) laser pulses, with a specific energy density, are focused by external lenses onto a rotating target. The external lenses should satisfy the condition of optical transparency to ultraviolet light before reaching the ceramic targets inside the main chamber. Two main events can take place when one laser pulse reaches the target surface. First event is the rapid heating and vaporization of the target surface by a portion of the laser pulse, and second, the absorption of the remainder of the laser pulse to heat and accelerate the plasma, which contains neutral atoms, molecules, ions, and clusters. These ablated components undergo collisions in the high density region near the target to create highly directional plume perpendicular to the target surface with high velocities around 10^6 cm s^{-1}. The ablated constituents propagate with gradually decreasing velocity toward the substrate, which is typically 5–10 cm away from the target, on which the growth occurs. The crystalline quality (amorphous, polycrystalline, or epitaxial single-crystal) of the grown film depends mainly on the substrate material and its temperature [3]. The uniqueness of PLD is that the energy source is outside the chamber, which facilitates a large range of operating pressures (10^{-10}–100 Torr) during film growth. By controlling the pressure and temperature, a variety of nanostructures and nanoparticles can be synthesized with unique functionalities.

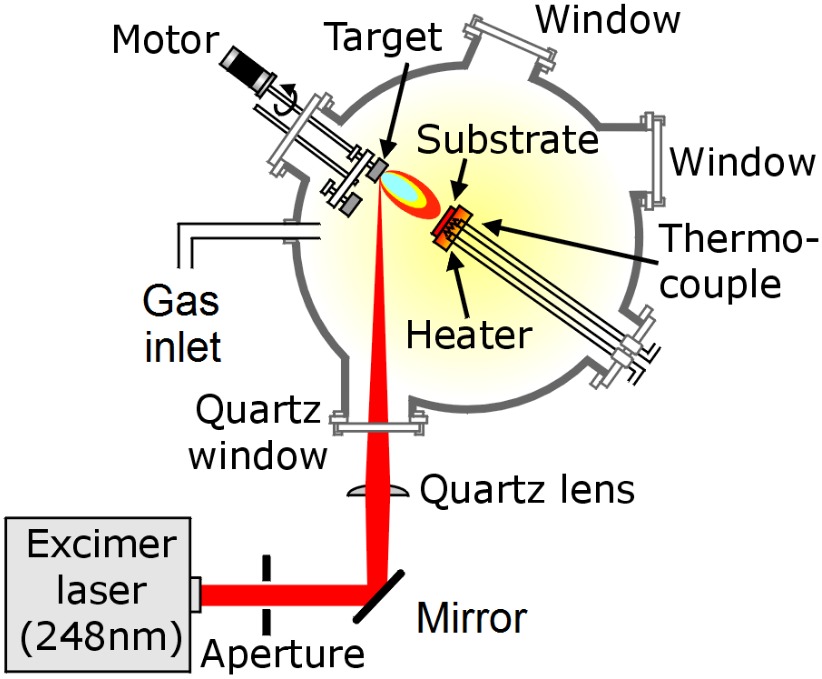

Figure 3.1. Schematic representation of PLD [4].

At the *Functional Nanomaterials and Device Laboratory*, PLD is performed in a Pioneer-240 model system from Neocera (Beltsville, MD) [5]. The system has a spherical (24” diameter), stainless steel chamber equipped with a load lock chamber. High vacuum ($<10^{-8}$ Torr) can be achieved inside the chamber using a turbo pump, with a maximum six targets (1” diameter) can be installed inside which enable us to grow SLs of different materials at the same time. Three independent mass flow controllers (MFC) allow gas flowing of Ar, N_2, or O_2 to the chamber with specific flow values measured in units of standard cubic centimeters per second (sccm). The target to substrate-holder (4″ diameter) distance is ~8 cm. In each deposition, the substrate rotates at speed of 29 revolutions per minute (rpm) to ensure a uniform growth for 1″×1″ substrates. The substrate holder can be placed directly in front of a radiant heater which can heat up to 1300 K. A KrF excimer laser (λ=248 nm, pulse duration ~20 ns, repetition rate =1–20 Hz) is installed outside the chamber to emit laser pulses directed and focused into the main chamber using a setup of optical lenses and mirrors. A clean laser window can be used before every deposition to eliminate run-to-run variation in laser fluence at the target due to coating on the laser window. The laser fluence is monitored regularly by a power meter to ensure a stable and reliable pre-set laser fluence at the source.

3.1.2. Magnetron Sputtering

Sputtering is a physical vapor deposition (PVD) technique which depends on bombarding ions in order to eject atoms from a solid material. Atoms or molecules are physically removed from the target to be deposited in a substrate after being transported through a vacuum or an ambient gas. The atoms are ejected from the target surface as a result of collisions and momentum transfer from the impinging highly energetic ions, created during the ionization of a gaseous species, to target materials. The sputtered constituents are directed to the substrate by an electric field to grow a thin film [6].

The process starts with two electrodes installed in a vacuum chamber. The electrodes are the target (cathode) and the substrate (anode). An inert gas (usually Argon) flows to the chamber and an electric field applied to the electrodes. Under the applied electric field, electrons are accelerated towards the anode (+) colliding with the atoms of the gas and making them ionized. Ions can be accelerated towards the cathode leading to the ejection of atoms from the source material (target). Secondary electrons are emitted from the surface, allowing the glow discharge to be sustained, as a result of the ions striking the cathode. When a direct current (dc) is used in the ionization process, the process is called a dc magnetron sputtering. It is the simplest method, as a dc voltage is applied between the cathode and the anode, nevertheless it is restricted to conductive targets, as insulating targets are not able to supply enough secondary electrons to sustain the glow discharge. To overcome this issue, radio frequency (rf) magnetron sputtering can be employed. In this process a high frequency voltage is supplied to the target to attract electrons from the glow discharge during the positive pulse of the rf signal. Both conductive and insulating materials can be deposited by rf magnetron sputtering [6].

The rf magnetron sputtering tool (ESCRD4, Equipment Company Ltd., Cambridge, England) at *KAUST core labs* was used to deposit SiN_x insulating film. To prepare samples for the thermal conductivity measurement, SiN_x layers were employed to separate the metal microheaters and the conductive oxide films, and also they used as buffer layers between the Si substrate and conductive oxide films, as it will be discussed later. SiN_x films (100 nm) were deposited at room temperature by applying 100 W rf electrical power with frequency of 13.56 MHz. Argon was used in the deposition under pressure of 10 mTorr. The distance between the target and the substrate was maintained at 180 mm, while rotating the substrate to ensure a uniform deposition. The target was pre-sputtering for 60 seconds to clean the target surface prior the real deposition.

3.2 Transport Measurements

Reliable and accurate measurements of transport properties are critically important in order to improve research in TEs. This section is dedicated to review all transport measurement techniques used in this work. The typical physical parameters are needed, to fully characterize any TE materials are electrical conductivity (σ), Seebeck coefficient (S), thermal conductivity (λ), and carrier concentration (n). All of these physical quantities were measured at the *Functional Nanomaterials and Devices Laboratory* except Hall measurement which was performed at *KAUST core labs*.

3.2.1. Electrical Conductivity

The σ measurement of many materials can be achieved straightforward. The simplest way to measure σ is to send a constant current through two electrical probes and measure the voltage across them. By using this two-probe method, we cannot isolate the sample resistance from other resistances in the circuits, such as contact resistance and the intrinsic resistance of the probes. To overcome these issues, four-probe method can be used to determine σ [7]. In this method, a separate pair of probes is used to measure the voltage with a high impedance, so that the parasitic resistances are negligible since small current flows along the voltage probe pairs. For bulk samples, metal foils can be used at the two sides of the sample to ensure uniform current flow along the sample and the two voltage probes can be placed on the sample surface with a known distance between them along the current direction. For thin films, however, all four probes are placed on the surface of the film. Figure 3.2(a) illustrates the linear four-probe configuration for thin film measurements used in this work.

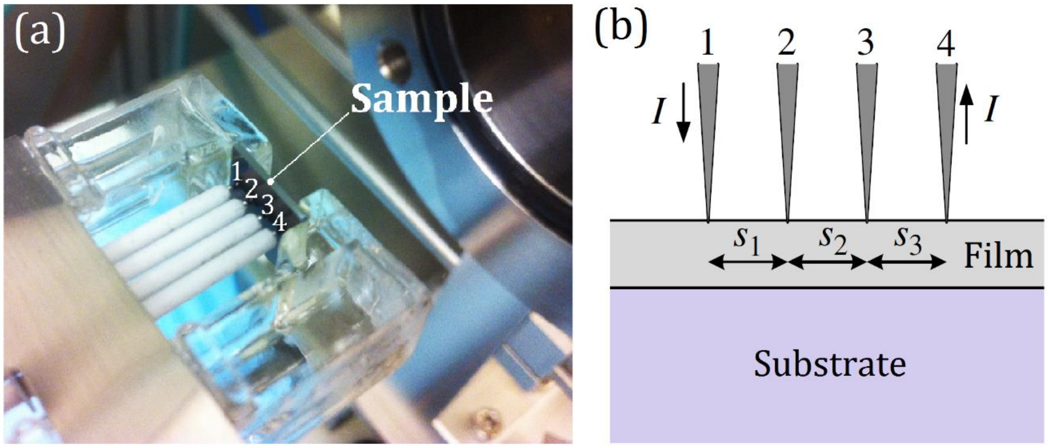

Figure 3.2. (a) Linear four-probe measurement system for in-plane $\boldsymbol{\sigma}$ and S of thin films (RZ2001i, Ozawa Science, Nagoya, Japan). (b) Cross sectional schematic diagram of the linear four probes along with film on substrate.

Ohm's law describes σ by the following equation:

$$\sigma = \frac{l}{wd}\frac{V}{I}, \tag{3.1}$$

where V, I, l, w, and d, are voltage measured between probes 2 and 3 (Figure 3.2(b)), electrical current flowing in the length direction of the film (from probe 1 to 4), length, width, and thickness of the film, respectively. In this work, we used a commercial system to measure σ of the films and SLs (RZ2001i, Ozawa Science, Nagoya, Japan). Using this system, σ can be measured from 300–1273 K under an ambient gas. All measurements done in this work were performed under Ar/H_2 (96%

Ar and 4% H_2) ambient as it induces the creation of oxygen vacancies in oxide films. At any temperature, σ (s cm^{-1}) is extracted using Equation 3.1 after measuring the slope ($\Delta V/\Delta I$) of the I-V curve which is customized to have five values of I (from -0.5 to 0.5 mA) with their corresponding voltage values. The measurement of σ is then repeated at a higher sample temperature, thereby enabling studies on change in σ during heating. It is important to note that, in order to measure the intrinsic σ of thin films or SLs, insulating substrates should be used to eliminate any parasitic contribution to the measured σ.

3.2.2. Seebeck Coefficient

S is an intrinsic property of a material, which is strongly dependent on the electronic band structure. Measurement of S-T dependence, with the help of other measurements, provides us with information on electronic transport properties, such as type of charge carriers, scattering parameter, and effective mass. S can be measured, on the same sample used in σ measurement, allowing us to fairly correlate both measurements. There are two main methods to measure S: the integral and the differential (Figure 3.3(a) and (b), respectively). In integral method (large ΔT), one end of the specimen is maintained at a fixed temperature T_1 while the other end is varied through T_2=T_1+ΔT. S can be extracted at any temperature, with respect to thermocouple used in the measurement, by using the equation: $S(T) = (dV/dT)_T$ as shown in Figure 3.3(a) [8]. Integral method overcomes the problem of having voltage offsets due to the large thermal gradients, and hence larger voltage signals. However, it is difficult to maintain the large thermal gradients at high temperatures, especially for small samples [9].

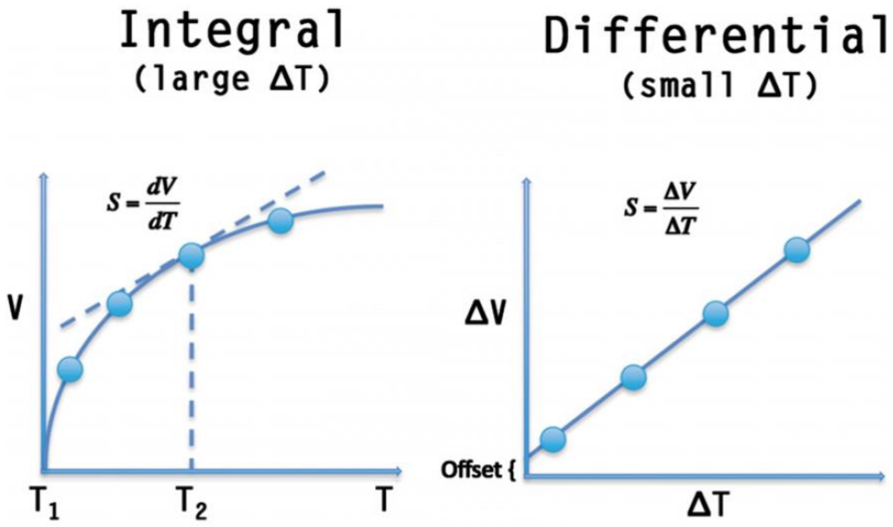

Figure 3.3. Illustrations of integral and differential methods of S measurement [9].

On the other hand, the differential method (small ΔT), which is used in the majority of high temperature characterizations of S, can overcome most difficulties encountered by the integral method. For example, the small thermal gradients required to perform the measurements are easily achievable even at high temperatures unlike the integral method where maintaining the high thermal gradients are quite challenging, especially at high temperature regimes. In the differential method, a small thermal gradient ΔT applied across the specimen is maintained at an average temperature of interest $T_{av} = (T_1 + T_2)/2$, where $T_1 = T_{av} - \Delta T/2$ and $T_2 = T_{av} + \Delta T/2$. Afterwards, S can be extracted from the slope of a linear fit composed of multiple voltage/temperature difference data points rather than one (Figure 3.3(b)).

At the *Functional Nanomaterials and Devices Laboratory*, S was measured in the range of 300–1000 K by using the differential method under Ar/H_2 (96% Ar and 4% H_2) ambient using the commercial setup same as used in σ measurement (RZ2001i, Ozawa Science, Nagoya, Japan). Pt–Pt/Rh thermocouples were used as probes which simultaneously served the purpose of voltage and current probes as well as temperature sensors. To have small temperature gradients (ΔT), one edge of the specimen is cooled by flowing air through quartz tube installed inside one of the sample holders (see arrow in Figure 3.4(a)). The automated setup allows simultaneous measurement of σ and S at any given temperature, enabling studies on the evolution of the physical properties during annealing of the sample in the selected ambient. Some measurements (see Figure 3.4(b)) were performed right after the system installation in order to calibrate S measurements using a high purity Ni sheet in the temperature range 300-850 K in flowing Ar. The measured curves match well with those reported for Ni [10, 11].

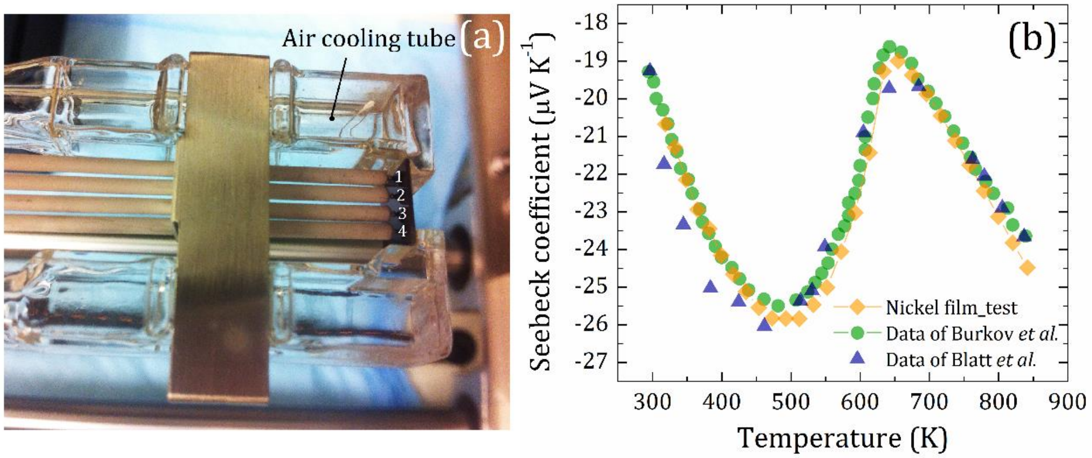

Figure 3.4. (a) TE measurement system used to measure S by differential method. Air flow is applied through a quartz tube on one specimen edge to make small temperature gradients (ΔT). (b) Seebeck coefficient calibration runs carried out using a high purity Ni sheet in the temperature range 300-850 K in flowing Ar. Measured data matches well with those reported for Ni [10, 11].

3.2.3. Thermal Conductivity

We used the differential 3ω method [12, 13] to measure the cross-plane thermal conductivity of the films. In this method, an alternating current passes through metal lines (Au microheaters), patterned on a reference sample and one with additional film (Figure 3.5(a) and (b), respectively). The Au microheater act as both a heater and a thermometer. The alternating current with angular frequency ω creates Joule heating at 2ω ($I^2(\omega)R$, where I is the current and R is the resistance). This heating causes the temperature of the Au microheater to oscillate at 2ω, and hence its resistance oscillates at 2ω. Therefore, a small voltage component ($I(\omega) \times R(2\omega)$) is produced at 3ω [13]. The temperature rise of the Au microheater can be expressed by [12]:

$$\Delta T = 2R\left(\frac{dR}{dT}\right)^{-1}\frac{V_{3\omega}}{V_{1\omega}}, \qquad (3.2)$$

where R is the resistance of the Au microheater, dR/dT is the temperature dependent coefficient of resistance of the Au microheater, $V_{1\omega}$ and $V_{3\omega}$ are the amplitudes of the first and third harmonic voltage drops along the Au microheater, respectively.

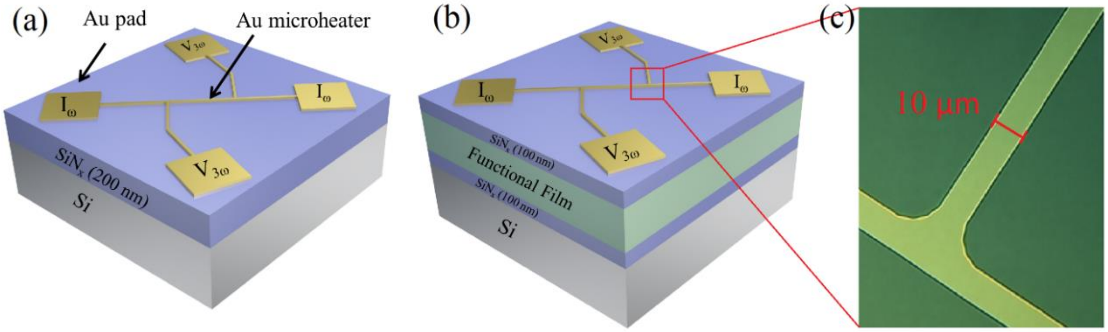

Figure 3.5. Schematic representations for the (a) reference sample and a (b) sample with additional film (doped STO), used in the differential 3ω method, and (c) optical micrograph of 10 μm wide Au microheater.

In order to pattern Au microheater on the electrically conductive film, an insulating layer is needed to prevent any leakage current. Therefore, SiN_x film was deposited on doped STO films (Figure 3.5(b)) and bare Si substrate (Figure 3.5(a)) using sputtering, and we measured the temperature rise from both samples. An algorithm was used to extract the temperature drops across the functional film from the rise in temperature across the two samples, using the differential 3ω method. Since the differential 3ω method allows the measurement of the thermal conductivity of the additional film, it removes uncertainties in the thermal properties of other layers [12].

Since the width of the Au microheater is 10 μm (Figure 3.5(c)) which is much larger than the thickness (~500 nm) of the film, the heat flow can be described as one dimensional, and the additional film has a frequency-independent temperature rise given by [14]:

$$\Delta T_f = \frac{P_l \, t_f}{w \, \lambda_f}, \tag{3.3}$$

where P_l, λ_f, t_f, and w are the heating power unit length, the thermal conductivity of the additional film, the thickness of the film, and the width of the microheater, respectively. For the anisotropic thermal properties of the films, the combination between w and t_f determines the measurement sensitivity to the in-plane and cross-plane heat flows in the film [12]. If $w \gg t_f$, the measured ΔT is mainly assumed to be sensitive to the cross-plane λ_f. On the other hand, if $w \sim t_f$, the heat generated by Au microheater spreads in the film, and the measured ΔT is influenced by both cross-plane and in-plane λ_f. Hence, by using a pair of Au microheaters with different widths and applying the two-dimensional heat flow model, the cross-plane and in-plane λ_f can be determined [12]. Due to the limited measurement capability of using the 'two-microheater' method, the cross-plane λ_f can be measured only.

3.2.4. Hall measurement

Hall measurement is usually performed to determine the resistivity, majority carrier polarity, carrier concentration, and mobility [7]. The Hall effect studies the behavior of charge carriers in the presence of magnetic and electric fields. In this condition, the charge carriers will be influenced by two forces, magnetic and electric, which are governed by Lorentz force:

$$\vec{F} = e(\vec{E} + \vec{v} \times \vec{B}), \tag{3.4}$$

where e is the charge of the electron, $\vec{E}$ is the electric field, $\vec{v}$ is the velocity, and $\vec{B}$ is the magnetic field. In Hall measurement, four electrodes are connected to the specimen, so a current (I), driven by $\vec{E}$, flows in a direction perpendicular to $\vec{B}$ by two non-adjacent electrodes (Figure 3.6). The Lorentz force deflects the carriers toward one side of the sample, creating an electric field in the remaining electrodes that is perpendicular to both $\vec{B}$ and $\vec{E}$.

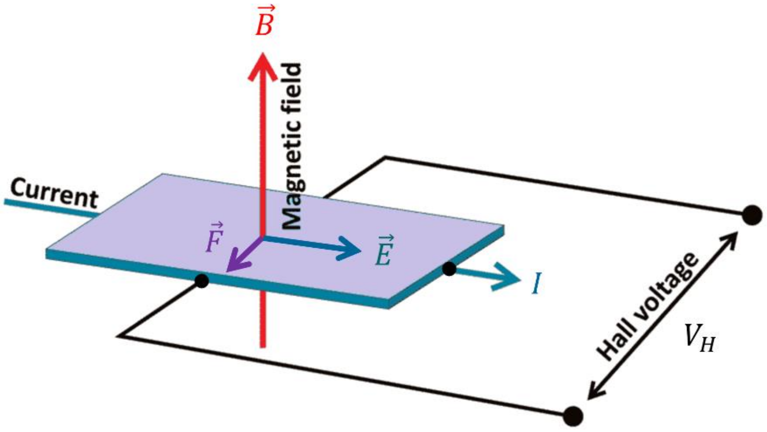

Figure 3.6. Schematic representation illustrates Hall effect.

The Hall voltage can be derived as [7]:

$$V_H = \frac{BI}{ent}, \tag{3.5}$$

where n is the carrier concentration, and t is the film thickness.

All the Hall measurements presented in this work were performed in a physical properties measurement system (PPMS) (Quantum Design, Inc., USA) at *KAUST core labs*. Each film was measured in a magnetic field from -5 to +5 Tesla at room temperature in the dark. All values of carrier concentrations reported in this work were extracted from the V_H-I curves (see Equation 3.5) after applying the magnetoresistance correction.

3.3 Materials Characterization

This section describes the materials characterization techniques used in this work. The techniques were used to explore the crystal structure and orientation, surface morphology and roughness, and the composition of elements in the films and superlattices.

3.3.1. X-ray Diffraction

X-ray Diffraction (XRD) is a fundamental characterization technique widely used in many research areas to reveal the crystal structure quality of materials under study. Since the wavelength of X-rays is comparable to the planar and atomic distances, they are very convenient for exploring the crystal structure of many classes of materials. The energetic X-rays can penetrate deep into the materials, and can be diffracted from the periodic arrays of atoms. XRD is based on the constructive interference of monochromatic X-rays diffracted from the crystals (Figure 3.7). Constructive interference occurs when the diffracted rays obey Bragg's condition which is given by:

$$n\lambda = 2d\ sin\theta, \tag{3.6}$$

where n is an integer, λ is the wavelength of X-rays, d is the distance between lattice planes, and θ is the angle of incidence of X-rays.

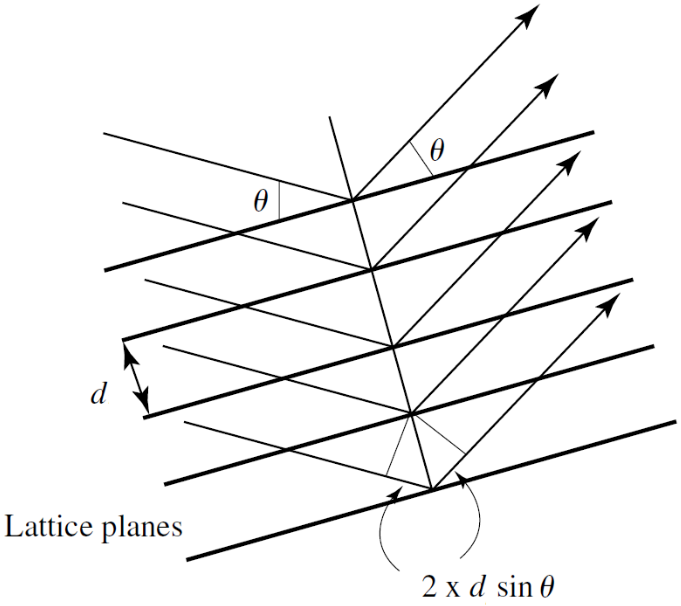

Figure 3.7. Diffraction of X-rays from lattice planes illustrating Bragg's law [15].

XRD patterns in this work were obtained using a high-resolution Bruker D8 Discover diffractometer, using CuKα1 (λ=1.5406 Å) radiation, at *KAUST core labs*. XRD was primarily used to identify the growth quality, the lattice constant, and the crystallite size of the oxide thin films with respect to their relative substrates. Two experimental configurations were performed in this dissertation: Bragg-Brentano and Φ-scan.

Figure 3.8 shows a schematic diagram of XRD scan experiment for thin film on a substrate. In Bragg-Brentano geometry, all rotation angles of the system parts are fixed in their initial positions (usually 0˚) except the X-ray source and the detector (θ angles) move simultaneously at the same rotation speed allowing diffraction from planes parallel to the film-substrate interface only. In Φ-scan, ψ and θ are fixed to specific values where other lattice planes can cause the diffraction of X-rays which is not achievable in Bragg-Brentano geometry. Φ-scan allows the study of the in-plane epitaxial relationships between the film and substrate, and it reveals the quality of film texturing.

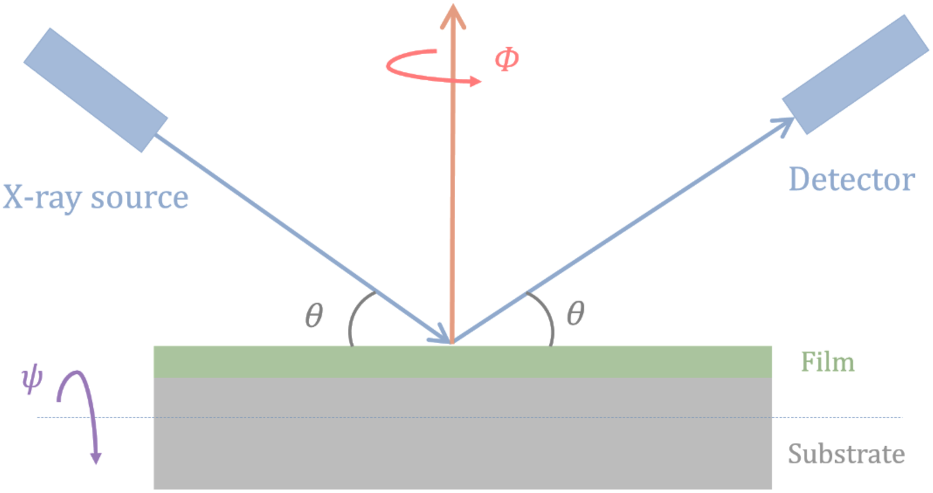

Figure 3.8. Schematic diagram of XRD scan experiment for thin film on a substrate.

3.3.2. Additional Characterization Techniques

This section reviews the additional characterization techniques used in this work in order to comprehensively study oxide thin films and superlattices. The basic principles of these techniques can be found elsewhere [16, 17].

3.3.2.1. Scanning Electron Microscope

Scanning electron microscopy (SEM) was used in this work to study the structure and surface morphology of oxide films. It was primarily used for top view imagining of doped $SrTiO_3$ films in Chapter 6. Exploring the microstructure and the surface morphology of the films is crucial in explaining the scattering events that dominates the electrical transport. SEM images were observed by FEI Nova NanoSEM at *KAUST core labs*.

3.3.2.2. Atomic Force Microscopy

Atomic Force Microscope (AFM) is a technique which enables us not only to study the surface morphology and microstructure of the films but also it is capable of measuring the roughness and identifying the individual surface atoms. At *KAUST core labs*, Agilent 5400 SPM AFM was used to discover the surface microstructure of doped $SrTiO_3$ and ZnO films studied in Chapter 4 and 5, respectively.

3.3.2.3. Transmission Electron Microscope

Transmission Electron Microscope (TEM) was used to confirm the epitaxial growth of $SrTiO_3$ superlattices which were studied in Chapter 7. At *KAUST core labs*, FEI high base Titan TEM was used to characterize the superlattices. Special experimental procedure was followed to perform proper TEM characterization, and it is discussed in Chapter 7.

3.3.2.4. Rutherford Backscattering Spectroscopy

The composition of the films was measured by high-resolution Rutherford backscattering spectrometry (HRBS-500, Kobelco, Japan), after depositing identical films with thickness less than 100 nm, on Al_2O_3 substrates, since accurate measurement of composition of films on $LaAlO_3$ (LAO) substrates was difficult due to the high atomic number of La. For the HRBS studies, He^+ ion beam with energy 400 keV was used and the backscattered ions were collected at an angle of 169°. Simulations were performed using a custom-built code (Kobelco, Japan).

3.4 References

1. H.M. Smith and A.F. Turner,*"Vacuum Deposited Thin Films Using a Ruby Laser",* Applied Optics, 4, 147 (1965).
2. D. Dijkkamp, T. Venkatesan, X.D. Wu, S.A. Shaheen, N. Jisrawi, Y.H. Min-Lee, W.L. McLean, and M. Croft,*"Preparation of Y-Ba-Cu oxide superconductor thin films using pulsed laser evaporation from high Tc bulk material",* Applied Physics Letters, 51, 619 (1987).
3. D.H. Lowndes, D.B. Geohegan, A.A. Puretzky, D.P. Norton, and C.M. Rouleau,*"Synthesis of Novel Thin-Film Materials by Pulsed Laser Deposition",* Science, 273, 898 (1996).
4. *Michigan State University, Department of Electrical and Computer Engineering*. Available from: https://www.egr.msu.edu/eceshop/testingfacility/.
5. *Neocera Company*. Available from: http://www.neocera.com/thin_film.html.
6. K. Wasa, M. Kitabatake, and H. Adachi, *"Thin Film Materials Technology: Deposition of Compound Thin Films"*, K.W.K. Adachi, Editor William Andrew Publishing, 191-403 (2004).
7. D.K. Schroder, *"Semiconductor Material and Device Characterization"*, John Wiley & Sons, Inc., 1-59 (2005).
8. C. Wood, A. Chmielewski, and D. Zoltan,*"Measurement of Seebeck coefficient using a large thermal gradient",* Review of Scientific Instruments, 59, 951 (1988).
9. J. Martin, T. Tritt, and C. Uher,*"High temperature Seebeck coefficient metrology",* Journal of Applied Physics, 108, 121101 (2010).
10. F.J. Blatt, D.J. Flood, V. Rowe, P.A. Schroeder, and J.E. Cox,*"Magnon-Drag Thermopower in Iron",* Physical Review Letters, 18, 395 (1967).
11. A.T. Burkov, A. Heinrich, P.P. Konstantinov, T. Nakama, and K. Yagasaki,*"Experimental set-up for thermopower and resistivity measurements at 100-1300 K",* Measurement Science and Technology, 12, 264 (2001).
12. T. Borca-Tasciuc, A.R. Kumar, and G. Chen,*"Data reduction in 3ω method for thin-film thermal conductivity determination",* Review of Scientific Instruments, 72, 2139 (2001).
13. D.G. Cahill,*"Thermal conductivity measurement from 30 to 750 K: the 3 omega method",* Review of Scientific Instruments, 61, 802 (1990).
14. S.-M. Lee and D.G. Cahill,*"Heat transport in thin dielectric films",* Journal of Applied Physics, 81, 2590 (1997).
15. W.C. Alexander J. Blake, Jacqueline M. Cole, John S.O. Evans, Peter Main, Simon Parsons, and David J. Watkin, *"Crystal Structure Analysis: Principles and Practice"*. Second ed: Oxford University press (2009).
16. H.R. Verma, *"Atomic and Nuclear Analytical Methods"*. Springer Berlin Heidelberg. 91-141 (2007).
17. Y. Leng, *"Materials Characterization: Introduction to Microscopic and Spectroscopic Methods"*. Second ed: Wiley (2013).

Chapter 4.

Crystal orientation dependent thermoelectric properties of highly oriented aluminum-doped zinc oxide thin films

(Reproduced with permission from *Appl. Phys. Lett. 102, 053507*. Copyright 2013, AIP Publishing LLC)

4.1 Abstract

We demonstrate that the thermoelectric properties of highly oriented Al-doped zinc oxide (AZO) thin films can be improved by controlling their crystal orientation. The crystal orientation of the AZO films was changed by changing the temperature of the laser deposition process on $LaAlO_3$ <001> substrates. The change in surface termination of the $LaAlO_3$ substrate with temperature induces a change in AZO film orientation. The anisotropic nature of electrical conductivity and Seebeck coefficient of the AZO films showed a favored thermoelectric performance in c-axis oriented films. These films gave the highest power factor of 0.26 W m^{-1} K^{-1} at 740 K.

4.2 Introduction

Zinc oxide (ZnO) has attracted considerable attention in many applications as a semiconductor oxide due to its abundance, non-toxicity, and low cost. ZnO is a wide band gap semiconductor with a direct band gap of 3.3 eV at room temperature [1]. The electrical properties of ZnO can be changed from insulator through *n*-type semiconductor to metal by controlling its doping level, while maintaining optical transparency, which makes it useful for transparent electrodes in flat-panel displays and solar cells. In addition, ZnO, has better stability at high temperature than the conventional thermoelectric (TE) materials (such as Bi_2Te_3 and PbTe), which can readily oxidize in such atmospheres. Owing to its superior stability compared to those heavy metal based compounds, ZnO has potential for high temperature TE energy conversion. ZnO-based oxide TE materials show a relatively high TE power factor, *PF,* (power factor in units of W m^{-1} K^{-1} is taken as the numerator of the figure of merit *ZT*, $ZT=(\sigma S^2T)/\lambda$, where σ is the electrical conductivity, S is the absolute Seebeck coefficient, T is the absolute temperature, and λ is the thermal conductivity), which is competitive to the conventional TE materials. Undoped ZnO is an *n*-type semiconductor. However, by doping with Al^{3+}, σ can be increased by more than three orders of magnitude at room temperature, changing the conduction behavior from semiconducting to metallic [2]. However, the overall TE performance of AZO is relatively low because of its high λ [3]. Therefore, enhancing the electronic transport is crucial for improving the TE properties of AZO films. Unfortunately, possible improvement in electron transport properties is often limited by the trade-off between σ and S. For example, high σ up to 7×10^3 S cm^{-1} was reported for Ga-doped ZnO epitaxial films prepared by pulsed laser deposition (PLD) , but with a low S around -11 μV/K [4], whereas a high S of -140 μV K^{-1} was reported for PLD-grown amorphous ZnO films, but with a low σ of 100 S cm^{-1} [5]. Optimizing the growth conditions is hence important to improve the TE power factor of ZnO-based thin films.

It is known that ZnO has an anisotropic electrical transport because of the ionic nature of the Zn–O bond and because of its wurtzite crystal structure, which lacks inversion symmetry. Thus, it may be possible to obtain better electrical transport and TE properties using ZnO-based films with specific crystal orientations. It has been reported that the in-plane electrical transport in the c-axis oriented ZnO films is enhanced compared to the a-axis oriented ones [6-8]. A number of methods can be used to change the crystal orientation of ZnO. For example, $SrTiO_3$ single crystal substrates with different orientations can be used to alter the crystal orientation of PLD-grown ZnO films [6]. The crystal orientation of AZO ceramics can also be controlled by applying a high magnetic field [7].

In this work, we have altered the crystal orientation of AZO films on $LaAlO_3$ (LAO) substrates, by changing the substrate temperature (T_S) and for doing so, we have used a well-known effect whereby the surface termination of LAO substrates change at different temperatures [9]. In this approach, the same substrate material can be used, which has the advantage that any variations in the TE properties of the AZO films are largely driven by the change in the film orientation itself, and not by interactions with the substrate material.

4.3 Experimental Section

AZO films were deposited by PLD (Neocera, Beltsville, MD) using a KrF excimer laser (λ=248 nm, pulse duration ~20 ns, repetition rate =10 Hz). Films were deposited by ablation of a 4N purity Al_2O_3 (2 wt.%) doped ZnO target at laser fluence of 3 J cm^{-2} $pulse^{-1}$. The target was held on a rotating carousel to ensure a uniform ablation. In order to create sufficient oxygen vacancies and increase carrier concentration in the films, 20 mTorr of Ar was introduced as a reducing gas, using a mass flow controller. Films were deposited on <001> oriented LAO substrates (MTI corporation, USA) of dimensions 10x10x0.5 mm^3 with a_{LAO}= 3.82 Å, held at different T_s values of 300, 425, 600, 800 and 1000 K and are denoted as films A, B, C, D and E, respectively. The thickness of the films was around 100 nm as measured by a spectroscopic ellipsometer. The phase purity of the films was determined from the analysis of θ-2θ (Bragg-Brentano) scan using an x-ray diffractometer (D8 Bruker, AXS System, Germany). Φ-scan was done for an asymmetric (110) and (001) diffraction of the LAO substrate and AZO film, respectively. When ψ, the tilt angle of the surface normal of the film, was 45° and 2θ was fixed at 33.4°, and when ψ was 30° and 2θ was fixed at 31.77°, the respective Φ-scans for LAO and AZO were obtained by rotating the film (0°–360°) around the surface normal. σ and S were measured, on the same sample, from 300–740 K by using respectively the linear four-probe and the differential methods, under Ar/H_2 (96% Ar and 4% H_2) ambient using a commercial setup (RZ2001i, Ozawa Science Co Ltd., Nagoya, Japan). At any temperature, σ was measured first, followed by S by introducing a ΔT of ~4–10 K, between the voltage probes. The measurements of σ and S were then repeated at a higher sample temperature, thereby enabling studies on change in transport properties during heating. Room temperature Hall effect measurements were carried out using a physical property measurement system (PPMS) (Quantum Design, Inc., USA). The surface morphology of the films was obtained by using an atomic force microscope (AFM) (Agilent, 5400, USA).

4.4 Results and Discussion

Figure 4.1 shows θ-2θ x-ray diffraction (XRD) patterns for the AZO films. The patterns confirm that AZO films with a wurtzite crystal structure (Figure 4.1(a)) are formed irrespective of T_s. The diffraction peaks of the {001} planes from the LAO substrate (marked 'S') and two reflections from AZO planes can be seen. Small diffraction peaks (marked by asterisk) are observed in all patterns at 52.55° which can be attributed to small concentration of secondary phases (Al_2O_3 (024)). However, since the intensity of this reflection is small and similar for all the films, the effect of the secondary phases in determining the properties is neglected. Film A has a very small peak corresponding to the (002) reflection compared to film B (marked by the arrow), indicating that the growth direction is preferentially oriented along the c-axis (c-AZO) and film A is less crystallized compared to film B. This should not be surprising since film A was deposited without substrate heating (at 300 K). On the other hand, films C and E have a single peak corresponding to (110), which indicates a growth along the a-axis (a-AZO). Film D exhibits both (002) and (110) orientations. The dependence of crystal orientation of the AZO films on T_s can be attributed to the change in surface termination of the LAO substrate with temperature. LAO has a layered crystal structure with alternating La–O and Al–O planes. It has been clearly demonstrated [9] that depending on temperature, the surface termination of LAO varies. From 300 K to ~423 K, the surface is terminated by the Al–O plane while at temperatures above ~523 K, the termination is by the La–O plane. Mixed terminations containing Al, La, and O have been reported in the intermediate region of 423–523 K. The O–O bonding distances in the Al–O and La–O terminated planes on LAO (100) are 2.68 and 5.36 Å [10], respectively, while the lattice constants of AZO are a_{AZO} = 3.25 Å and c_{AZO} = 5.2 Å. If the O sites on LAO surface provide the base for Zn atoms of ZnO, one expects that the La–O terminated surface provides better match (3–5% lattice mismatch) for the growth of a-AZO at temperatures above 550 K (Figure 4.2(b)) as compared to the Al–O terminated surface because of the large lattice mismatch (94%). Also, growth of c-AZO is favored on Al–O surface, which occurs below 450 K (Figure 4.2(c)) [10]. The mixed orientation in film D is related to the formation of oxygen vacancies in the films at T_s >600 K (an effect which will be discussed in detail later), which tends to relax [11] the lattice causing the occurrence of both types of growth directions. The lattice constants obtained from XRD analysis are shown in Table 4.1. However, it has been reported [10, 12] that mixed orientation of PLD-grown ZnO films can be obtained at different ranges of T_s. In these reports, the ambient gas used (20–30 mTorr of O_2) was different compared to ours (20 mTorr of Ar). The physical properties of our films must hence be expected to be different compared to the reported ones, since ambient gas for the PLD process is a crucial parameter that changes the physical properties of oxide films [13].

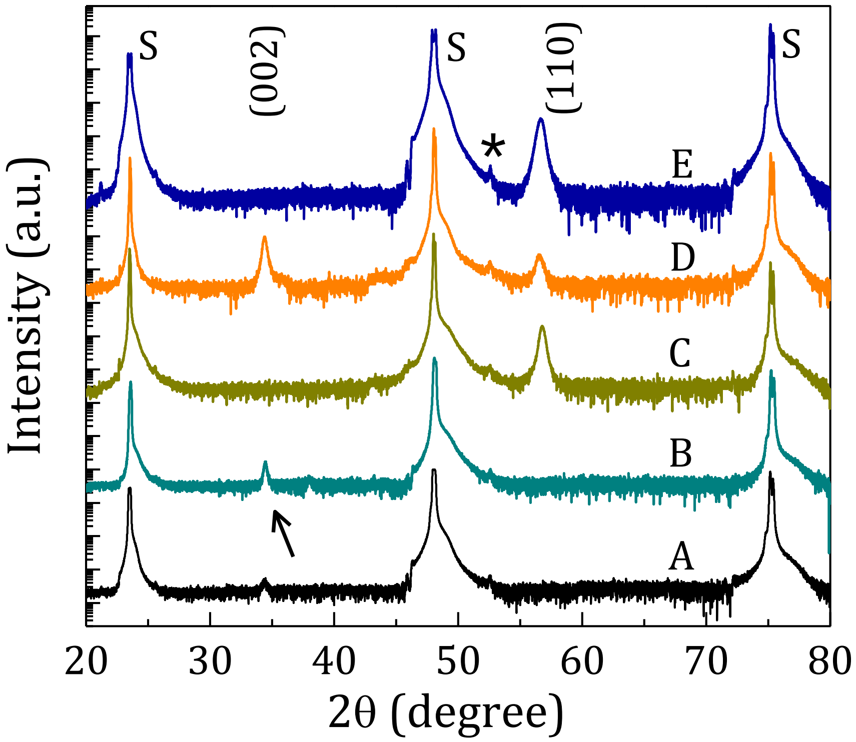

Figure 4.1. θ-2θ XRD pattern for AZO thin films grown on LAO substrate at different temperatures T_s = 300, 425, 600, 800, and 1000 K which are denoted as films A, B, C, D, and E respectively.

Figure 4.2(d) shows the Φ-scan patterns for LAO substrate and films C, E (both, a-AZO), wherein four peaks with almost equal intensity, and spaced by 90° can be observed, indicating a highly textured growth. The shift in peak positions of the Φ-scan patterns corresponding to a-AZO {100} and LAO {110} is 45°, indicating that these two families of planes intersect the substrate surface with an angular difference of 45°. Therefore, the epitaxial relationships for a-AZO are [001] AZO || [110] LAO and [001] AZO || [-110], as shown in Figure 4.2(b). It is evident that films C and E, which were grown respectively at 600 and 1000 K, have the same in-plane epitaxy.

However, the respective full width at half maximum (FWHM) values of the peaks of Φ-scan patterns of films C and E are 5.3° and 4.35°, indicating that film E is more textured than film C. For the c-AZO films, the Φ-scans, despite repeated attempts at different tilt angles, did not show any peaks, indicating that the crystallites are randomly distributed in the plane of the LAO substrate while maintaining their c-axis perpendicular to the substrate surface (Figure 4.2(c)). The presence of a single (002) peak in the θ-2θ scan and the absence of any peaks in the Φ-scan indicate that film B is fibre-textured. Fibre-texture arises when the c-axis of the film is fixed perpendicular to the substrate, but the in-plane axes are randomly rotated [14]. However, a ring pattern expected for fibre-textured films was not observed in the pole figures for {101} poles, which occur at ψ of 61.6°, which may be attributed to the low crystallinity of the films.

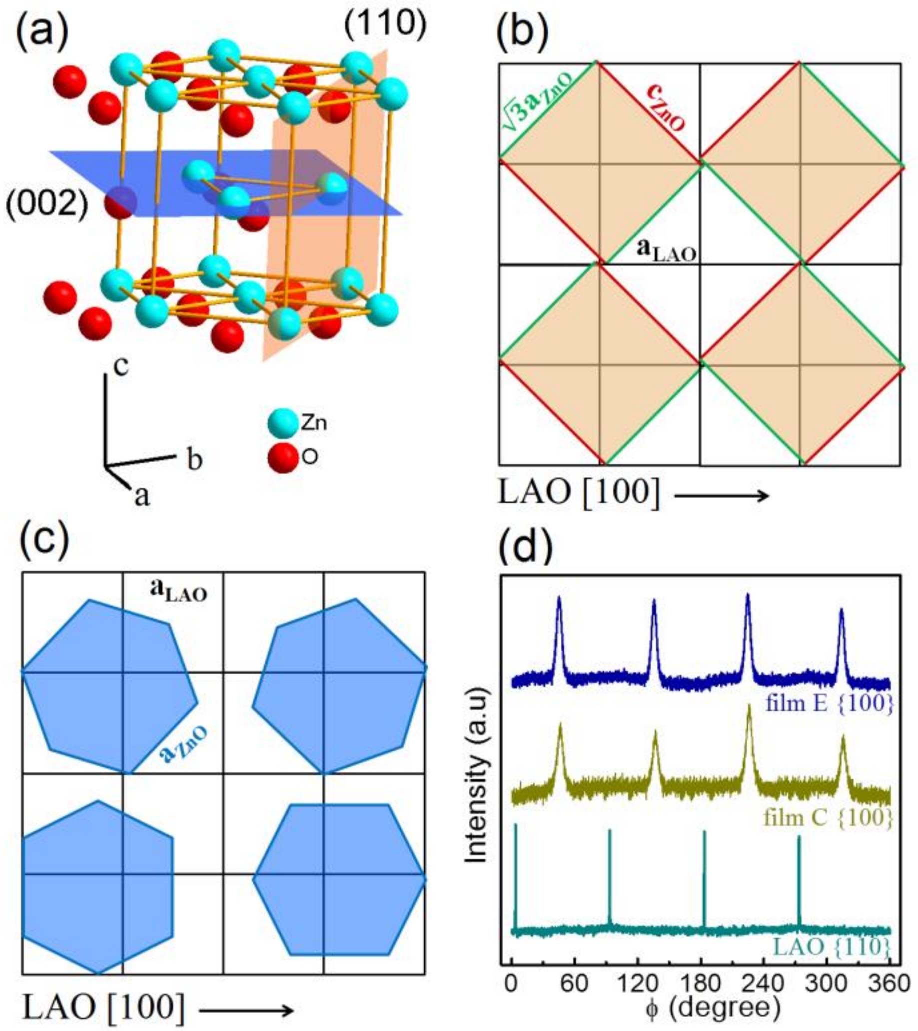

Figure 4.2. (a) ZnO wurtzite crystal structure with the (002) and (110) planes highlighted. (b) Lattice arrangement at the interface between (b) a-AZO film and La–O terminated LAO surface and (c) c-AZO film and Al–O terminated LAO surface. (d) XRD Φ-scan for {100} of film C and film E (a-AZO) and {110} of LAO substrate.

The σ-T dependence of AZO films deposited at different T_s is plotted in Figure 4.3. Since the LAO substrate is insulating even after the film deposition (as measured from the rear side), its contribution to σ of AZO films can be neglected. Thus, the two possible sources for electronic charge carriers in the films are oxygen vacancies in AZO and the substitutional doping of Al^{3+} ions on the Zn^{2+} sites. Due to the presence of the charge carriers in the conduction band, all films exhibit semiconductor characteristics, with σ increasing with temperature. The most prominent feature seen in Figure 4.3 is the dependence of σ on the crystal orientation. Compared to the a-AZO films, the c-AZO film (film B) shows higher σ in the entire range of temperature. However, film A, though also c-oriented, exhibits the lowest σ at 300 K, as shown in Figure 4.3, possibly due to significant electron scattering, owing to the incomplete crystallization, as may be expected for room temperature laser deposition. Furthermore, film A has the lowest electrical mobility (Table 4.1) which is also expected. It is well known that the electron effective mass is strongly dependent on the conduction direction in anisotropic crystals. For example, electrons have higher effective mass along c-axis than along a-axis in ZnO crystals [8]. The origin of this anisotropy is the lack of inversion symmetry and the ionic nature of the Zn–O bond, which results in a strong spontaneous bound polarization [15] along c-axis, the direction along which the Zn and O atoms are stacked alternately. This polarization can generate bound positive and negative charges on (001) Zn-polar and (00-1) O-polar surfaces, respectively. These bound polarization charges induce a Schottky barrier potential at every Zn-polar surface which reduces effective mass and σ along the c-axis [6, 16]. It has also been found [17] that though both c-polar planes and a-planes in ZnO accumulate electrons, owing to the spontaneous polarization the former accumulates more electrons. Since σ and Hall effect in our films were measured in-plane, the relevant effective mass that determines the transport is the in-plane effective mass, i.e., along directions in the c-plane of c-AZO film (film B) and along directions in the a-plane of a-AZO films (films C and E). Hence, one expects higher carrier concentration in c-AZO films compared to the a-AZO films, which is indeed observed (Table 4.1). Due to the combined effect of spontaneous polarization and the resultant increase in carrier concentration, c-AZO film (film B) exhibits a higher effective in-plane σ. Film C (a-AZO) has significantly lower values of σ not only due to the polarization effect along the c-axis and a resultant drop in carrier concentration, as discussed above, but also due to its small oxygen vacancy concentration, since it was deposited at T_s= 600 K. Compared to film C, film E was deposited at higher T_s (1000 K, which is much higher than the temperature at which oxygen vacancies are created in AZO, as explained later) and hence the contribution of oxygen vacancies to its carrier concentration is higher, resulting in a higher σ for the entire range of temperature. Film D has lower electrical mobility (and hence lower σ) than film E since it has mixed crystal orientations (i.e., both c-AZO and a-AZO), which increases the scattering of the electrons. It may be noted that for a given crystal orientation, the carrier concentration increases with T_s, due to the increase in oxygen vacancy concentration of the films. From Table 4.1, it is also evident that the crystallite size and carrier concentration of the films increase after annealing. It may be noted that it is possible for two films with extreme crystalline qualities to have similar carrier concentration, but other transport properties will be significantly different (compare for instance, the mobility and electrical conductivity of films A and E).

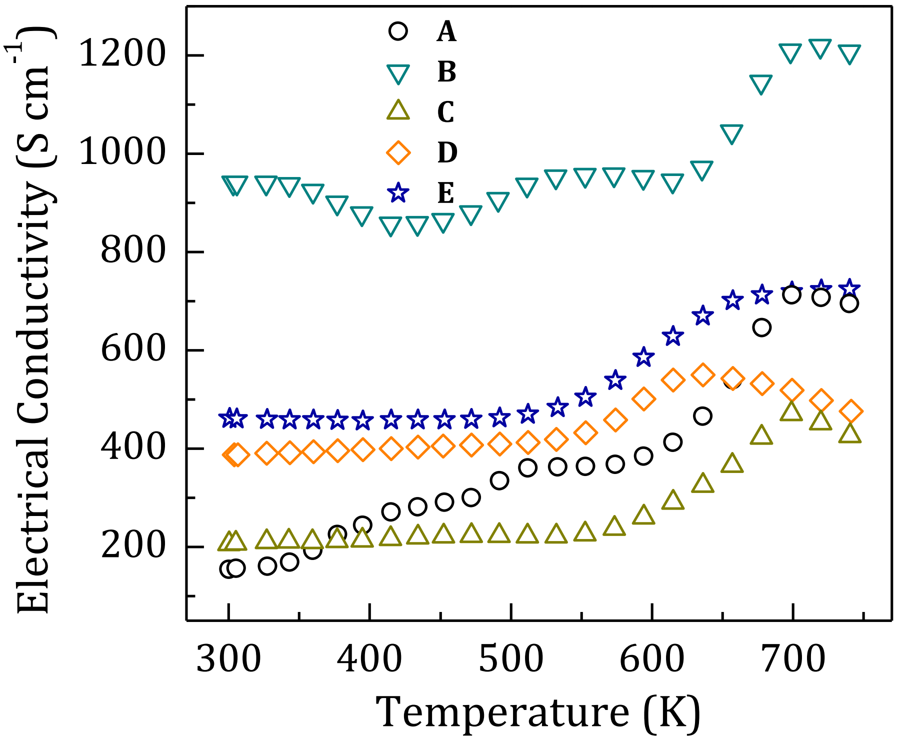

Figure 4.3. Electrical conductivity of AZO films grown at different substrate temperatures.

Another interesting feature observed in Figure 4.3 is the gradual increase in σ for all films, in the temperature range 550–700 K, irrespective of their crystal orientations. This change in σ is commonplace in oxide thermoelectrics, especially when measured in a reducing ambient such as Ar/H_2, and can be attributed to the creation of additional oxygen vacancies in the AZO films [18]. To prove this argument, we measured the carrier concentration (Table 4.1) for the as-grown films and the films subjected to TE measurements (annealed) up to 740 K in Ar/H_2. All of the annealed films have higher carrier concentration compared to the as-grown ones, as a direct consequence of oxygen vacancy creation during the annealing process, with each oxygen vacancy contributing two electrons towards conduction. It is also observed that above ~700 K, σ decreases with temperature since the films start to deteriorate at this temperature. We have observed a drastic drop (not shown here) in σ (from 830 to 430 S cm^{-1}), for an AZO film annealed up to 900 K.

Table 4.1 Measured and calculated transport properties of AZO thin films at 300 K for different substrate temperatures. The films were grown at different substrate temperatures, T_s = 300, 425, 600, 800, and 1000 K and are denoted by A, B, C, D, and E, respectively. Except in columns 5 and 7, the values shown are for the as-grown films. The calculated crystallite size for film D is reported respectively for c-AZO and a-AZO, for both as-grown and annealed films.

Sample	Lattice constant		Crystallite Size		n	n	σ	μ	S	PF
	a (Å)	c (Å)	(Å)	(Å)	(cm^{-3} × 10^{20})	(cm^{-3} × 10^{20})	(S cm^{-1})	(cm^{-2} v^{-1} s^{-1})	(μV K^{-1})	(W m^{-1} K^{-1})
A	-	5.205	220	250	7.90	8.85	154	1.22	-30	0.004
B	-	5.202	250	290	12.3	28.8	941	4.78	-25	0.018
C	3.244	-	190	210	1.74	4.82	207	7.43	-33	0.007
D	3.259	5.214	200, 160	210, 180	5.33	7.84	387	4.54	-30	0.011
E	3.252	-	150	170	5.26	5.56	461	5.48	-33	0.015

In TE thin films, the transport properties also depend critically on the microstructure. In order to differentiate between the effect of crystal orientation and the possible effect of microstructure on the electrical transport, AFM images of the films were obtained. Figure 4.4(a-e) show AFM phase images for all films. Evidently, the surface morphology of the films is different. The rms surface roughness of the films is however nearly identical (~4 nm). To correlate the microstructure with the electrical transport, films B, D, and E can be selected as examples. These films have grain sizes around 40, 65, and 80 nm, respectively. Assuming that microstructure plays a predominant role on the transport, one would expect film B to have lower σ

compared to films D and E, because of its smaller grain size, which enhances scattering and decrease mobility. But film B has the highest σ (Table 4.1), indicating that the scattering of the free electrons is not dominated by grain boundaries. Hence it is clear that crystal orientation of the AZO films, and not the microstructure, plays predominant role in determining the electrical transport properties of AZO.

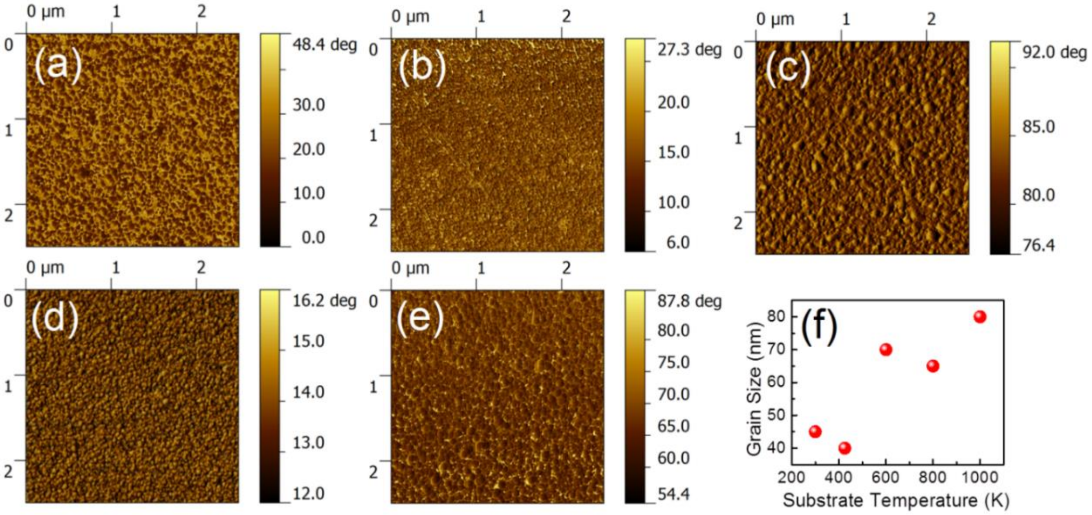

Figure 4.4. AFM phase images for AZO films: (a) film A, (b) film B, (c) film C, (d) film D, and (e) film E. (f) Grain size of films as a function of substrate temperature (T_s).

The temperature dependence of S is shown in Figure 4.5(a). All films have negative S coefficient indicating n-type conduction as a consequence of Al and oxygen vacancy doping of ZnO. The films (except film A) also exhibit a linear dependence of S on temperature up to around 550–600 K. Above $T \sim 600$ K, this linearity is no longer obeyed. A plausible explanation for the deviation from linearity is a change in the scattering mechanism of the free electrons. Above 600 K, oxygen vacancies are created in these oxides, as discussed earlier, which act as additional scattering centers. Film A has a different S-T dependence compared to other films, which can be explained by the enhanced electron scattering due to the low crystalline quality. Film C (a-AZO) has the highest S across the entire temperature range compared to the other films, a result which is consistent with the fact that it also had the lowest σ. It may be noted here that the electron effective mass is higher [8] along a-plane of AZO and the measurement of S was also done in-plane. On the other hand, film B (c-AZO) has the lowest S because of the lower electron effective mass along c-plane. In contrast, film D has lower S (lower σ) than film E (higher σ). Since film D has both types of crystal orientations, a-AZO and c-AZO, and the total electronic effective mass is a combination of the respective c-axis and a-axis components of effective mass. Therefore, the a-axis component reduces the total electron effective mass in film D, and hence results in a lower S.

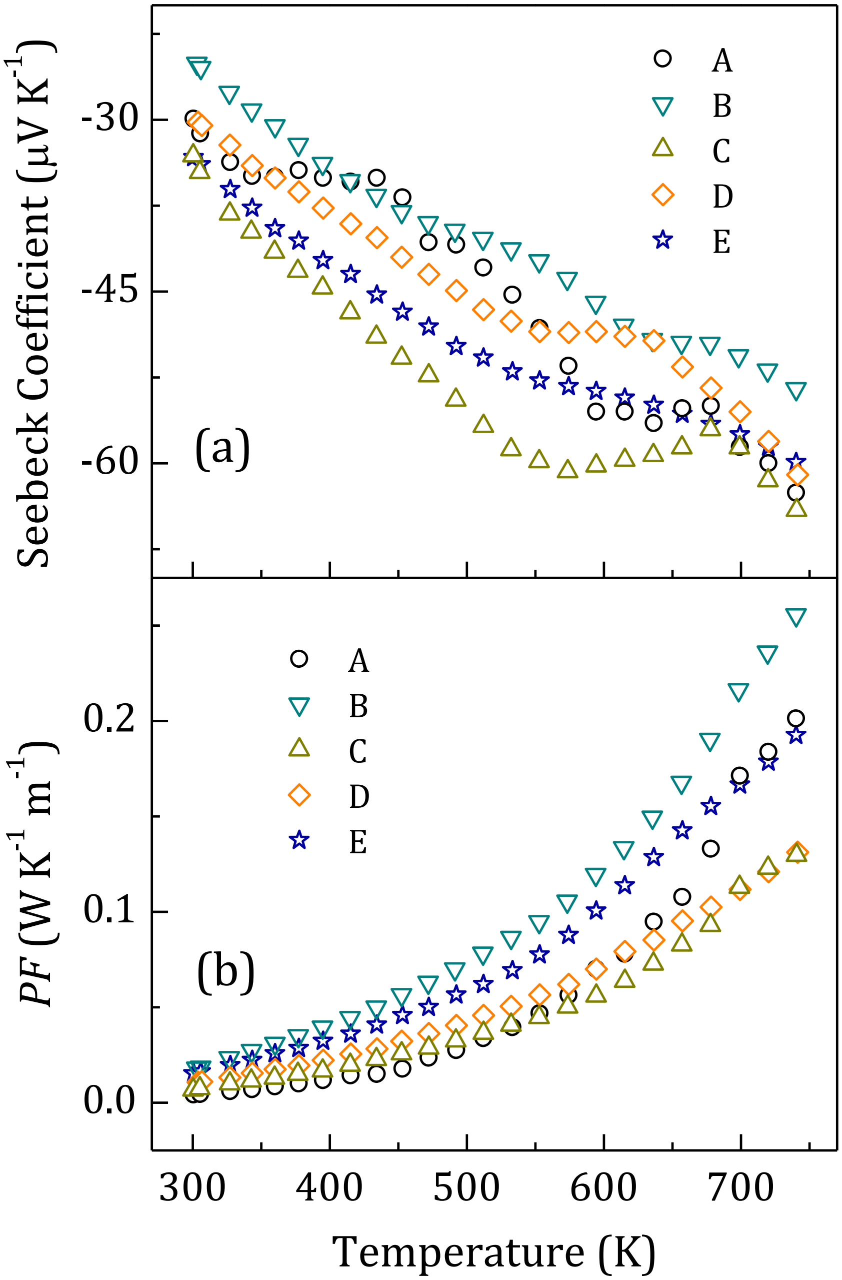

Figure 4.5. The temperature dependence of (a) Seebeck coefficient and (b) power factor (***PF***) for AZO films grown at different substrate temperatures.

The temperature dependence of the derived *PF* is plotted in Figure 4.5(b). Film B exhibits the best *PF* compared to other films (0.26 W m^{-1} K^{-1}) at 740 K. The obtained value is higher than those reported for undoped ZnO film (0.12 W m^{-1} K^{-1}) [5] at 650 K, and Ga doped ZnO films (2.5×10^{-4} W m^{-1} K^{-1}) at 300 K [4]. The improved *PF* is mainly due to the enhanced electronic conductivity of the c-axis oriented film.

4.5 Conclusions

In summary, we showed the direct dependence of the thermoelectric properties of AZO films on crystal orientation. The crystal orientation of the AZO films can be controlled by changing the substrate temperature during deposition. To induce a change in the AZO crystal orientation, we used a well-established effect wherein LAO substrates change their surface termination at different temperatures. The c-AZO film (grown at 425 K) shows the best thermoelectric *PF* (0.26 W K^{-1} m^{-1} at 740 K), which is attributed mainly to the improvement of electrical conductivity brought in by the spontaneous polarization along the c-axis, which also increases the carrier concentration. The critical dependence of thermoelectric properties on the controllable crystal orientation offers a pathway for the design of thin film thermoelectric devices using optimized AZO films.

4.6 References

1. V. Srikant and D.R. Clarke,*"On the optical band gap of zinc oxide",* Journal of Applied Physics, 83, 5447 (1998).
2. M. Snure, D. Toledo, P. Slusser, and A. Tiwari, *"Conduction in Degenerately Doped $Zn_{1-x}Al_xO$ Thin Films GaN and ZnO-based Materials and Devices"*, S. Pearton, Editor Springer Berlin Heidelberg, 349-360 (2012).
3. M. Ohtaki, T. Tsubota, K. Eguchi, and H. Arai,*"High-temperature thermoelectric properties of $(Zn_{1-x}Al_x)O$",* Journal of Applied Physics, 79, 1816 (1996).
4. M. Snure and A. Tiwari,*"Structural, electrical, and optical characterizations of epitaxial $Zn_{1-x}Ga_xO$ films grown on sapphire (0001) substrate",* Journal of Applied Physics, 101, 124912 (2007).
5. M.O. Yoshihiro Inoue, Toshio Kawahara, Yoichi Okamoto and Jun Morimoto,*"Thermoelectric properties of Amorphus Zinc Oxide thin films fabricated by pulsed laser deposition",* Materials Transactions, 46, 1470 (2005).
6. K.Z. Gaofeng Sun, Yunlong Wu, Yuhang Wang, Na Liu and Liuwan Zhang,*"Polar dependent in-plane electric transport of epitaxial ZnO thin films on SrTiO3 substrates",* Journal of Physics: Condensed Matter, 24, 295801 (2012).
7. Y.K. Hisashi Kaga, Satoshi Tanaka, Atsushi Makiya, Zenji Kato, Keizo Uematsu and Koji Watari,*"Preparation and Thermoelectric Property of Highly Oriented Al-Doped ZnO Ceramics by a High Magnetic Field",* Japanese Journal of Applied Physics, 45, L1212 (2006).
8. K.-F. Lin, C.-J. Pan, and W.-F. Hsieh,*"Calculations of electronic structure and density of states in the wurtzite structure of $Zn_{1-x}Mg_xO$ alloys using sp3 semi-empirical tight-binding model",* Applied Physics A, 94, 167 (2009).
9. J. Yao, P.B. Merrill, S.S. Perry, D. Marton, and J.W. Rabalais,*"Thermal stimulation of the surface termination of $LaAlO_3$ {100}",* The Journal of Chemical Physics, 108, 1645 (1998).
10. Y.-T. Ho, W.-L. Wang, C.-Y. Peng, M.-H. Liang, J.-S. Tian, C.-W. Lin, and L. Chang,*"Growth of nonpolar (110) ZnO films on $LaAlO_3$ (001) substrates",* Applied Physics Letters, 93, 121911 (2008).
11. A. Janotti and C.G.V.d. Walle,*"Oxygen vacancies in ZnO",* Applied Physics Letters, 87, 122102 (2005).
12. D.-H. Cho, J.-H. Kim, B.-M. Moon, Y.-D. Jo, and S.-M. Koo,*"Control of a- and c-plane preferential orientations of ZnO thin films",* Applied Surface Science, 255, 3480 (2009).
13. S.S. Kim and B.-T. Lee,*"Effects of oxygen pressure on the growth of pulsed laser deposited ZnO films on Si (001)",* Thin Solid Films, 446, 307 (2004).
14. C. Detavernier, A.S. Ozcan, J. Jordan-Sweet, E.A. Stach, J. Tersoff, F.M. Ross, and C. Lavoie,*"An off-normal fibre-like texture in thin films on single-crystal substrates",* Nature, 426, 641 (2003).
15. F. Bernardini, V. Fiorentini, and D. Vanderbilt,*"Spontaneous polarization and piezoelectric constants of III-V nitrides",* Physical Review B, 56, R10024 (1997).

16. M.W. Allen, P. Miller, R.J. Reeves, and S.M. Durbin,*"Influence of spontaneous polarization on the electrical and optical properties of bulk, single crystal ZnO",* Applied Physics Letters, 90, 062104 (2007).
17. M.W. Allen, C.H. Swartz, T.H. Myers, T.D. Veal, C.F. McConville, and S.M. Durbin,*"Bulk transport measurements in ZnO: The effect of surface electron layers",* Physical Review B, 81, 075211 (2010).
18. T. Hiramatsu, M. Furuta, T. Matsuda, C. Li, and T. Hirao,*"Behavior of oxygen in zinc oxide films through thermal annealing and its effect on sheet resistance",* Applied Surface Science, 257, 5480 (2011).

Chapter 5.

Laser energy tuning of carrier effective mass and thermopower in epitaxial oxide thin films

(Reproduced with permission from *App. Phys. Lett. 100, 162106*. Copyright 2012, AIP Publishing LLC)

5.1 Abstract

The effect of the laser fluence on high temperature thermoelectric properties of the La^{3+} doped $SrTiO_3$ (SLTO) thin films epitaxially grown on $LaAlO_3$ <001> substrates by pulsed laser deposition is clarified. It is shown that oxygen vacancies that influence the effective mass of carriers in SLTO films can be tuned by varying the laser energy. The highest power factor of 0.433 W K^{-1} m^{-1} has been achieved at 636 K for a film deposited using the highest laser fluence of 7 J cm^{-2} $pulse^{-1}$.

5.2 Introduction

$SrTiO_3$ (STO) is a promising n-type oxide suitable for high-temperature thermoelectric applications [1-5]. The melting point [6] of STO is 2353 K making it applicable at high temperatures, unlike the heavy metal based materials such as Bi_2Te_3 and PbTe, which are not stable at temperatures in excess of 1000 K. Moreover, the constituents of STO are all naturally abundant compared to other conventional thermoelectric materials. The electrical conductivity of STO can be easily varied from insulating to metallic by the substitutional doping with La^{3+} or Nb^{5+} and also by creating oxygen vacancies [2, 4]. In spite of all the attractive features, the figure of merit ZT ($ZT=\sigma S^2 T/\lambda$, where σ is the electrical conductivity, S is the Seebeck Coefficient, T is the absolute temperature, and λ is the thermal conductivity) of STO is smaller than that of the heavy metal based materials since STO has a relatively high thermal conductivity (3–10 W m^{-1} K^{-1}) [1]. Recently, several research groups reported relatively high ZT for STO with La^{3+} doping (0.21 at 750 K) [7], Dy^{3+} and La^{3+} doping (0.36 at 1045 K) [8]. Considerable improvement in ZT is required to make STO a practical thermoelectric material and one way to do so is to reduce the thermal conductivity by nano structuring or doping with elements that enhance mass-fluctuation scattering. On the other hand, enhancing the electron transport properties is often limited by the trade-off relationship between σ and S in terms of electrical mobility (μ). For example, with increasing μ, σ increases while S decreases. Optimizing the growth conditions of the thin films is hence important to achieve the best power factor. The oxygen content and hence the carrier concentration (n) play a vital role in detemining the physical properties of the films. The usual sources of oxygen in oxide films grown by pulsed laser deposition (PLD) are the background gas and the substrate [9, 10]. It has been reported that Hall mobility of carriers at room temperature decreases as oxygen pressure increases, and hence oxygen partial pressure strongly affect the electrical transport properties of the PLD grown SLTO thin films [9]. Another approach to improve the power factor is by forming high density two-dimensional electron gas confined in a very thin layer of STO to produce a large value of $|S|$ (850 μV K^{-1}) without reducing σ [1]. The effective mass (m^*) of electrons is an important physical quantity that the electrical properties depend on. By changing the dopant concentration, m^* can be varied. In STO single crystals, m^* has been reported to vary in the range 6–6.6 m_0 and 1.1–1.6 m_0 for La^{3+} [3, 4] and in the range 7.3–7.7m_0 for Nb^{5+} [4] dopants.

In this work, we report the role of laser fluence in determining the oxygen content in STO based thermoelectric thin films. X-ray diffraction (XRD) and Atomic Force Microscopy (AFM) have been used to characterize the thin films. The temperature dependence of σ and S has been measured for three different laser fluences. The electrical transport properties at 300 K have been determined by using a physical property measurement system (PPMS). The observed results are explained based on the dependence of m^* on the oxygen content of the films.

5.3 Experimental Section

$Sr_{0.98}La_{0.02}TiO_{3-\delta}$ (SLTO) films were deposited by PLD (Neocera, Beltsville, MD) using a KrF excimer laser (λ=248 nm, pulse duration ~20 ns, repetition rate =10 Hz). Films were deposited by ablation of a 4N purity SLTO target (Testbourne Ltd., England) at three different laser fluences (7, 6, and 5 J cm^{-2} $pulse^{-1}$) and are denoted as films I, II and III respectively. The target was held on a rotating carousel to ensure a uniform ablation from the target surface. In order to create sufficient oxygen vacancies, 20 mTorr of Ar was introduced as a reducing gas. The gas flow was regulated by a mass flow controller. Films were deposited on (001) oriented $LaAlO_3$ (LAO) substrates (MTI corporation, USA) of dimensions 10x10x0.5 mm^3 with a_{LAO}= 3.82 Å, held at a temperature of 875 °C. The thickness of the films is around 500 nm as measured by a spectroscopic ellipsometer. The phase purity of the thin films was determined from the analysis of θ–2θ (Bragg-Brentano) and Φ (phi) scans using an X-ray diffractometer (D8 Bruker, AXS System, Germany). Φ-scan was done for an asymmetric (110) diffraction of the SLTO thin film on LAO substrate. When ψ, the tilt angle of the surface normal of the film, was 45˚ and 2θ was fixed at 32.42˚, Φ-scan result was obtained by rotating the film (0˚ –360˚) around the surface normal. σ and S were measured from 300–1000 K by using respectively the linear four-probe and the differential methods, under Ar/H_2 (96% Ar and 4% H_2) ambient using a commercial setup (RZ2001i, Ozawa Science Co Ltd., Nagoya, Japan). Room temperature Hall Effect was measured by using the PPMS (Quantum Design, Inc., USA). The surface morphology of the films was obtained by using AFM (Agilent, 5400, USA).

5.4 Results and Discussion

Figure 5.1(a) shows θ-2θ XRD patterns for the films. The diffraction peaks of the {001} planes from LAO (marked 'S') and SLTO can be seen and reflections from other crystalline orientations are of negligible intensity, indicating a preferential epitaxial growth of the films on the substrate. Figure 5.1(b) shows the Φ-scan for SLTO on LAO wherein four peaks with almost equal intensity spaced by 90˚ can be observed. The full width at half maximum (FWHM) of the peaks is 0.69˚, indicating a low mosaic spread and a high quality of the epitaxial thin film growth. Fine scans in the θ-2θ geometry were done for (002) reflection from SLTO (inset to Figure 5.1(a)) to detect any change in lattice constant with laser fluence in the films. The observed lattice constants of the films are presented in Table 5.1. All films possess a higher lattice constant compared to stoichiometric STO (3.905 Å). The ionic radius of La^{3+} (1.5 Å) with co-ordination number 12 is smaller than that of Sr^{2+} (1.58 Å) which it substitutes. Hence, a decrease in lattice constant should be expected in SLTO films and hence the observed increase in lattice constant indicates the presence of oxygen vacancies in the films. In STO, oxygen binds the cations together in SrO and TiO_2 planes and hence for films with oxygen vacancies, the cation-cation overlap decreases, leading to an increase in lattice constant [2, 11]. The systematic shift in (002) peak position indicates that the unit cell parameters of the films vary with laser fluence. The decrease in lattice constant with increase in laser fluence can be explained in terms of a decrease in oxygen vacancy concentration in the films. As the laser fluence increases, the oxygen content in the film increases. The plasma plume generated from the surface of the SLTO target has different ionic elements and clusters. The velocity of the plume species depends on different factors such as the mass, electrical charge of the species, laser fluence of the ablating laser, and partial pressure of the background gas [12]. Oxygen ions have the lowest mass compared to other species of the plume and possess a low magnitude (-2) of the electrical charge and hence have the highest velocities. Evidently oxygen ions reach the substrate first. At high laser fluence, more oxygen ions are bombarded towards the substrate where the nucleation takes place [12], enabling growth of films with lower oxygen vacancy concentration. From the FWHM of the (002) peaks of the films I, II and III an average crystallite size of 55 nm was calculated by applying Scherrer's equation after taking into account the instrument broadening. For film III, the fine scan reveals a broader shoulder (denoted by 'C'), which is indicative of a small cation non-stoichiometry [13]. However, from the shift of the (002) peak position, it is clear that oxygen vacancy concentration is highest in this film and hence the cation non-stoichiometry will have negligible influence in the transport properties of the films. On the contrary, if one assumes that the oxygen concentration in the films are the same, the deficiency of La^{3+}, that can also explain the observed shift in the peak position, should lead to a marked reduction in carrier concentration in the n-type SLTO films, since each La^{3+} ion contributes an electron to the conduction band and the deficiency of La^{3+} may be treated as hole doping. However, as shown in Table 5.1, the carrier concentrations of the films I, II and III are respectively 3.635, 8.312 and 11.27 ($\times 10^{20}$ cm^{-3}) implying that the film with largest shift in the (002) peak has the highest carrier concentration and hence La^{3+} deficiency can be ruled out. Moreover, if contribution from oxygen vacancies is ignored, using a simple calculation using the unit cell volume and assuming that all La atoms are ionized, with each La^{3+} ion contributing an electron to the conduction band, it can be shown that approximately 2.1, 4.9 and 6.7 at.% of La^{3+} is required to account for the observed carrier concentrations in films I, II and III respectively. Such large variations in La^{3+} concentration is not probable since the concentration of La^{3+} in the target is only 2 at.%. Also, such an increase in La^{3+} content should result in a decrease in lattice constant whereas the observed trend is the opposite. It must be noted that the observed carrier concentrations can be easily accounted for if we assume $Sr_{0.98}La_{0.02}TiO_{3-\delta}$ with δ= 0.0008, 0.015 and 0.024 respectively for films I, II and III respectively and these values of δ can be easily achieved in the PLD growth in 20 mTorr of Ar.

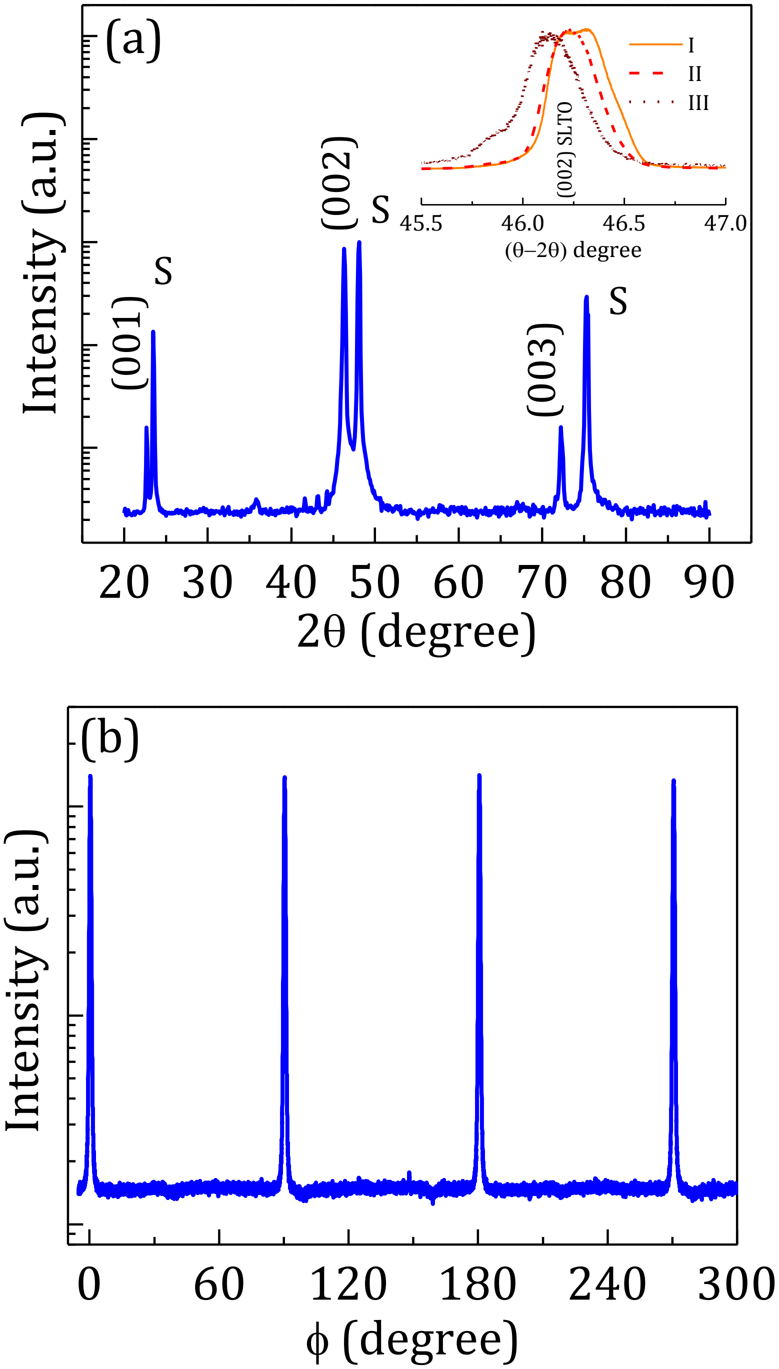

Figure 5.1. (a) θ-2θ XRD pattern for SLTO thin films grown by different laser fluences on LAO substrate. The inset shows the fine scan for (002) reflection revealing the lattice expansion with decrease in laser fluence. (b) Φ-scan for film II.

The Rutherford Backscattering Spectroscopic (RBS) spectrum of the as-grown SLTO film on Al_2O_3 substrate is shown in Figure 5.2 along with the simulated curve. The edges corresponding to the elements of the film are marked. Since the substrate is thick, signal from Al extends to lower energies and the oxygen peaks from the film as well as the substrate are superimposed on the Al plateau. The composition of the film is estimated to be 21.5% Sr, 0.5% La, 21.4% Ti, and 56.6% O. Since the La^{3+} ions substitute for the Sr^{2+} ions in SLTO films, the film is best represented as $Sr_{1.07}La_{0.025}Ti_{1.07}O_{3-\delta}$, δ being 0.17. The small deviation from target stoichiometry is evidently due to the presence of Ar gas during film growth, which can affect the growth process by introducing oxygen vacancies.

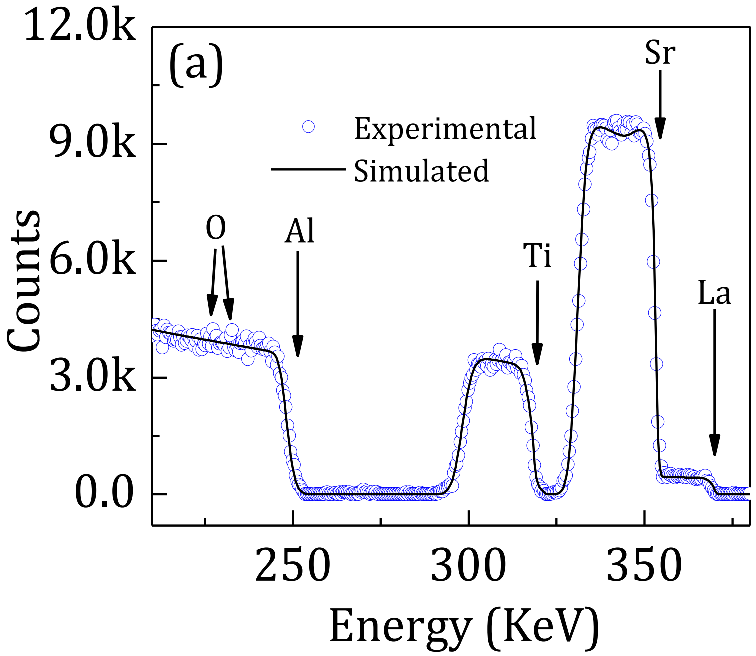

Figure 5.2. RBS spectra of the SLTO film. The symbols correspond to the experimental data, and the solid line to the simulated curve. The high energy edges corresponding to the constituent elements of the film are marked.

Figure 5.3(a-c) shows AFM height retrace images of the films. The dependence of rms roughness on the laser fluence is plotted in Figure 5.3(d). The roughness generally increases with increasing the laser energy [14]. Films I, II, and III have rms roughness 3.47 nm, 2.18 nm, and 1.55 nm respectively. Clearly, as the laser fluence increases, large ionic clusters will be ablated from the target. These bombarded constituents will not decompose completely before they arrive at the substrate surface because of their high velocity. At the same time, many incident atoms and ions will be re-sputtered from the substrate, which makes the surface rough during the nucleation process. The measured roughness values are approximately the same, and hence the difference in electron scattering in the films by surface roughness will be minimal.

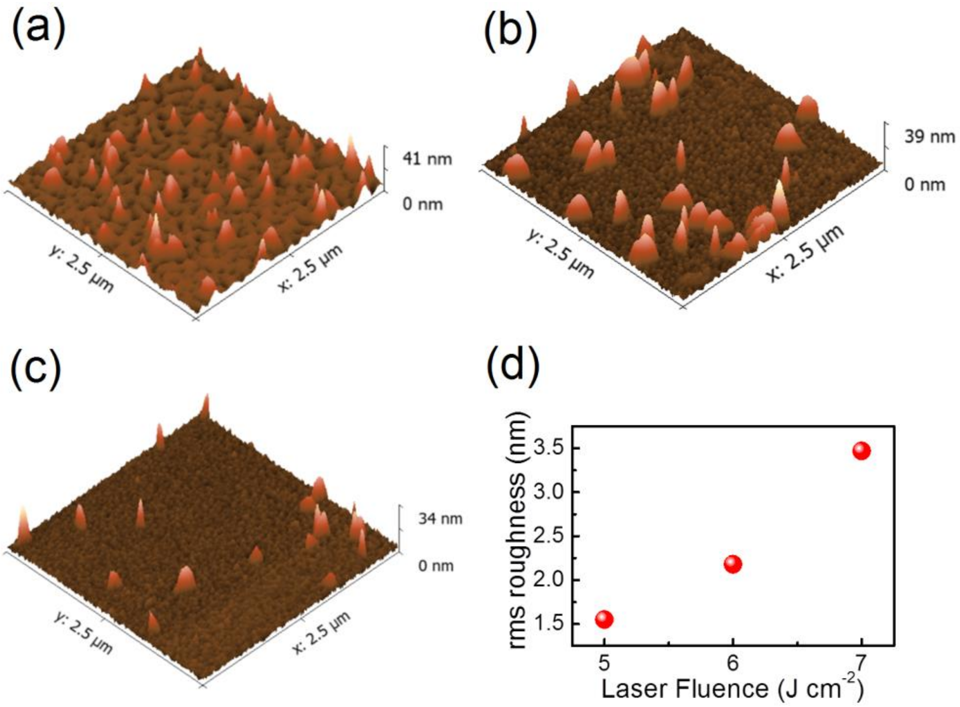

Figure 5.3. AFM height retrace images of (a) film I (b) film II and (c) film III together with the dependence of rms roughness of the films (d) as a function of laser fluence.

The temperature dependence of σ is plotted in Figure 5.4. All the films behave as degenerate semiconductors in the temperature range of 300–1000 K. The contribution of the LAO substrate to σ of SLTO is negligible because it is electrically insulating. At any temperature, film I has the highest σ due to lowest m^* of electrons as compared to the other films. In other words, m^*increases with lattice constant and n [3]. This is an obvious indication of the dependence of m^* of the electrons on laser fluence. In SLTO films, every La^{3+} ion that substitutes for Sr^{2+} ion contributes an electron each to the conduction band, provided all the dopant atoms are ionized. Similarly, each doubly ionized oxygen vacancy contributes two electrons to conduction. Hence n of SLTO increases. Table 5.1 shows the electrical transport properties at 300 K of the SLTO thin films grown with different laser fluences. The Hall mobility was estimated by using the equation $\sigma = ne\mu$ [15]. From Table 5.1, it is evident that film III with the highest concentration of oxygen vacancies has the highest n. However, since oxygen vacancies act as point scatterers, μ of film III is adversely affected, leading to a reduction in σ.

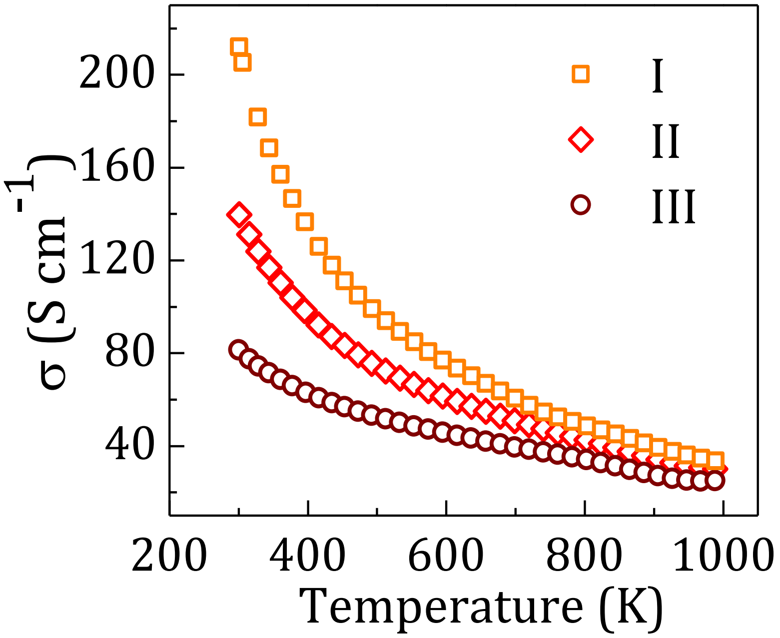

Figure 5.4. Electrical conductivity for the films grown with different laser fluences.

The temperature dependence of Seebeck coefficient and power factor ($PF = S^2\sigma T$), are shown in Figure 5.5(a) and (b) respectively. All films have negative Seebeck coefficient indicating n-type conduction as a consequence on La^{3+} and oxygen vacancies doping of STO. The effective masses of the electrons in the films were estimated from the Seebeck coefficient around the room temperature, using the following equation [15, 16]:

$$S = \frac{8\,\pi^{8/3}\,k_B^2\,m^*}{3^{5/3}\,e\,h^2\,n^{2/3}}\,(r+1)\,T\,, \tag{4.1}$$

where $k_B, m^*, h, n, r, and\ T$ are the Boltzmann's Constant, effective mass, Planck's constant, carrier concentration, carrier scattering parameter of the relaxation time, and absolute temperature, respectively.

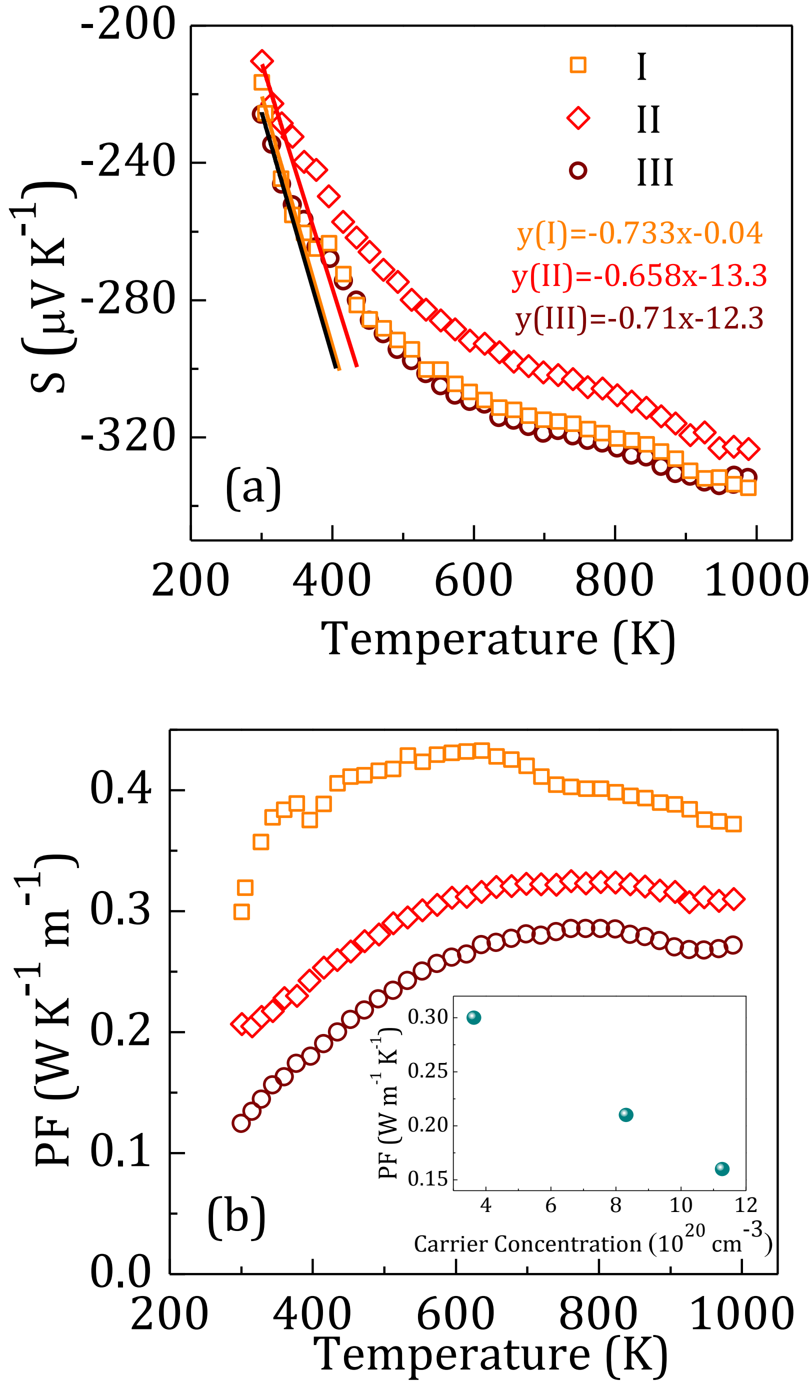

Figure 5.5. The temperature dependence of (a) Seebeck coefficient and (b) power factor (PF) for SLTO thin films grown by different laser fluences. The inset to (b) shows the power factor dependence on carrier concentration at 300 K.

From the slope of the S–T curve at temperatures below the Debye temperature [17] of the $SrTiO_3$ (θ_D=513 K), m^* of the films can be extracted by assuming r=2 (ionized impurity scattering). This assumption is valid near room temperature since scattering by acoustic phonons can be neglected below θ_D. Above θ_D, the slope of the S–T curve changes, and this is attributed to changes in electron scattering mechanism. Electrons are scattered predominantly by acoustic phonons above θ_D.

Table 5.1 Measured and calculated transport properties of SLTO films at 300 K. m^*/m_0 is the effective mass of the carriers with respect to the rest mass of electron (m_0)

Sample No.	Lattice constant (Å)	Electrical conductivity (S cm^{-1})	Carrier concentration (× 10^{20} cm^{-3})	Hall mobility (cm^2 V^{-1} s^{-1})	Effective mass m^*/m_o	Seebeck coefficient |S| (μV K^{-1})	Power factor (W K^{-1} m^{-1})
I	3.918	212	3.635	3.64	1.88	217	0.30
II	3.924	140	8.312	1.05	2.93	222	0.21
III	3.932	81	11.27	0.45	3.86	257	0.16

The temperature dependence of the derived PF (W K^{-1} m^{-1}) is plotted in Figure 5.5(b). Film I exhibits the best PF within the whole temperature range (0.433 W K^{-1} m^{-1}) at 636 K which compares well with those reported for 0 % La doped STO (0.23 W K^{-1} m^{-1}), 5 % La doped STO (0.93 W K^{-1} m^{-1}) [2] at 375 K, and 10 % Nb doped STO (0.6 W K^{-1} m^{-1}) [5] at 1000 K. Inset to Figure 5.5(b) shows the variation of PF with n for the SLTO films. It is seen that the film with the lowest n has the highest PF. Recently, it has been reported that oxygen vacancies in STO lead to a decrease in the thermal conductivity [18]. Hence, by tuning the oxygen vacancies, large increase in ZT may be achieved since oxygen vacancies, if controlled, can increase the electronic contribution with a simultaneous reduction in thermal conductivity.

5.5 Conclusions

In summary, we showed the effect of laser energy on the thermoelectric response of SLTO thin films in the temperature range 300–1000K. In PLD process, the coating of laser window by the ablated species, with sequential depositions is a source of uncertainty of actual laser energy falling on the target. For wide band-gap materials such as SLTO, this coating effect results in a significant drop of laser energy falling on the target, but often goes undetected to the bare eye. As demonstrated in this work, the variation in laser energy affects the dynamics of film growth. As the laser fluence increases, the oxygen concentration increases, resulting in a reduction in carrier concentration and electron effective mass which determines the thermoelectric power factor of the films. The best power factor obtained in this work is 0.433 W K^{-1} m^{-1} at 636 K for 7 J cm^{-2} $pulse^{-1}$ which agrees well with those reported in literature.

5.6 References

1. H. Ohta, S. Kim, Y. Mune, T. Mizoguchi, K. Nomura, S. Ohta, T. Nomura, Y. Nakanishi, Y. Ikuhara, M. Hirano, H. Hosono, and K. Koumoto,*"Giant thermoelectric Seebeck coefficient of a two-dimensional electron gas in* $SrTiO_3$*",* Nat Mater, 6, 129 (2007).
2. J. Ravichandran, W. Siemons, D.W. Oh, J.T. Kardel, A. Chari, H. Heijmerikx, M.L. Scullin, A. Majumdar, R. Ramesh, and D.G. Cahill,*"High-temperature thermoelectric response of double-doped* $SrTiO_3$ *epitaxial films",* Physical Review B, 82, 165126 (2010).
3. T. Okuda, K. Nakanishi, S. Miyasaka, and Y. Tokura,*"Large thermoelectric response of metallic perovskites:* $Sr_{1-x}La_xTiO_3$*",* Physical Review B, 63, 113104 (2001).
4. S. Ohta, T. Nomura, H. Ohta, and K. Koumoto,*"High-temperature carrier transport and thermoelectric properties of heavily La- or Nb-doped* $SrTiO_3$ *single crystals",* Journal of Applied Physics, 97, 034106 (2005).
5. S. Ohta, T. Nomura, H. Ohta, M. Hirano, H. Hosono, and K. Koumoto,*"Large thermoelectric performance of heavily Nb-doped* $SrTiO_3$ *epitaxial film at high temperature",* Applied Physics Letters, 87, 092108 (2005).
6. H. Ohta,*"Thermoelectrics based on strontium titanate",* Materials Today, 10, 44 (2007).
7. J. Liu, C.L. Wang, W.B. Su, H.C. Wang, P. Zheng, J.C. Li, J.L. Zhang, and L.M. Mei,*"Enhancement of thermoelectric efficiency in oxygen-deficient* $Sr_{1-x}La_xTiO_{3-\delta}$ *ceramics",* Applied Physics Letters, 95, 162110 (2009).
8. H.C. Wang, C.L. Wang, W.B. Su, J. Liu, Y. Zhao, H. Peng, J.L. Zhang, M.L. Zhao, J.C. Li, N. Yin, and L.M. Mei,*"Enhancement of thermoelectric figure of merit by doping Dy in* $La_{0.1}Sr_{0.9}TiO_3$ *ceramic",* Materials Research Bulletin, 45, 809 (2010).
9. S. Liang, D.J. Wang, J.R. Sun, and B.G. Shen,*"Effect of oxygen content on the transport properties of La-doped* $SrTiO_3$ *thin films",* Solid State Communications, 148, 386 (2008).
10. C.W. Schneider, M. Esposito, I. Marozau, K. Conder, M. Doebeli, Y. Hu, M. Mallepell, A. Wokaun, and T. Lippert,*"The origin of oxygen in oxide thin films: Role of the substrate",* Applied Physics Letters, 97, 192107 (2010).
11. W. Wunderlich, H. Ohta, and K. Koumoto,*"Enhanced effective mass in doped* $SrTiO_3$ *and related perovskites",* Physica B: Condensed Matter, 404, 2202 (2009).
12. C.W. Schneider and T. Lippert, *"Laser Processing of Materials"*, Springer Berlin Heidelberg, 89 (2010).
13. B. Jalan and S. Stemmer,*"Large Seebeck coefficients and thermoelectric power factor of La-doped* $SrTiO_3$ *thin films",* Applied Physics Letters, 97, 042106 (2010).

14. M. Liu, B. Man, X. Lin, and X. Li,*"The effect of incident laser energy on pulsed laser deposition of HgCdTe films",* Journal of Crystal Growth, 311, 1087 (2009).
15. R.A. Smith, *"Semiconductors"*. Cambridge University Press (1956).
16. B.M. Askerov, *"Electron Transport Phenomena in Semiconductors"*. World Scientific (1994).
17. M. Ahrens, R. Merkle, B. Rahmati, and J. Maier,*"Effective masses of electrons in n-type $SrTiO_3$ determined from low-temperature specific heat capacities",* Physica B: Condensed Matter, 393, 239 (2007).
18. C. Yu, M.L. Scullin, M. Huijben, R. Ramesh, and A. Majumdar,*"Thermal conductivity reduction in oxygen-deficient strontium titanates",* Applied Physics Letters, 92, 191911 (2008).

Chapter 6.

Doping site dependent thermoelectric properties of epitaxial strontium titanate thin films

(*J. Mat. Chem. C, 2, 9712 (2014)* - Reproduced by permission of The Royal Society of Chemistry)

6.1 Abstract

We demonstrate that the thermoelectric properties of epitaxial strontium titanate (STO) thin films can be improved by additional B-site doping of A-site doped ABO_3 type perovskite STO. The additional B-site doping of A-site doped STO results in increased electrical conductivity, but at the expense of Seebeck coefficient. However, doping on both sites of the STO lattice significantly reduces the lattice thermal conductivity of STO by adding more densely and strategically distributed phononic scattering centers that attack a wider phonon spectra. The additional B-site doping limits the trade-off relationship between electrical conductivity and total thermal conductivity of A-site doped STO, leading to an improvement in room-temperature thermoelectric figure of merit, ZT. The 5% Pr^{3+} and 20% Nb^{5+} double-doped STO film exhibits the best ZT of 0.016 at room temperature.

6.2 Introduction

Metal oxides have recently attracted significant attention for thermoelectric (TE) power generation at high temperatures due to their greater chemical and thermal stability over heavy metal alloys [1-3]. Furthermore, metal oxides are naturally abundant and non-toxic, unlike heavy metal alloys whose use is limited to specific applications such as in space exploration. Among metal oxides, crystalline $SrTiO_3$ (STO) is a promising TE material, which crystallizes in the cubic perovskite structure (lattice parameter a = 3.905 Å, space group $pm3m$). Electrical conductivity of STO can be easily varied from insulating to metallic by substitutional doping on different sites [4] (A-site and B-site) in the lattice or by creating oxygen vacancies [5]. Generally, the performance of TE materials is evaluated in terms of the dimensionless figure of merit ZT ($ZT = \sigma S^2 T/(\lambda_e + \lambda_l)$, where σ is the electrical conductivity, S is the Seebeck coefficient, T is the absolute temperature, and λ_l and λ_e are the lattice and electronic contributions to thermal conductivity, respectively). STO has relatively low ZT compared to the conventional TE materials (ZT >2) [6, 7], which is mainly attributed to its high thermal conductivity (~7 W m^{-1} K^{-1} for reduced bulk STO [8] and ~10 W m^{-1} K^{-1} for bulk La^{3+} doped STO [4]). These high thermal conductivity values of STO are predominantly attributed to λ_l, nearly one order of magnitude higher than that of conventional TE materials, since the perovskite structure of STO is relatively simple and lacks effective phononic scattering centers [3]. Nevertheless, STO has a high power factor ($PF = \sigma S^2 T$) comparable to the best TE materials. Considerable improvement in ZT is required to make STO a practical TE material and one way to do so is to reduce the thermal conductivity by introducing nano-structures, such as superlattices [9, 10], nano-cubes [11], and nano-inclusions [12]. Another approach is to create point defects such as oxygen vacancies [13] and extrinsic doping of elements that enhance mass-fluctuation scattering [14-17]. Extrinsic dopants, of different mass and ionic radius compared to Sr and Ti, that occupy A and B sites can be effectively used for scattering phonons. In singly doped STO, either Sr (A-site) or Ti (B-site) gets substituted with elements such as La, Y, Pr etc. or Nb, Ta etc. respectively that help in reducing λ_l [15]. Maximum enhancement in phonon scattering is possible with high density and strategic distribution of these dopants. Doping on both A and B- sites is hence a promising approach to reduce λ_l and optimize ZT, which needs to be investigated.

In this work, we report the role of additional B-site doping in enhancing the TE properties of A-site doped epitaxial STO films. Additional doping on B-site improves the TE power factor by increasing σ through adding electrons to the conduction band with lower effective mass [18]. We also report the role of double-doping on both sites (A-site and B-site) in reducing λ_l of STO films, and hence improving the room-temperature ZT. In order to correlate the TE properties with the structure and morphology of the films, x-ray diffraction (XRD) and high resolution scanning electron microscopy (SEM) studies have been carried out. A notable dependence of structure and morphology on doping site in STO films is observed. The temperature dependence of σ and S has been analyzed for the films. The observed results are explained based on the improved room-temperature ZT brought in by a simultaneous enhancement of PF, by tuning the carrier density, and reduction of λ_l

of the films by adding efficient phononic scattering centers distributed effectively via double-doping route.

6.3 Experimental Section

All films were deposited by pulsed laser deposition (PLD) system (Neocera, Beltsville, MD) using a KrF excimer laser (λ=248 nm, pulse duration ~20 ns, repetition rate =10 Hz). $Sr_{0.95}Pr_{0.05}TiO_{3-\delta}$ (SPTO) and $Sr_{0.98}La_{0.02}TiO_{3-\delta}$ (SLTO) films were deposited by ablation of $Sr_{0.95}Pr_{0.05}TiO_3$ and $Sr_{0.98}La_{0.02}TiO_3$ targets, while $Sr_{0.98}La_{0.02}Ti_{0.8}Nb_{0.2}O_{3-\delta}$ (SLTNO) and $Sr_{0.95}Pr_{0.05}Ti_{0.8}Nb_{0.2}O_{3-\delta}$ (SPTNO) films were deposited by ablation of the double-doped $Sr_{0.98}La_{0.02}Ti_{0.8}Nb_{0.2}O_3$ and $Sr_{0.95}Pr_{0.05}Ti_{0.8}Nb_{0.2}O_3$ targets at a laser fluence of 4 J cm^{-2} $pulse^{-1}$. The targets were held on a rotating carousel to ensure uniform ablation. In order to create sufficient oxygen vacancies, 20 mTorr of Ar was introduced as a reducing gas, using a mass flow controller. Films were deposited on (001) oriented $LaAlO_3$ (LAO) substrates (MaTeck GmbH, Germany) of dimensions 10x10x0.5 mm^3 with a_{LAO}= 3.82 Å, held at a temperature of 973 K. The thickness of the films was around 270 nm as measured by a spectroscopic ellipsometer. The phase purity of the films was determined from the analysis of θ-2θ scan using an x-ray diffractometer (Bruker D8 Discover, AXS System, Germany). Φ scan was done for asymmetric (110) diffraction of the films on LAO substrate. When ψ, the tilt angle of the surface normal of the film, was 45˚ and 2θ was fixed at 32.42˚, Φ scan result was obtained by rotating the film (0˚–360˚) around the surface normal. In-plane σ and S were measured, quasi-simultaneously on the same sample, in the range 300–1000 K by using respectively the linear four-probe and the differential methods, under Ar/H_2 (96% Ar and 4% H_2) ambient using a commercial setup (RZ2001i, Ozawa Science Co Ltd., Nagoya, Japan). At any temperature, σ was measured first, followed by S by introducing a ΔT of ~4–10 K, between the voltage probes. The measurements of σ and S were then repeated at a higher sample temperature. We used the 3ω method [19] to measure the cross-plane thermal conductivity of the films. In this method, an alternating current passes through a metal line patterned on the film, and the amplitudes of the first and third harmonic voltage drops along the line are measured in order to extract the thermal conductivity of the films. For the metal line which acts as both a heater and a thermometer, a 200 nm thick Au film, with 20 nm thick Cr as an adhesive layer, were deposited on the films using sputtering. The Au films were patterned to linear heaters using photolithography and lift-off. The width (~10 μm) of Au heaters is much larger than the film thickness (~500 nm) which allows us to measure the cross-plane thermal conductivity by applying one dimensional heat flow model. In order to pattern the metal line on the electrically conductive STO films, an insulating layer is needed to prevent any leakage current. Therefore, an insulating layer of SiN_x (thickness of 100 nm) was deposited on doped STO films and bare Si substrate using sputtering, and we measured the temperature rise from both samples. An algorithm was used to extract the temperature drops across the doped STO films from the rise in temperature across the two samples, using a comparative method [20]. Room temperature Hall effect measurements were carried out using a physical property measurement system (PPMS) (Quantum Design, Inc., USA). Surface morphology and microstructures were observed by a SEM system (FEI Nova NanoSEM, USA).

6.4 Results and Discussion

Figure 6.1(a) shows θ-2θ XRD patterns for the films. The out-of-plane diffraction peaks of the {001} planes from LAO (marked '*') and films can be seen, while reflections from other crystalline orientations are of negligible intensity, indicating a preferential epitaxial growth of the films on the substrate. To verify the in-plane epitaxial relationship between the films and LAO substrate, Φ scans were obtained. Figure 6.1(b) shows typical Φ-scan XRD patterns for the off-axis {011} reflections from the films and substrate. Four peaks with almost equal intensity spaced by 90° can be observed for both substrate and films indicating that the films and the substrate have four-fold symmetry about an axis normal to the substrate. The peak positions of the Φ-scan patterns corresponding to films and substrate indicate that the films are in-plane textured and epitaxially aligned on the substrate with epitaxial relationships of [100] STO || [100] LAO and [001] STO || [001] LAO. High-resolution XRD scans in the θ-2θ geometry were done for (002) reflection from all films (Figure 6.1(c)) to detect any change in lattice constant depending on the extrinsic dopants in the films. The observed lattice constants of the films are plotted in Figure 6.1(d). All films possess higher lattice constants compared to stoichiometric STO (3.905 Å) although the ionic radii [21, 22] of Pr^{3+} (1.144 Å) and La^{3+} (1.36 Å) are smaller than that of Sr^{2+} (1.44 Å) which they substitute. The observed increase in lattice constant is hence attributed to the presence of oxygen vacancies in the films. It has been reported that doped STO films grown under identical conditions are oxygen deficient [18]. In STO, oxygen binds the cations together in SrO and TiO_2 planes and hence for films with oxygen vacancies, the cation-cation overlap decreases, leading to an increase in lattice constant [23]. Furthermore, it may be noted that oxygen vacancy creation induces the formation of Ti^{3+} (0.67 Å) from Ti^{4+} (0.605 Å), adding to the increase in lattice constant [24]. On the other hand, SLTNO and SPTNO films have higher lattice constant than stoichiometric STO which is attributed to both oxygen vacancies and the difference in the ionic radii [22] of Nb^{5+} (0.640 Å) compared to Ti^{4+} (0.605 Å) which it substitutes [25].

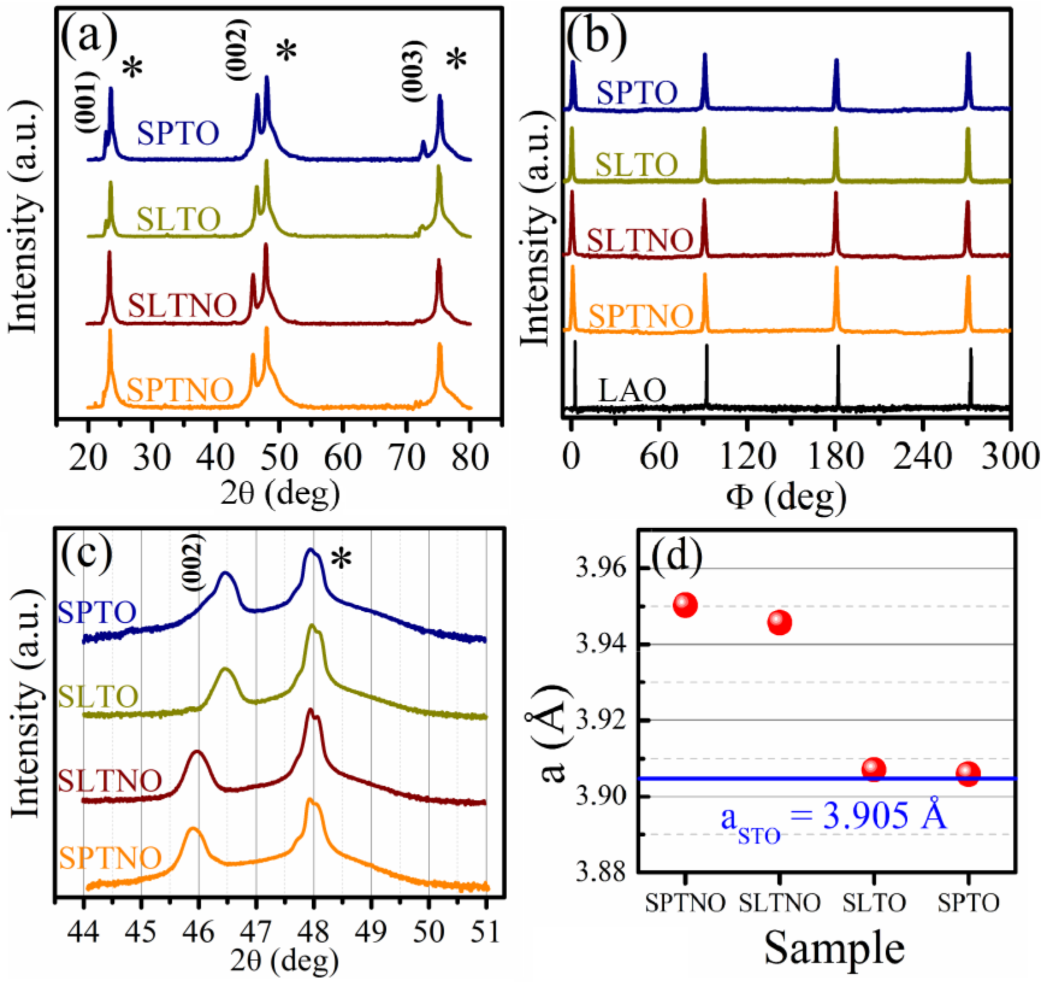

Figure 6.1. (a) θ-2θ XRD patterns for doped STO thin films grown on LAO substrate. Peaks of (001) reflections are seen along with substrate peaks (*) indicating the preferential epitaxial growth of the films on the substrates, (b) Φ scan for {011} planes of the films and the substrate, showing four evenly spaced (90^0) peaks that confirm a four-fold symmetry about an axis normal to the substrate, (c) high resolution scan for (002) reflection revealing a shift in (002) peak position, depending on the dopants, and (d) dependence of lattice constant on the dopant concentration.

High resolution SEM images reveal the surface morphology of the films (Figure 6.2). It is evident that the surface morphology of A-site doped films (Figure 6.2(a) and (b)) is quite different from that of films with additional B-site doping (Figure 6.2(c) and (d)). For instance, the morphology of SLTO film (Figure 6.2(a)) consists of the highest density of randomly distributed nano-features (~50–90 nm) on the surface whereas SPTO film (Figure 6.2(b)) has lower density of such nano-features. On the other hand, SLTNO and SPTNO films (Figure 6.2(c) and (d), respectively) have densely arranged grains with less grain size distribution (~40 nm) than the A-site doped films. Although SLTNO and SPTNO films have lower grain sizes, which may reduce the mobility (μ) of free electrons as a result of scattering at grain boundaries, they exhibit higher σ (as explained later) than SLTO and SPTO films indicating that the scattering of free electrons is not dominated by grain boundaries.

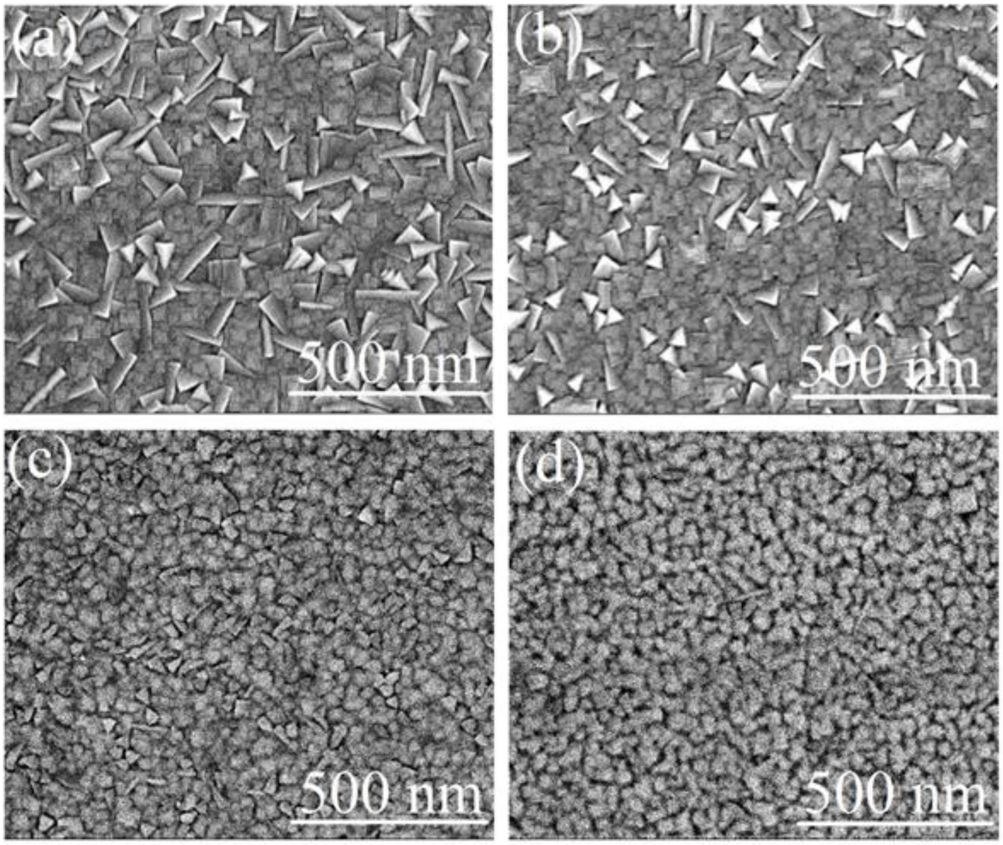

Figure 6.2. Topographic SEM images showing the microstructures of (a) SLTO, (b) SPTO, (c) SLTNO, and (d) SPTNO films.

Figure 6.3(a) and (b) show schematic representations of perovskite lattice for SLTO and SPTO films where La^{3+} and Pr^{3+} substitute Sr^{2+} ions, respectively. ln (σ)-$1/T$ relationship of SLTO and SPTO films is plotted in Figure 6.3(c). Since LAO substrate remains insulating (as measured from the rear side), even after deposition of the films, its contribution to σ of the films can be neglected. Both films show a typical degenerate semiconductor behavior. The possible sources of free electrons in the films are the substitutional dopants (La^{3+} and Pr^{3+}) and the oxygen vacancies (δ). At any temperature, SPTO film has higher σ than SLTO due to the higher carrier concentration (n) (Table 6.1). At T ~600 and 750 K, the slopes of ln (σ)-$1/T$ plots change for SLTO and SPTO films, respectively, which is likely due to changes in the scattering mechanism around these temperatures [4]. At $T < 600$ K, free electrons are believed to be predominantly scattered by ionized impurities embedded in the STO lattice, as previously reported [26]. The scattering centers are the randomly distributed oxygen vacancies [13] (usually doubly ionized) [5] and the ionized dopants that substitute at the A-sites [14]. For doped STO films with lower ionized impurity and hence carrier densities, polar optical phonon scattering has also been reported as an important mechanism that limits carrier mobility around 300 K [4, 27]. However, in our films, which have high ionized dopant and carrier densities, the scattering at 300 K is most likely due to ionized impurities, with possible contribution also from polarons. It is interesting to note that in many wide band-gap degenerate oxides, scattering by ionized impurities has been reported as the dominant scattering mechanism at room temperature [28, 29]. As temperature increases, scattering by lattice vibrations increases and start to dominate around 600 and 750 K for SLTO and

SPTO films, respectively, leading to a change in the slope of the ln (σ)-1/T plots. At T ~750 and 900 K, σ of SLTO and SPTO films, respectively, starts to increase with T as the lightly reduced regions can be reduced more at these temperatures, because the measurements are done in the highly reducing Ar/H_2 ambient. It may be noted that similar changes in curvatures are noticed for the temperature variation of S of the films (to be discussed later), confirming the changes in scattering mechanisms.

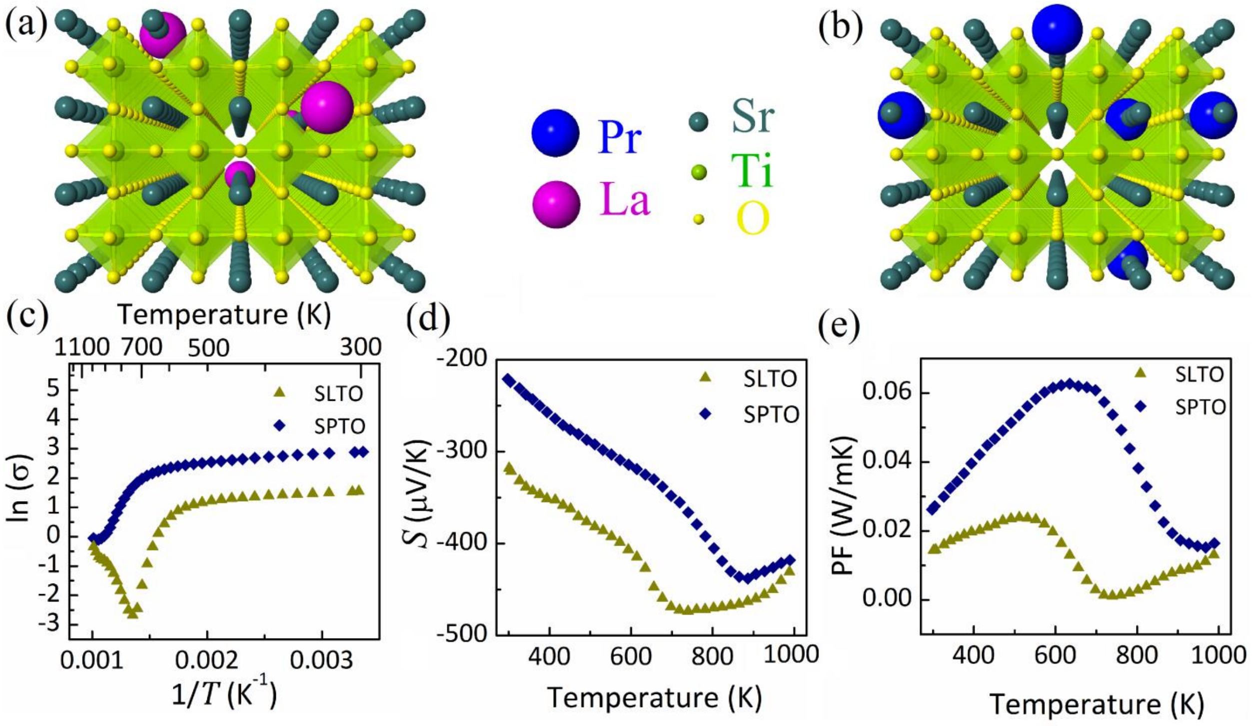

Figure 6.3. Schematic representations showing substitutional doping of La^{3+} and Pr^{3+} for Sr^{2+} (A-site) in (a) SLTO and (b) SPTO films. (c) ln ($\boldsymbol{\sigma}$) vs $\mathbf{1/}\boldsymbol{T}$ plot, and the temperature dependence of (d) Seebeck coefficient and (e) power factor of SLTO and SPTO films.

The temperature dependence of S and PF of SLTO and SPTO films are shown in Figure 6.3(d) and (e), respectively. Both films have negative S indicating n-type conduction as a consequence of Pr^{3+}, La^{3+} and oxygen vacancy doping of STO. Both films also exhibit a typical degenerate semiconducting behavior with a linear dependence of S on temperature up to ~600 K and ~750 K for SLTO and SPTO films, respectively. Above these temperatures, this linearity is no longer obeyed. This deviation from linearity can be attributed to the change in the scattering mechanism of the free electrons as discussed earlier, since we observe similar changes in S-T curves as in ln (σ)-1/T [4]. The effective masses of the electrons in the films were estimated from the linear S-T relationship around room temperature (Table 6.1), using the following equation described by the degenerate Fermi gas model [30, 31]:

$$S = C_n n^{-2/3} m^*(r+1)T\ , \tag{6.1}$$

where the constant C_n includes only the basic physical constants, $C_n = 8\,\pi^{8/3}\,k_B^2\,/\,(3^{5/3}\,e\,h^2)$; k_B is the Boltzmann's Constant; h is the Planck's constant; e is the electronic charge; r is the carrier scattering parameter of the relaxation time. From the slope of the S-T curve at around 300 K, m^* of the films can be extracted by taking r=2, assuming ionized impurity scattering for these films, as discussed earlier. It may be noted here that, scattering from grain boundaries can be ignored at room temperature since the mean free path [32] ($l = (3\pi^2)^{1/3}\,(h/2\pi)(\sigma/e^2 n^{2/3})$) of electrons ($l$<0.7 nm), considering degenerate conduction, are much smaller than the grain sizes (~40–90 nm) of the films suggesting that most scattering mechanisms take place in the in-grain domain. As evident from Table 6.1, m^* in A-site doped STO films (SLTO and SPTO) increases with n as previously reported [33].

In Figure 6.3(d), S tends to saturate to asymptotic values at T ~700 and 850 K, for SLTO and SPTO films, respectively. Such a non-monotonic change of S-T curve at high temperature is usually explained by Heikes theory [34]. It has been reported [35, 36] that the temperature at which S saturates increases with dopant concentration, which is indeed observed for our films. However, S of SLTO and SPTO films deviates above T ~750 K and ~900 K respectively, from the saturation value, and hence Heikes theory cannot be used to interpret such a temperature dependence of S. One possible reason why Heikes theory cannot account for the observed variation of S at high temperatures is the presence of randomly distributed oxygen vacancy clusters [13], which is a common to STO films grown by PLD [37]. These clusters are in different degrees of reduction [5], and the lightly reduced regions can be reduced more at very high temperatures during measurements in a reducing ambient (Ar/H_2 in the present case), leading to a slight decrease in the absolute value of Seebeck coefficient ($|S|$) as observed in Figure 6.3(d). The increase in σ (Figure 6.3(c)) of these films above ~750 K and ~900 K respectively, confirms the reduction of lightly reduced regions in the films. Although SLTO and SPTO films have relatively high $|S|$, their σ is low resulting in poor PF values as shown in Figure 6.3(e). One way to improve PF is to increase the dopant concentration in STO, and it would be reasonable if this additional doping is applied to a different site in STO lattice, such as B-site, which can help reducing λ_l by increasing the density and randomness of the phononic scattering centers in the lattice.

The dependence of S on $T$and n can be understood from the fundamental theoretical treatment of transport in degenerate semiconductors. For a single band degenerate system, the Seebeck coefficient may be expressed as [38]:

$$S_i = \frac{\int g_i(E)E(E-E_F)\frac{\partial f_0}{\partial E}dE}{eT\int g_i(E)E\frac{\partial f_0}{\partial E}dE}, \tag{6.2}$$

where $g_i(E)$, E_F, f_0, and T are the electronic density of states (DOS), Fermi energy, Fermi distribution, and the absolute temperature, respectively. For multiband systems, the total Seebeck coefficient is given by

$$S = \frac{\sum_i S_i \sigma_i}{\sum_i \sigma_i}, \tag{6.3}$$

where σ_i is the conductivity due to the i^{th} band and the summation runs over all the bands.

It is clear from Equation 4.2 that S depends on the product of $g_i(E)$ and $\frac{\partial f_0}{\partial E}$ which brings in an asymmetry of DOS around E_F. The broadening or shifting of the function, $\frac{\partial f_0}{\partial E}$ brought in respectively by changes in T or n leads to marked observed variation in S, as illustrated in Figure 6.4(a) and (b). For instance, for a degenerate system with fixed n, with increase in T the asymmetry increases (Figure 6.4(a)), leading to an enhanced $|S|$, which explains the temperature variation of S of our films. Similarly, at any given T, the asymmetry is more pronounced for systems with lower n (Figure 6.4(b)). Hence, S follows an inverse relation with n, which again is observed in our films (Table 6.1).

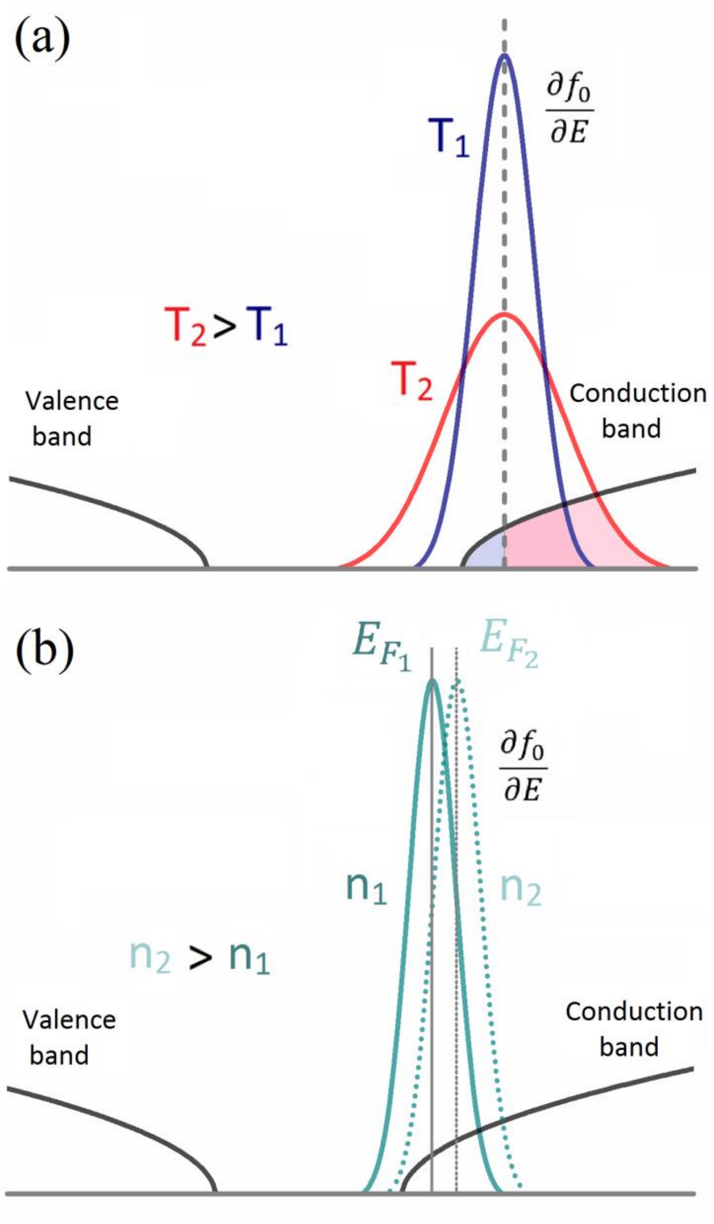

Figure 6.4. Schematic diagram representing asymmetry in density of states due to (a) broadening of the Fermi distribution function with increase in temperature and (b) shifting of the Fermi level ($\boldsymbol{E_F}$) due to increase in carrier density. The asymmetry of the area, described by the product $\boldsymbol{g_i(E)}\ \frac{\boldsymbol{\partial f_0}}{\boldsymbol{\partial E}}$, above and below $\boldsymbol{E_F}$ is marked by the shaded regions in (a). For a fixed carrier density, with increase in temperature, due to broadening of the Fermi function, the asymmetry with respect to $\boldsymbol{E_F}$ increases, leading to increase in absolute Seebeck coefficient. When carrier density increases, due to shift of $\boldsymbol{E_F}$ further into the conduction band, as shown in (b), the asymmetry decreases, leading to a decrease in absolute Seebeck coefficient.

Table 6.1. Lattice constant along with measured and calculated transport properties of the films at room temperature.

Sample	**A** (**Å**)	**σ** (**S cm^{-1}**)	**$\|S\|$** (**μV K^{-1}**)	**n** (**× 10^{21} cm^{-3}**)	**m^*/m_o**	**μ** (**cm^2 V^{-1} s^{-1}**)	**τ_e** (**fs**)	**λ_t** (**W m^{-1} K^{-1}**)	**λ_e** (**Wm^{-1} K^{-1}**)	**λ_l** (**Wm^{-1} K^{-1}**)	**ZT**
SLTO	3.907	5	318	0.79	1.9	0.04	0.04	3.77	0.005	3.76	0.004
SPTO	3.906	18	221	1.03	2.0	0.11	0.13	3.28	0.01	3.26	0.008
SLTNO	3.946	815	48	3.93	1.6	1.30	1.18	3.42	0.6	2.82	0.014
SPTNO	3.950	1420	44	4.51	1.4	1.97	1.57	3.75	1.04	2.71	0.016

To study the effect of additional B-site doping to the already A-site doped STO films (i.e. SLTO and SPTO), Nb^{5+} ions are chosen to be the substitutional dopants to Ti^{4+} ions (B-site) as shown in the schematic representations in Figure 6.5(a)and (b) for SLTNO and SPTNO films, respectively. ln (σ) of SLTNO and SPTNO films as function of $1/T$ is shown in Figure 6.5(c). A change in the slopes of ln (σ) vs $1/T$ plots is seen at T $\sim$750 K, indicating a change in scattering mechanisms of free electrons at this temperature as discussed earlier. σ of the double-doped films is enhanced compared to single-doped films as a consequence of the introduction of more free electrons to the conduction band by the additional B-site dopants to the already A-site doped STO. For instance, SPTNO film has σ two orders of magnitude higher than that of SPTO film. It is obvious that, at any T, SPTNO film possesses higher σ than SLTNO due to higher n (Table 6.1). The improvement in σ brought in by the additional B-site doping is opposed by a decrease in $|S|$ (Figure 6.5(d)), as $|S|$ decreases with n in degenerately doped semiconductors, as explained before. It is worthy to note that the saturation behavior of S observed for A-site doped films is not seen for SPTNO and SLTNO films, most probably due to the much higher dopant concentration in these films.

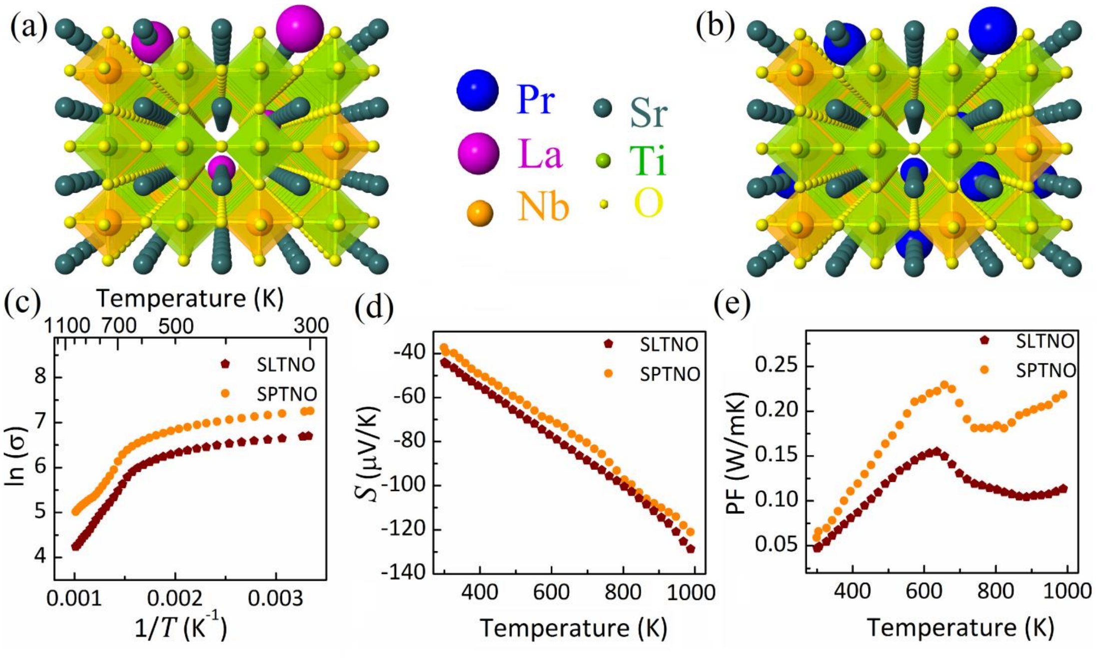

Figure 6.5. Schematic representations showing substitutional doping of Nb^{5+} for Ti^{4+} (B-site) in (a) SLTNO and (b) SPTNO films. (c) ln ($\boldsymbol{\sigma}$) vs $\mathbf{1/}\boldsymbol{T}$ plot, and the temperature dependence of (d) Seebeck coefficient and (e) power factor of SLTNO and SPTNO films.

Unlike A-site doped STO films, m^* of double-doped STO films (SLTNO and SPTNO) decreases with n (Table 6.1). To understand this discrepancy, it is important to consider the role of lattice constant in determining m^*. In STO films, the bottom of conduction band is mainly composed of Ti 3d orbitals [39] and an increase in lattice constant enhances orbital overlapping between adjacent Ti ions. It was predicted [23] that Nb doping of STO increases the lattice constant and induces a tetragonal distortion of the Ti sublattice, changing the degeneracy of the conduction band from 6-fold to 4-fold one, resulting in a higher band curvature and hence, a lower m^*, as observed for SLTNO and SPTNO films. For SLTO and SPTO films, where the lattice constant is close to the stoichiometric STO (3.905 Å), the tetragonal distortion can be neglected and m^* increases with n as previously reported [33]. As evident from Table 6.1, single-doped films possess lower μ than double-doped films which is attributed to the difference in m^*, i.e. the higher m^*, the lower μ. From m^* and μ values, the relaxation time (τ_e) can be found by using equation: $\tau_e = \mu m^*/e$. A quick perusal of the table reveals that σ increases with τ_e.

One possible reason for the large S of STO, and hence high PF, is the nature of the d-band which makes the m^* relatively large compared to other TE materials [3]. The temperature dependence of PF for SLTNO and SPTNO films is plotted in Figure 6.5(e). The double-doped films exhibit PF higher than single-doped films. SPTNO film exhibits the best PF (0.23 W K^{-1} m^{-1}) within the whole temperature range at 656 K, although it has a low S. The improvement in PF is attributed to the superior σ of SPTNO film brought in by the additional B-site doping.

The cross-plane thermal conductivity (λ_t, where $\lambda_t = \lambda_e + \lambda_l$) of the films was measured at room temperature (Table 6.1). We assume that the in-plane thermal conductivity is the same as the cross-plane one since the films are cubic and the properties are isotropic. All films have lower λ_t than stoichiometric bulk STO (11 W m^{-1} K^{-1}) [13] and La doped bulk STO (9 W m^{-1} K^{-1}) [33]. This reduction in λ_t can be attributed to the phonon scattering due to the randomly distributed nature of oxygen vacancy clusters [13] as well as phonon scattering from point defects caused by the extrinsic dopants (Figure 6.6(a)) [16, 40]. Maximum reduction in λ_l is attributed to oxygen vacancy clusters, whose feature size compares well with the phonon mean free path (order of nm) [13]. Nevertheless, it can be shown that extrinsic dopants are responsible for the change in λ_l of the films. If we assume that all extrinsic dopants are fully ionized, each one of them will donate one electron to the conduction band. By knowing the unit cell volume of STO ([3.905 Å]^3), it can be shown that the carrier concentration, donated only by extrinsic dopants, of SLTO, SPTO, SLTNO, and SPTNO films are 0.34, 0.84, 3.7, and 4.2×10^{21} cm^{-3}, respectively, which are lower than the measured ones (see Table 6.1). This difference in carrier concentrations, between measured and calculated ones, is attributed to the presence of oxygen vacancies in our films as each oxygen vacancy can donate two electrons to the conduction band. If the electron doping via oxygen vacancies is considered, it is possible to find that the concentrations (δ) of oxygen vacancies in SLTO, SPTO, SLTNO, and SPTNO films are 0.013, 0.006, 0.007, and 0.009, respectively. To understand the real effect of such change in concentrations of imperfections on the lattice thermal conductivity, one may calculate the relaxation time (τ) of phonon scattering from different imperfections in the lattice using the equation [41]:

$$\tau = \frac{1}{\varphi \eta \upsilon}, \tag{4}$$

where φ, η, and υ are respectively the phonon scattering cross section ($\varphi \propto$ (imperfection radius)^2), the number of scattering sites per unit volume, and the speed of sound. The calculated τ_i values due to different imperfections are listed in Table 6.2. It can be shown that the effective relaxation time (τ_{eff}) is lower than the lowest relaxation time due to individual scattering events, by using Matthiessen's rule ($\frac{1}{\tau_{eff}} = \sum_i \frac{1}{\tau_i}$), since the individual scattering events under consideration are all elastic in nature and the orders of magnitude of the individual relaxation times (τ_i) match, as evident from Table 6.2. The τ_i values of La^{3+} and Pr^{3+} are lower than those of oxygen vacancies, indicating that phonon scattering from extrinsic dopants is more effective than scattering from oxygen vacancies due to the difference in their relative concentrations.

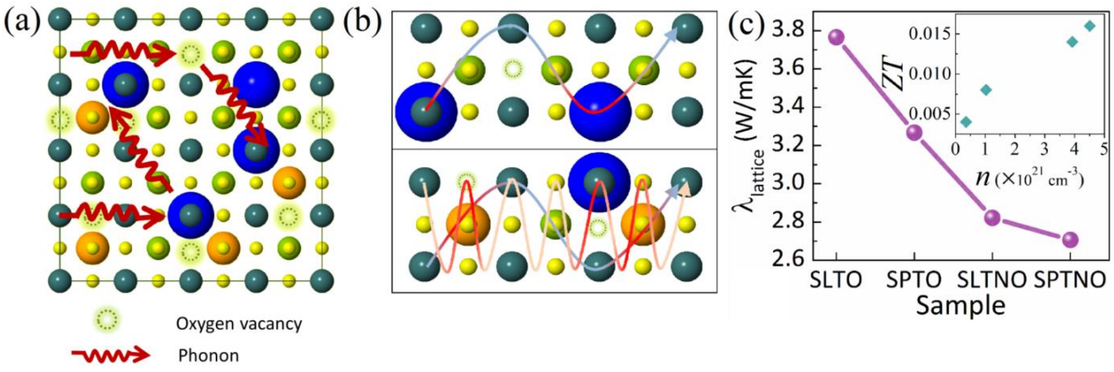

Figure 6.6. (a) Schematic diagram illustrating possible phonon scattering events with lattice defects resulting from extrinsic dopant ions and oxygen vacancies in the films, (b) schematic representation depicting possible scattering of wider phonon frequencies due to extrinsic doping at both A and B sites as compared to A-site doping alone. Assuming that A-site dopants can scatter phonons of frequency f, simultaneous doping at both A and B sites can scatter phonons of frequencies f, 2f and 3f, making it a more effective approach in reducing lattice thermal conductivity. (c) Direct dependence of lattice thermal conductivity on the site dependence of the extrinsic dopant concentrations which are 2%, 5%, 22%, and 25% for SLTO, SPTO, SLTNO, and SPTNO films, respectively. Inset to (b) shows *ZT* dependence on carrier concentration, at room temperature.

It has been reported [42] that λ_l is dominant in heavily doped STO systems (20% Nb or 20% Pr doped STO). It is very important to understand the significance of doping STO on different lattice sites in reducing λ_l. Figure 6.6(b) shows a schematic representation depicting how double-doping helps scatter wider phonon spectra as compared to single-doping. The phonon mean free path is usually of the order of nm in STO based films [13] and hence strategic positioning, density and distribution of efficient phononic scattering centers in the lattice bring in additional reduction of λ_l.

Figure 6.6(c) shows the direct dependence of λ_l on extrinsic dopant concentration and positioning of the scatterers. For instance, SPTNO film has the highest concentration of the largest phonon scattering centers distributed across two different sites (5% Pr^{3+} and 20% Nb^{5+} ions), and hence, it has the lowest λ_l (2.71 W m^{-1} K^{-1}) compared to other films. On the other hand, SLTNO film has slightly higher λ_l (2.82 W m^{-1} K^{-1}) than SPTNO film and this is attributed to the smaller mass and the lower concentration of La^{3+} ions than Pr^{3+} ions. On the other hand, single-doped (SLTO and SPTO) films have the highest λ_l (3.76 W m^{-1} K^{-1} and 3.26 W m^{-1} K^{-1}, respectively) due to the lowest concentration of point defects in the lattice compared to double-doped films. λ_e was calculated by using Wiedemann-Franz law ($\lambda_e = L\sigma T$, where L is the Lorentz number which is taken as [43] 2.45×10^{-8} W Ω K^{-2}). It is observed that λ_e does not become negligible when n exceeds 3×10^{21} cm^{-3} (Table 6.1) [44]. For instance, λ_e/λ_t of SPTNO (n = 4.51×10^{21} cm^{-3}) and SLTO (n = 0.79×10^{21} cm^{-3}) films is 0.28 and 0.001, respectively. The room-temperature ZT is plotted as a function of n in the inset to Figure 6.6(c). The ZT value increases with n as a result of the superior enhancement of σ over the small increase in λ_t of the double-doped STO films (SPTNO and SLTNO). It is clear that the approach of reducing λ_l via additional B-site doping in A-site doped STO films allows one to limit the trade-off relationship between σ and λ_t, and hence improving ZT. SPTNO film possesses the best ZT of 0.016 at room temperature compared to other films. This ZT value compares well with those reported at room temperature for 10% La doped bulk STO (0.015) [45], 5% La and 3% Nb double-doped bulk STO (0.025) [46], and 18% La and 2% Yb double-doped bulk STO (0.02) [15].

Table 6.2. Relaxation rime due to Phonon scattering from different imperfections in the films.

Imperfection	τ_i (×10^{-7} s)
2% La^{3+}	1.45
5% Pr^{3+}	1.35
20% Nb^{5+}	8.9
1.3% Oxygen Vacancy (SLTO)	1.96
0.6% Oxygen Vacancy (SPTO)	4.25
0.7% Oxygen Vacancy (SLTNO)	3.64
0.9% Oxygen Vacancy (SPTNO)	2.83

6.5 Conclusions

We show the direct dependence of thermoelectric properties of STO films on additional B-site doping on A-site doped STO. Additional B-site doping plays a significant role in enhancing the thermoelectric power factor and reducing the lattice thermal condcutivty of A-site doped STO, and hence improving their room-temperature ZT. Our approach of reducing the lattice thermal conductivity by adding more phononic scattering centers that are strategically distributed, via additional B-site doping of A-site doped STO films, allows us to limit the trade-off relationship between the electrical conductivity and the total thermal conductivity, leading to an improvement in ZT. The 5% Pr^{3+} and 20% Nb^{5+} double-doped (SPTNO) film exhibits the best ZT of 0.016 at room temperature which compares well with those reported for STO based thermoelectrics at room temperature. The critical dependence of thermoelectric properties on double-doping approach can offer a pathway for the design of thin film thermoelectric devices using optimized STO films.

6.6 References

1. J.W. Fergus,*"Oxide materials for high temperature thermoelectric energy conversion",* Journal of the European Ceramic Society, 32, 525 (2012).
2. J. He, Y. Liu, and R. Funahashi,*"Oxide thermoelectrics: The challenges, progress, and outlook",* Journal of Materials Research, 26, 1762 (2011).
3. K. Koumoto, Y. Wang, R. Zhang, A. Kosuga, and R. Funahashi,*"Oxide Thermoelectric Materials: A Nanostructuring Approach",* Annual Review of Materials Research, 40, 363 (2010).
4. S. Ohta, T. Nomura, H. Ohta, and K. Koumoto,*"High-temperature carrier transport and thermoelectric properties of heavily La- or Nb-doped* $SrTiO_3$ *single crystals",* Journal of Applied Physics, 97, 034106 (2005).
5. S. Lee, G. Yang, R.H.T. Wilke, S. Trolier-McKinstry, and C.A. Randall,*"Thermopower in highly reduced n-type ferroelectric and related perovskite oxides and the role of heterogeneous nonstoichiometry",* Physical Review B, 79, 134110 (2009).
6. L.-D. Zhao, S.-H. Lo, Y. Zhang, H. Sun, G. Tan, C. Uher, C. Wolverton, V.P. Dravid, and M.G. Kanatzidis,*"Ultralow thermal conductivity and high thermoelectric figure of merit in SnSe crystals",* Nature, 508, 373 (2014).
7. K. Biswas, J. He, I.D. Blum, C.-I. Wu, T.P. Hogan, D.N. Seidman, V.P. Dravid, and M.G. Kanatzidis,*"High-performance bulk thermoelectrics with all-scale hierarchical architectures",* Nature, 489, 414 (2012).
8. H. Muta, K. Kurosaki, and S. Yamanaka,*"Thermoelectric properties of reduced and La-doped single-crystalline* $SrTiO_3$*",* Journal of Alloys and Compounds, 392, 306 (2005).
9. H. Ohta, S. Kim, Y. Mune, T. Mizoguchi, K. Nomura, S. Ohta, T. Nomura, Y. Nakanishi, Y. Ikuhara, M. Hirano, H. Hosono, and K. Koumoto,*"Giant thermoelectric Seebeck coefficient of a two-dimensional electron gas in* $SrTiO_3$*",* Nat Mater, 6, 129 (2007).
10. R. Venkatasubramanian,*"Lattice thermal conductivity reduction and phonon localizationlike behavior in superlattice structures",* Physical Review B, 61, 3091 (2000).
11. Y. Kinemuchi, K.-i. Mimura, A. Towata, and K. Kato,*"Thermoelectric Properties of Rare Earth-Doped* $SrTiO_3$ *Nanocubes",* Journal of Electronic Materials, 42, 1 (2013).
12. H.C. N. Wang, H. He, W. Norimatsu, M. Kusunoki & K. Koumoto,*"Enhanced thermoelectric performance of Nb-doped* $SrTiO_3$ *by nano-inclusion with low thermal conductivity",* Scientific Reports, 3, 3449 (2013).
13. C. Yu, M.L. Scullin, M. Huijben, R. Ramesh, and A. Majumdar,*"Thermal conductivity reduction in oxygen-deficient strontium titanates",* Applied Physics Letters, 92, 191911 (2008).

14. T. Teranishi, Y. Ishikawa, H. Hayashi, A. Kishimoto, M. Katayama, and Y. Inada,*"Thermoelectric Efficiency of Reduced $SrTiO_3$ Ceramics Modified with La and Nb",* Journal of the American Ceramic Society, 96, 2852 (2013).
15. J. Liu, C.L. Wang, Y. Li, W.B. Su, Y.H. Zhu, J.C. Li, and L.M. Mei,*"Influence of rare earth doping on thermoelectric properties of $SrTiO_3$ ceramics",* Journal of Applied Physics, 114, 223714 (2013).
16. H.C. Wang, C.L. Wang, W.B. Su, J. Liu, Y. Zhao, H. Peng, J.L. Zhang, M.L. Zhao, J.C. Li, N. Yin, and L.M. Mei,*"Enhancement of thermoelectric figure of merit by doping Dy in $La_{0.1}Sr_{0.9}TiO_3$ ceramic",* Materials Research Bulletin, 45, 809 (2010).
17. K. Kato, M. Yamamoto, S. Ohta, H. Muta, K. Kurosaki, S. Yamanaka, H. Iwasaki, H. Ohta, and K. Koumoto,*"The effect of Eu substitution on thermoelectric properties of $SrTi_{0.8}Nb_{0.2}O_3$",* Journal of Applied Physics, 102, 116107 (2007).
18. S.R.S. Kumar, A.Z. Barasheed, and H.N. Alshareef,*"High Temperature Thermoelectric Properties of Strontium Titanate Thin Films with Oxygen Vacancy and Niobium Doping",* ACS Applied Materials & Interfaces, 5, 7268 (2013).
19. D.G. Cahill,*"Thermal conductivity measurement from 30 to 750 K: the 3 omega method",* Review of Scientific Instruments, 61, 802 (1990).
20. T. Borca-Tasciuc, A.R. Kumar, and G. Chen,*"Data reduction in 3ω method for thin-film thermal conductivity determination",* Review of Scientific Instruments, 72, 2139 (2001).
21. A. Duran, E. Martinez, J.A. Diaz, and J.M. Siqueiros,*"Ferroelectricity at room temperature in Pr-doped $SrTiO_3$",* Journal of Applied Physics, 97, 104109 (2005).
22. R.D. Shannon,*"Revised effective ionic radii and systematic studies of interatomic distances in halides and chalcogenides",* Acta Crystallographica Section A, 32, 751 (1976).
23. W. Wunderlich, H. Ohta, and K. Koumoto,*"Enhanced effective mass in doped $SrTiO_3$ and related perovskites",* Physica B: Condensed Matter, 404, 2202 (2009).
24. R. Perez-Casero, J. Perrière, A. Gutierrez-Llorente, D. Defourneau, E. Millon, W. Seiler, and L. Soriano,*"Thin films of oxygen-deficient perovskite phases by pulsed-laser ablation of strontium titanate",* Physical Review B, 75, 165317 (2007).
25. T. Tomio, H. Miki, H. Tabata, T. Kawai, and S. Kawai,*"Control of electrical conductivity in laser deposited $SrTiO_3$ thin films with Nb doping",* Journal of Applied Physics, 76, 5886 (1994).
26. S.R. Sarath Kumar, A.I. Abutaha, M.N. Hedhili, and H.N. Alshareef,*"Modeling the transport properties of epitaxially grown thermoelectric oxide thin films using spectroscopic ellipsometry",* Applied Physics Letters, 100, 052110 (2012).
27. T.A. Cain, A.P. Kajdos, and S. Stemmer,*"La-doped $SrTiO_3$ films with large cryogenic thermoelectric power factors",* Applied Physics Letters, 102, 182101 (2013).

28. V.S.R. Kodigala Subba Ramaiah, A K Bhatnagar, R D Tomlinson, R D Pilkington, A E Hill, S J Chang, Y K Su and F S Juang,*"Optical, structural and electrical properties of tin doped indium oxide thin films prepared by spray-pyrolysis technique",* Semiconductor Science and Technology, 15, 676 (2000).
29. H.Y. Liu, V. Avrutin, N. Izyumskaya, Ü. Özgür, A.B. Yankovich, A.V. Kvit, P.M. Voyles, and H. Morkoç,*"Electron scattering mechanisms in GZO films grown on a-sapphire substrates by plasma-enhanced molecular beam epitaxy",* Journal of Applied Physics, 111, 103713 (2012).
30. N.W. Ashcroft and N.D. Mermin, *"Solid State Physics"*. (1976).
31. R. Moos, A. Gnudi, and K.H. Hardtl,*"Thermopower of $Sr_{1-x}La_xTiO_3$ ceramics",* Journal of Applied Physics, 78, 5042 (1995).
32. T. Yamamoto, T. Sakemi, K. Awai, and S. Shirakata,*"Dependence of carrier concentrations on oxygen pressure for Ga-doped ZnO prepared by ion plating method",* Thin Solid Films, 451, 439 (2004).
33. T. Okuda, K. Nakanishi, S. Miyasaka, and Y. Tokura,*"Large thermoelectric response of metallic perovskites: $Sr_{1-x}La_xTiO_3$",* Physical Review B, 63, 113104 (2001).
34. M. Matsuo, S. Okamoto, W. Koshibae, M. Mori, and S. Maekawa,*"Nonmonotonic temperature dependence of thermopower in strongly correlated electron systems",* Physical Review B, 84, 153107 (2011).
35. J. Liu, C.L. Wang, W.B. Su, H.C. Wang, P. Zheng, J.C. Li, J.L. Zhang, and L.M. Mei,*"Enhancement of thermoelectric efficiency in oxygen-deficient $Sr_{1-x}La_xTiO_{3-\delta}$ ceramics",* Applied Physics Letters, 95, 162110 (2009).
36. J. Liu, C.L. Wang, W.B. Su, H.C. Wang, J.C. Li, J.L. Zhang, and L.M. Mei,*"Thermoelectric properties of $Sr_{1-x}Nd_xTiO_3$ ceramics",* Journal of Alloys and Compounds, 492, L54 (2010).
37. N.N. David A. Muller, Akira Ohtomo, John L. Grazul & Harold Y. Hwang,*"Atomic-scale imaging of nanoengineered oxygen vacancy profiles in $SrTiO_3$",* Nature, 430, 657 (2004).
38. R.-z. Zhang, C.-l. Wang, J.-c. Li, W.-b. Su, J.-l. Zhang, M.-l. Zhao, J. Liu, Y.-f. Zhang, and L.-m. Mei,*"Determining Seebeck coefficient of heavily doped La:$SrTiO_3$ from density functional calculations",* Solid State Sciences, 12, 1168 (2010).
39. K. Uchida, S. Tsuneyuki, and T. Schimizu,*"First-principles calculations of carrier-doping effects in $SrTiO_3$",* Physical Review B, 68, 174107 (2003).
40. P.-P. Shang, B.-P. Zhang, Y. Liu, J.-F. Li, and H.-M. Zhu,*"Preparation and Thermoelectric Properties of La-Doped $SrTiO_3$ Ceramics",* Journal of Electronic Materials, 40, 926 (2011).
41. A. Majumdar,*"Microscale Heat Conduction in Dielectric Thin Films",* Journal of Heat Transfer, 115, 7 (1993).
42. A.V. Kovalevsky, A.A. Yaremchenko, S. Populoh, A. Weidenkaff, and J.R. Frade,*"Effect of A-Site Cation Deficiency on the Thermoelectric Performance of Donor-Substituted Strontium Titanate",* The Journal of Physical Chemistry C, 118, 4596 (2014).
43. E. Flage-Larsen and Ø. Prytz,*"The Lorenz function: Its properties at optimum thermoelectric figure-of-merit",* Applied Physics Letters, 99, 202108 (2011).

44. S. Ohta, T. Nomura, H. Ohta, M. Hirano, H. Hosono, and K. Koumoto,*"Large thermoelectric performance of heavily Nb-doped $SrTiO_3$ epitaxial film at high temperature",* Applied Physics Letters, 87, 092108 (2005).
45. H.C. Wang, C.L. Wang, W.B. Su, J. Liu, H. Peng, Y. Sun, J.L. Zhang, M.L. Zhao, J.C. Li, N. Yin, and L.M. Mei,*"Synthesis and thermoelectric performance of Ta doped $Sr_{0.9}La_{0.1}TiO_3$ ceramics",* Ceramics International, 37, 2609 (2011).
46. H.C. Wang, C.L. Wang, W.B. Su, J. Liu, H. Peng, J.L. Zhang, M.L. Zhao, J.C. Li, N. Yin, and L.M. Mei,*"Substitution effect on the thermoelectric properties of reduced Nb-doped $Sr_{0.95}La_{0.05}TiO_3$ ceramics",* Journal of Alloys and Compounds, 486, 693 (2009).

Chapter 7.

Enhanced Thermoelectric Figure of Merit in Thermally Robust, Nanostructured Superlattices based on $SrTiO_3$

(Reprinted with permission from *Chemistry of Materials, 27, 2165*. Copyright 2015, American Chemical Society)

7.1 Abstract

Thermoelectric (TE) metal oxides overcome crucial disadvantages of traditional heavy-metal-alloy based TE materials, such as toxicity, scarcity, and instability at high temperatures. Here, we report the TE properties of metal oxide superlattices, composed from alternative layers of 5% Pr^{3+} doped $SrTiO_{3-\delta}$ (SPTO) and 20% Nb^{5+} doped $SrTiO_{3-\delta}$ (STNO) fabricated using pulsed laser deposition (PLD). Excellent stability is established for these superlattices by maintaining the crystal structure and reproducing the TE properties after long-time (20 hours) annealing at high temperature (~1000 K). The introduction of oxygen vacancies as well as extrinsic dopants (Pr^{3+} and Nb^{5+}), with different masses and ionic radii, at different lattice sites in SPTO and STNO layers, respectively, results in a substantial reduction of thermal conductivity via scattering a wider range of phonon spectrum without limiting the electrical transport and thermopower, and hence leading to an enhancement in the figure of merit (ZT). The superlattice composed of 20 SPTO/STNO pairs, 8 unit cells of each layer, exhibits a ZT of 0.46 at 1000 K, highest among $SrTiO_3$-based thermoelectrics.

7.2 Introduction

The rapid increase in global energy consumption and the inability of conventional energy conversion technologies, such as combustion of fossil fuels, to reduce their negative impact on environment, have led to significant activities in developing alternative energy conversion technologies. One of these promising technologies is thermoelectrics (TE), which possess sustainable, reliable, and scalable characteristics in converting waste heat into electricity. Currently, TE devices cannot replace the traditional power generation systems due to their relatively low conversion efficiencies. The performance of TE materials is evaluated in terms of a dimensionless figure of merit $ZT = \sigma S^2 T/\lambda$, where σ is electrical conductivity, S is Seebeck coefficient, T is the absolute temperature, and λ is the total thermal conductivity [1]. The total thermal conductivity consists of contributions from electronic (λ_e) and lattice (λ_l) thermal conductivities (*i.e.* $\lambda = \lambda_e + \lambda_l$). Unfortunately, all of the physical quantities describing ZT are strongly correlated, which makes enhancement of ZT extremely challenging [2]. The TE community has been intensively targeting to achieve $ZT \geq 3$ in order to make the performance of TE solid state devices competitive with traditional energy conversion systems. Although heavy-metal-based alloys, such as SnSe (~2.6) [3] and PbTe (~2.2) [4], exhibit high ZT, they are not attractive for wide range of applications because they are toxic, decomposable, and their constituents are not naturally abundant. For these reasons, metal oxides, which do not have the above said disadvantages of traditional TE materials, emerge as reasonable and viable alternatives. Among metal oxides, $SrTiO_3$

(STO) is a promising TE material, particularly at high temperatures, as it has a high melting point (2353 K) and naturally abundant constituent elements [5]. STO, with a cubic perovskite crystal structure (a=3.905 Å), is one of the well-studied oxides [6] and has a wide band gap [7], high S [8], and huge electron mobility at T < 10 K [9]. Furthermore, σ of STO can be tuned from insulating to metallic by substitutional doping in Sr^{2+} (e.g. with La^{3+}) [10] and Ti^{4+} sites (e.g. with Nb^{5+}) [11] or by creating oxygen vacancies [12] but at the expense of S, limiting the power factor ($PF = \sigma S^2 T$). However, STO exhibits a reasonably high PF (~1.5 W m^{-1} K^{-1}) [11], which is comparable to those of the best known TE materials. Nevertheless, STO possesses relatively low ZT compared to traditional TE materials because of its high λ at room temperature (~11 W m^{-1} K^{-1}) [13]. Considerable improvement in ZT is required to make STO a practical TE material and one way to do so is to reduce λ by using nano-structures, such as superlattices (SLs) [14, 15], nano-cubes [16], and nano-inclusions [17], while maintaining the high PF of the final structures. For instance, Ohta *et al.* reported [14] that stoichiometric STNO/STO superlattices may exhibit a relatively high and effective ZT of 0.24 at 300 K, by exploiting the phenomenon of 2D electron gas in STO. Despite all the attractive properties of superlattices, the stability at high temperatures comprises a crucial challenge in terms of having sustainable nanostructured TE devices. One crucial challenge regarding nanostructured TE devices, such as SLs, is the stability at high temperatures. These devices may be operated under high thermal gradients, for long duration at high operating temperatures, and structural stability, without compromising TE performance assumes great significance. Previous studies have shown that the thermal stability of some SLs is limited to operating temperatures below a threshold value beyond which the SLs structures are destroyed, for example, STO-based SLs at 900-950 K [18, 19], and Bi_2Te_3-based SLs at 423 K [20].

In this work, we report the TE properties and the excellent high temperature stability of SLs composed of 5% Pr^{3+} doped $SrTiO_{3-\delta}$ (SPTO) and 20% Nb^{5+} doped $SrTiO_{3-\delta}$ (STNO) layers (Figure 7.1(a)), represented as $[(SPTO)_a|(STNO)_b]_{20}$, where a and b are the number of unit cells of SPTO and STNO layers, respectively, and the total number of SPTO/STNO pairs is 20 for all SLs. The SLs are labeled depending on the relative thickness ratio of SPTO to STNO layers, a/b (see Table 7.1). Epitaxial cube-on-cube growth of SPTO and STNO unit cells in SLs, confirmed by x-ray diffraction (XRD) and scanning transmission electron microscope (STEM), facilitates the electrical transport. Continuum analysis is used to calculate the in-plane λ of SLs from the measured λ values of SPTO and STNO single layers. The introduction of alternating, oxygen-deficient SPTO and STNO layers (Figure 7.1(a)) reduces λ of SLs via scattering of a wider range of phonon spectrum. In other words, short-wavelength phonons can be scattered by the presence of different extrinsic dopants (Pr^{3+} and Nb^{5+}), at different lattice sites (A-site and B-site), while longer-wavelength phonons can be scattered by the clusters of oxygen vacancies (few nanometers) [21, 22] in each layer as well as from interfaces between the layers [23]. The high-temperature stability of $[(SPTO)_a|(STNO)_b]_{20}$ SLs, as confirmed from the stable crystal structure and reproducible TE properties, even after 20 hours of operation at 1000 K, makes the STO-based SLs extremely attractive for high temperature applications.

7.3 Experimental Section

Films and SLs were deposited by PLD (Neocera, Beltsville, MD) using a KrF excimer laser (λ=248 nm, pulse duration ~20 ns, repetition rate =10 Hz, and fluence of 3 J cm^{-2}). Samples were deposited by ablation of 5% Pr^{3+} and 20% Nb^{5+} doped STO targets, for SPTO and STNO layers, respectively. Prior depositions, the surfaces of the targets were cleaned by laser ablation using 1000 pulses. Each target was held on a rotating carousel to ensure a uniform ablation. The PLD chamber was evacuated to a high vacuum level (~10^{-9} Torr) before each deposition. In order to create sufficient oxygen vacancies, a mass flow controller was used to introduce 20 mTorr of Ar as a reducing gas. Films were deposited on single-side polished <001> oriented LAO substrates of dimensions 10x10x0.5 mm^3 with a_{LAO}= 3.82 Å, held at substrate temperature of 973 K. Before each deposition, the substrates were cleaned ultrasonically in deionized water and isopropyl alcohol, and dried using high purity nitrogen gas.

The phase purity of the SLs was determined from the analysis of θ-2θ (Bragg-Brentano) scan using an x-ray diffractometer (D8 Bruker, AXS System, Germany). STEM was performed on an FEI high base Titan STEM operated at 300 kV with a probe spherical aberration (Cs) corrector and a monochromator (not turned on). The camera length was set at 145 mm, which corresponded to a STEM signal collection angle between 40 and 200 mrad for the high angle angular dark field (HAADF) detector. Under such a condition, the STEM image contrast is dominated by atomic number (Z-contrast). The specimen was oriented at the <001> zone axis. For this orientation the electron beam saw three atomic column configurations, pure Sr columns, pure O columns, and Ti and O mixed columns. The Sr, Ti and O atoms have an atomic number of 38, 22, and 8 respectively. The high angle angular dark field imaging condition will make Sr atomic column brighter in contrast than Ti/O mixed atomic column. The pure O column will not show up due to the weak intensity of scattered electron.

σ and S were measured in the temperature range of 300– 1000 K by using respectively the linear four-probe and the differential methods, under Ar/H_2 (96% Ar and 4% H_2) ambient using a commercial setup (RZ2001i, Ozawa Science Co Ltd., Nagoya, Japan). At any temperature, σ was measured first, followed by S by introducing a ΔT of ~4–10 K, between the voltage probes. The measurements of σ and S were then repeated at a higher sample temperature, thereby enabling studies on change in transport properties during heating. Room temperature Hall effect measurements were carried out using a physical property measurement system (PPMS) (Quantum Design, Inc., USA).

3ω method [24] was used to measure the cross-plane thermal conductivity of SPTO and STNO films. In this method, an ac current passes through metal line patterned on a film, and the amplitudes of the first and third harmonic voltage drops along the line were measured in order to extract the thermal conductivity of the films. A 200 nm thick Au film, with 20 nm thick Cr as an adhesive layer, were deposited on the films using sputtering. The Au films were patterned to linear heaters using photolithography and lift-off. The width (~10 μm) of Au heaters is much larger than films thickness (~500 nm) which allows us to measure the cross-plane thermal conductivity by applying one-dimensional heat flow model. In order to pattern the metal line on the electrically conductive STO films, an insulating layer is needed to prevent any leakage current. Therefore, a 100 nm of SiN_x was deposited on doped STO films and bare Si substrate using sputtering, and we measured the temperature rise from both samples. An algorithm was used to extract the temperature drops across the doped STO films from the rise in temperature across the two samples, using a comparative method [25].

7.4 Results and Discussion

The epitaxial growth of all samples is evident from the dominant {001} peaks in the out of plane (c-axis) XRD patterns in the θ-2θ geometry shown in Figure 7.1(b). The diffraction peaks of the {001} planes from LAO (marked 'S'), SLs, and films can be seen, while reflections from other crystal orientations are of negligible intensity, indicating a preferential epitaxial growth of SLs and films on the substrate. Small satellite peaks (marked '*') are observed due to the periodic structure of SLs. High resolution XRD patterns in the θ-2θ geometry were done for (002) reflection from all samples and substrate (Figure 7.1(c)) to detect any change in lattice constant. The observed lattice constants are presented in Table 7.1. All samples possess lattice constants larger than that of stoichiometric STO (3.905 Å). However, it was reported [26, 27] that the unit cell volume of Pr^{3+} doped STO shrinks due to the substitution of Pr^{3+} (1.144 Å) with Sr^{2+} (1.44 Å). Another factor that should be taken into account is oxygen vacancies, which can play an important role in determining the lattice constant of STO. It has been reported by Luo *et al.* [28] that Ti–Ti bond is larger than Ti–O–Ti and this effect leads to a tetragonal distortion of the lattice and results in a larger lattice constant. Furthermore, it may be noted that creation of oxygen vacancies induces the formation of Ti^{3+} (0.67 Å) from Ti^{4+} (0.605 Å), adding to the increase in lattice constant [12]. On the other hand, STNO film has the largest lattice constant (3.960 Å) among the samples due to the substitution of Nb^{5+} (0.64 Å) for Ti^{4+} (0.605 Å) [29] as well as the presence of oxygen vacancies in the film. For SLs(1–5), the effective lattice constant decreases monotonically with a/b ratio. In other words, as a/b ratio increases, the contribution of the SPTO layers (lower lattice constant) to (002) XRD peak becomes more prominent compared to STNO layers (higher lattice constant), and hence the effective lattice constant of SLs decreases.

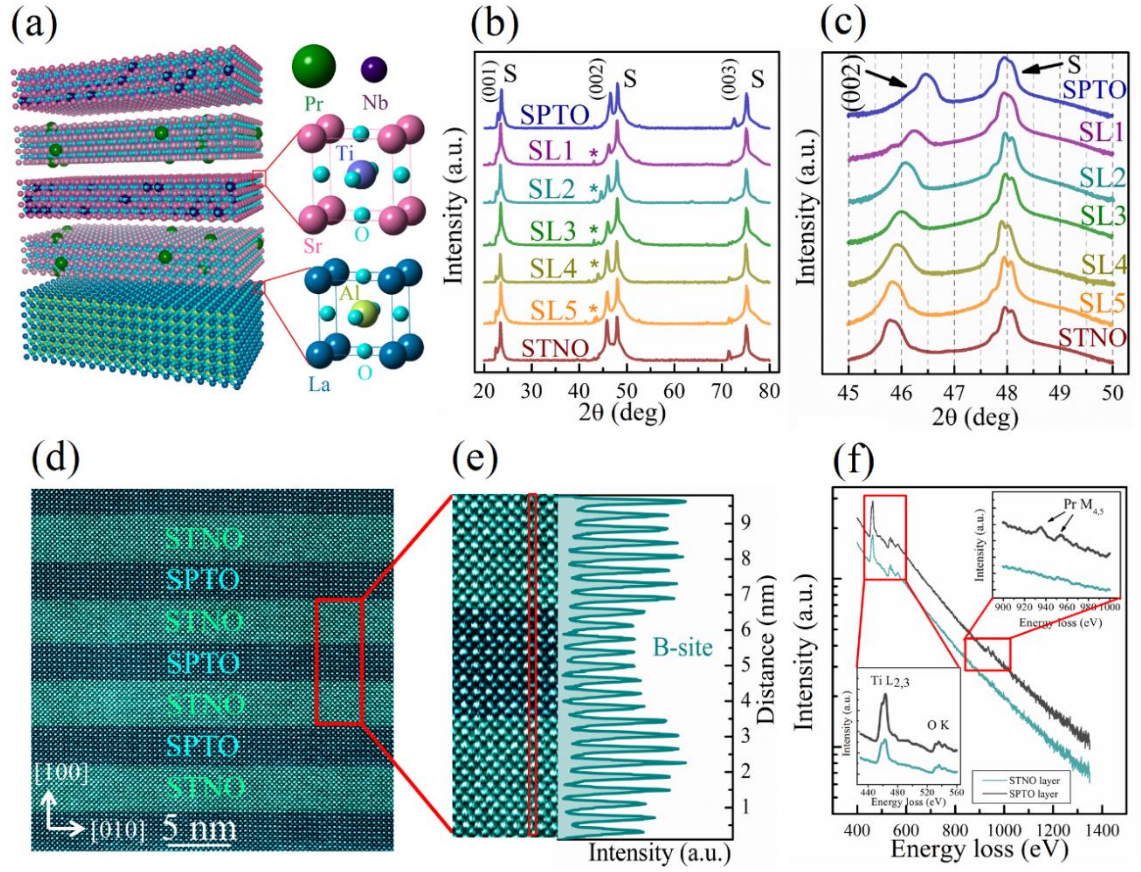

Figure 7.1. (a) Schematic diagram of epitaxial perovskite [SPTO$_a$|STNO$_b$]$_{20}$ SLs on LAO substrate. The unit cells of LAO substrate, STO, and the extrinsic dopants (Pr^{3+} and Nb^{5+}) in each layer are shown with arbitrary atomic sizes for illustration purpose. (b) θ-2θ XRD patterns for doped STO thin films grown on LAO substrate, peaks of {001} reflections are seen along with substrate peaks (marked by 'S') indicating the preferential epitaxial growth of the films and SLs on the substrates. (c) High resolution scan for (002) XRD peak revealing a shift in (002) peak position, depending on $\boldsymbol{a}/\boldsymbol{b}$ thickness ratio of the forming layers of SLs. (d) High resolution STEM image of SL3 confirms a cube-on-cube epitaxial growth with alternating dark and bright layers of SPTO and STNO, respectively. (e) HAADF intensity profile of B-site of SL3 proves that Nb^{5+} ions substitute Ti^{4+} ions as STNO layers are brighter than STNO layers since Nb^{5+} (Z=41) ions are heavier than Ti^{4+} (Z=22). (f) EELS spectra obtained from SPTO and STNO layers confirming that dark layers are SPTO as Pr M$_{4,5}$-edge is found in the range 900–1000 eV while other edges (Ti L$_{2,3}$ and O K) are also observed for both SPTO and STNO layers (430–560 eV).

Figure 7.1(d) shows STEM image of as-grown SL3 which confirms the high quality of epitaxial layer-by-layer growth of both SPTO and STNO layers. The STEM image shows alternating bright and dark regions, both of which are about 8 unit cells thick, with very sharp interfaces, as confirmed by the intensity of high angle annular dark field (HAADF) line profile of B-site, across the layers (Figure 7.1(e)). The alternating change in contrast is due to the replacement of Ti^{4+} atoms by Nb^{5+} ions. As Nb^{5+} ions (Z=41) are heavier than Ti^{4+} ions (Z=22), the replacement will make Ti^{4+}/ Nb^{5+}/O^{2-} columns in STNO layers brighter in contrast than Ti^{4+}/ O^{2-} columns in SPTO layers. It is also deduced from B-site HAADF intensity profile that Pr^{3+} (Z=59) ions do not substitute Ti^{4+} (Z=22) ions. Our deduction is further supported by the analysis of the electron energy loss spectroscopy (EELS) spectra shown in Figure 7.1(f), obtained from both dark and bright layers. The spectrum obtained from the dark layer clearly shows the presence of Pr $M_{4,5}$-edge, as shown in inset of Figure 7.1(f) (900–1000 eV) [30], confirming that the dark regions represent SPTO layers. Other edges (Ti $L_{2,3}$ and O K) are also observed for both SPTO and STNO layers (430–560 eV) [31].

The temperature dependence of σ is plotted in Figure 7.2(a). In all samples, σ decreases with temperature showing a degenerate semiconducting behavior in the entire temperature range as a consequence of electrons excited to the conduction band by oxygen vacancies and the substitution of Ti^{4+} and Sr^{2+} with Nb^{5+} and Pr^{3+} in STNO and SPTO layers, respectively. SPTO film has lower σ than STNO film which is attributed to the difference in carrier concentrations resulting from different doping levels (n_{SPTO}=9.1×10^{20} cm^{-3} and n_{STNO}=2.78×10^{21} cm^{-3}), as $\sigma = ne\mu$, where n, e, and μ are carrier concentration, electronic charge, and electrical mobility, respectively. Furthermore, it was reported [32] that the effective mass (m^*) of free electrons in STO is influenced by lattice constant, *i.e.* the smaller the lattice constant, the higher m^*, and hence the lower μ leading to lower σ as observed for SPTO film. On the other hand, the in-plane electrical conductivity ($\sigma_{\parallel}$) of SLs can be described by treating SPTO and STNO layers as parallel non-interacting conductors,

$$\sigma_{\parallel} = \frac{a\sigma_{SPTO} + b\sigma_{STNO}}{(a+b)} = \frac{(a/b)\sigma_{SPTO} + \sigma_{STNO}}{(a/b)+1}, \tag{7.1}$$

where σ_{SPTO} and σ_{STNO} are electrical conductivity of SPTO and STNO layers, respectively [33]. At any temperature, $\sigma_{\parallel}$ of SLs decreases as a/b ratio increases since $\sigma_{SPTO} < \sigma_{STNO}$.

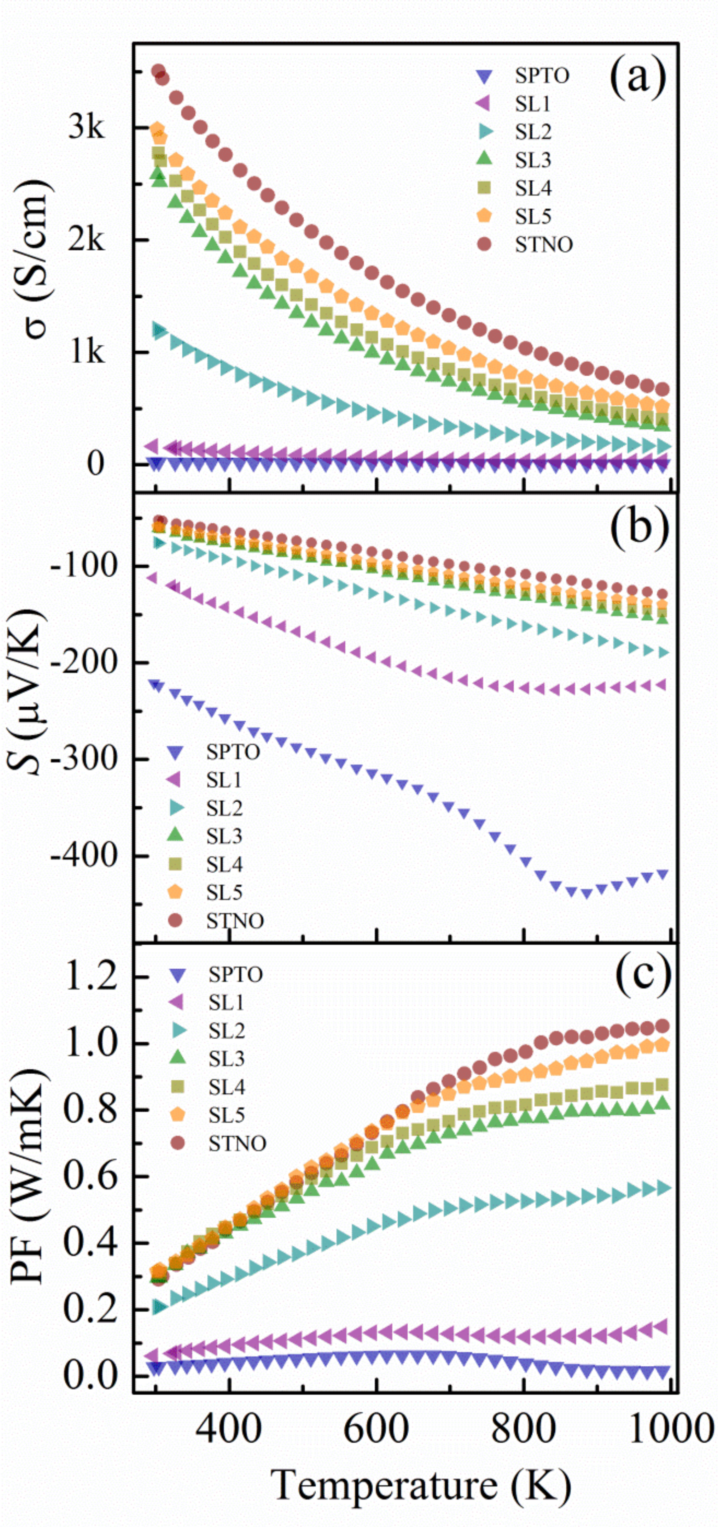

Figure 7.2. (a) Electrical conductivity (b) Seebeck coefficient, and (c) power factor of the films and SLs as a function of temperature.

Figure 7.2(b) shows the temperature dependence of S. All samples exhibit negative S indicating n-type conduction. As a consequence of different doping levels in SPTO and STNO films, SPTO film has the highest absolute Seebeck coefficient ($|S|$) while STNO film has the lowest $|S|$ in the whole temperature range, as $|S|$ decreases with n and increases with m^* of electrons in degenerate semiconductors ($S \,\alpha\, m^* n^{-2/3}$).[1] In addition, SPTO is expected to have higher m^*in the in-plane direction as discussed earlier [32], and hence higher $|S|$ which is indeed observed for SPTO film (Table 7.1). In SLs, the in-plane Seebeck coefficient ($S_{||}$) is determined from the contribution of SPTO and STNO layers as they can be treated as parallel conductors ($S_{||} = ((a/b)\, S_{SPTO}\sigma_{SPTO} + S_{STNO}\sigma_{STNO})/((a/b)\, \sigma_{SPTO} + \sigma_{STNO})$).[33] So, as a/b ratio increases, $|S_{||}|$ increases since $|S_{SPTO}|$>$|S_{STNO}|$ at any temperature. All samples have linear S-T relationship indicating a typical degenerate semiconducting behavior, except for SPTO film and SL1, this linearity is no longer obeyed at ~750 K. This deviation from linearity can be attributed to the change in the scattering mechanism of the free electrons as they are scattered predominantly by acoustic phonons at high temperatures [34]. Above ~900 K, $|S|$ of SPTO and SL1 decreases with temperature because of the presence of randomly distributed oxygen vacancy clusters [21], which is common in STO films grown by PLD [22]. These clusters are in different degrees of reduction [31], and the lightly reduced regions can be reduced more at very high temperatures during measurements in a reducing ambient (Ar/H_2 in the present case), leading to a slight decrease $|S|$ as observed in Figure 7.2(b).

Figure 7.2(c) shows the PF as a function of temperature. STNO film has the highest PF (1.05 W m^{-1} K^{-1}) at 1000 K. It is interesting to note that the PF of SLs(3–5) is not reduced much by the presence of SPTO layers (lowest PF) which gives the opportunity to these SLs to have higher ZT than STNO film because of their expected lower λ due to the higher phonon scattering, which is indeed confirmed and to be discussed later.

Our SLs exhibit excellent stability of TE properties at high temperatures ($\sim$1000 K). To demonstrate this stability, TE properties of SL3 was measured in Ar/H_2 ambient up to T $\sim$1000 K, which was maintained for 20 hours, before cooling down to room temperature (Figure 7.3(a)). σ (blue curve) and S (purple curve) were measured during heating, soaking and cooling. In the heating regime (0 hours ≤ t ≤5.4 hours), SL3 shows a typical degenerate semiconductor behavior, i.e., as temperature increases, σ decreases, while $|S|$ increases, as previously discussed. During the soaking at 1000 K for 20 hours (5.4 hours ≤ t ≤25.4 hours), σ and $|S|$ of SL3 show a stable and constant performance with time. During this period, small temperature variations (ΔT $\sim$10 K) were applied to make the measurement of S possible. (It may be noted that for measuring S, a temperature gradient is inherently necessary and hence the sample cannot be, in principle and practice, maintained strictly at 1000 K). When cooled to room temperature (25.4 hours ≤ t ≤30 hours), both σ and S returned to their initial room-temperature values, suggesting an excellent reproducibility of TE properties. θ-2θ XRD patterns of as-grown and annealed SL3 are plotted in Figure 7.3(b). It is evident from these patterns that the epitaxial nature of SL3 on LAO is preserved after annealing as observed from {001} peaks of SL3 and LAO substrate.

Small satellite peaks (marked by '*') are observed also in both patterns resulting from the diffraction by SLs, as discussed earlier. Furthermore, TEM images were obtained (Figure 7.4(a) and (b)) for the two samples showing no change in the atomic structure. Furthermore, no inter-diffusion of atoms between SPTO and STNO layers is observed before and after annealing, confirming the robustness of the SLs.

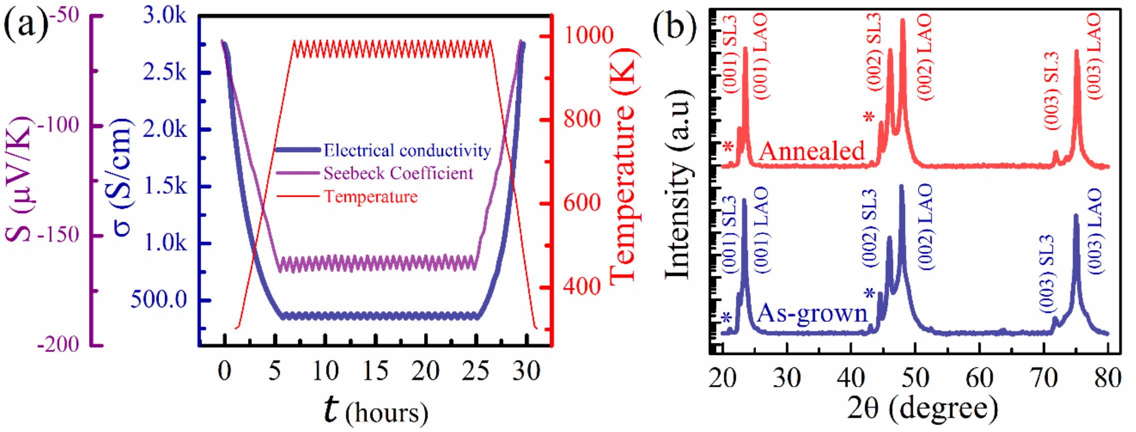

Figure 7.3. The temperature dependence of the electrical conductivity and Seebeck coefficient of SL3 which show excellent stability and reproducible TE properties after 20 hours of continuous annealing. (b) XRD patterns of as-grown and annealed SL3, the patterns show no difference before and after annealing suggesting that the epitaxial crystal structure of SL3 is preserved.

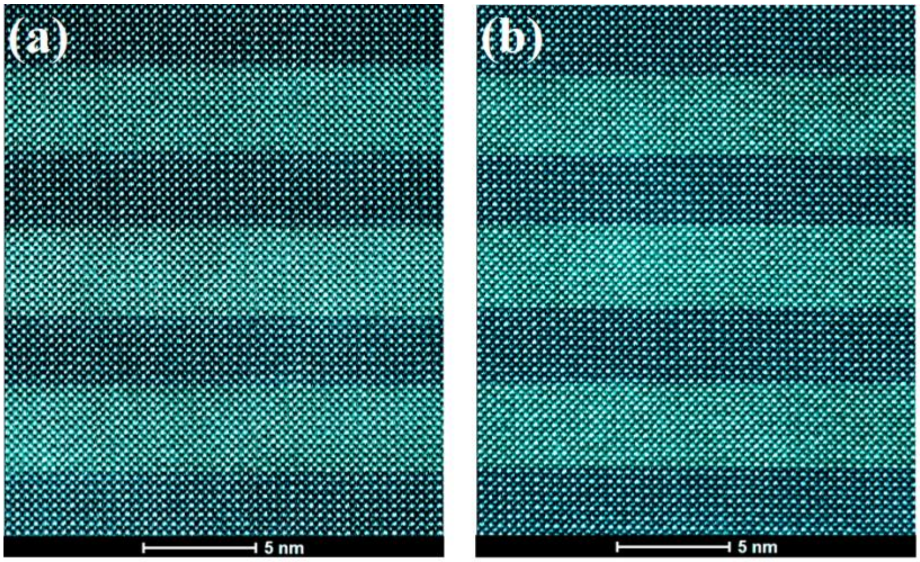

Figure 7.4. TEM images for (a) as-grown and (b) annealed SL3.

It is worthy to note that the TE properties of STO-based films behave differently, if the ambient used for TE measurements is changed. For example, when measured in air up to 1000 K, a reduction in σ during cooling has been observed for STNO films, which can be attributed to the refilling process of oxygen vacancies during the measurement [35]. Since ubiquitous use of TE devices demand continuous operation in air, the SLs need to be prevented from exposure to air. Hence, a protective barrier coating may be provided to the TE generator after integrating them in real devices. Another issue that TE devices based on thin films and SLs encounter is the difficulty in maintaining high temperature gradients in the cross-plane geometry. Alternative approaches have been developed to overcome this problem, by allowing the heat and electrical fluxes to be in the in-plane direction rather than the cross-plane one [36]. For instance, two different SLs (p-type and n-type) could be grown on both sides of an insulating substrate (e.g. LAO) while metal contacts are connected to the lateral edges of the epitaxial SLs and the substrate to facilitate the in-plane heat and electrical fluxes. One possible metal contact that can be used in such devices is Ag since it is compatible with oxides and shows good stability at high temperatures as discussed elsewhere [37].

In 3ω method, the cross plane thermal conductivity $(\lambda_{\perp})$ can be extracted from temperature rise (ΔT) on the microheaters due the ac current I(ω). Figure 7.5(a) and (b) show the temperature rise of the Au microheaters as a function of current frequency (ω) at 100 K and 300 K, respectively. ΔT_{SPTO} and ΔT_{STNO} are the frequency-independent temperature rises due to the presence of SPTO and STNO films, respectively. Since the width of the Au microheater is 10 μm which is much larger than the thickness (500 nm) of the film, the heat flow can be described as one dimensional, and the additional film has a frequency-independent temperature rise given by [25]:

$$\Delta T_f = \frac{P_l \, t_f}{w \, \lambda_f}, \qquad (7.2)$$

where P_l, λ_f, t_f, and w are the heating power unit length, the thermal conductivity of the additional film, the thickness of the film, and the width of the microheater, respectively. It is evident that ΔT resulted from SPTO film is higher than ΔT resulted from STNO film, which is attributed to lower λ_f of SPTO film compared to STNO film (Equation 7.2).

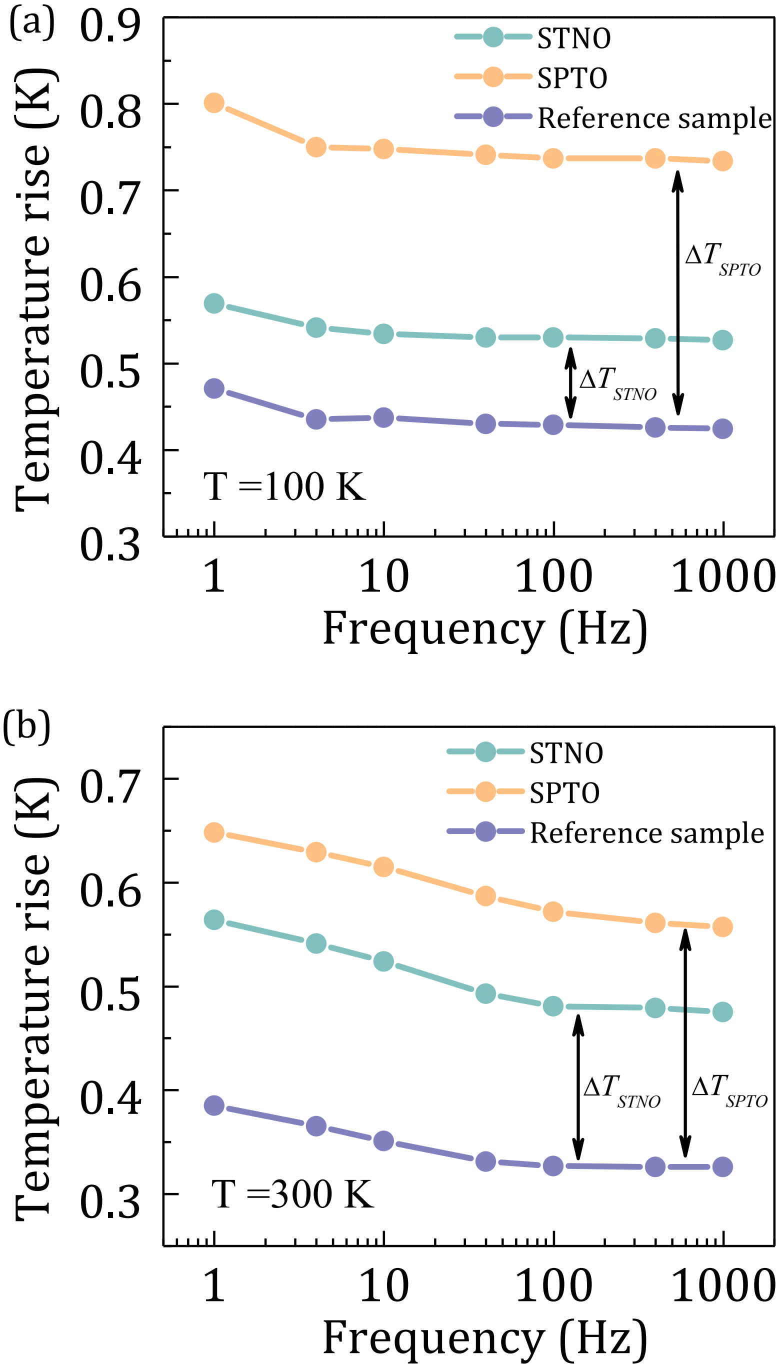

Figure 7.5. Temperature rise of the Au microheaters as a function of current frequency (ω) at (a) 100 K and (b) 300 K. $\boldsymbol{\Delta T_{SPTO}}$ and $\boldsymbol{\Delta T_{STNO}}$ are the frequency-independent temperature rises due to the presence of SPTO and STNO films, respectively.

The cross-plane thermal conductivities ($\lambda_{\perp}$) of the individual SPTO (λ_{SPTO}) and STNO (λ_{STNO}) films were measured in the temperature range 100< T<300 K as shown in Figure 7.6(a). We assume that the in-plane thermal conductivity ($\lambda_{\|}$) is identical to $\lambda_{\perp}$ since the films have cubic lattice structure, and hence the properties are isotropic. The room-temperature $\lambda_{\perp}$ of both films is lower than those reported for stoichiometric bulk STO (11 W m^{-1} K^{-1}) [21] and La^{3+} doped bulk STO (9 W m^{-1} K^{-1}) [38]. This reduction in $\lambda_{\perp}$ is caused by scattering of phonons with different frequencies [39, 40] due to the randomly distributed scattering centers embedded in the lattice such as oxygen vacancy clusters (few nanometers) [21] and the extrinsic dopants located at A-site and B-site in SPTO and STNO layers, respectively [41, 42]. The peak value of $\lambda_{\perp}$ at low temperature is typical for crystalline materials [21, 43], and it occurs when the mean free path of phonons is comparable to the crystallite size. The peak value of $\lambda_{\perp}$ separates the low temperature region, where phonon scattering is dominated by surfaces and lattice imperfections, from the high temperature region, where phonon-phonon scattering is dominant.

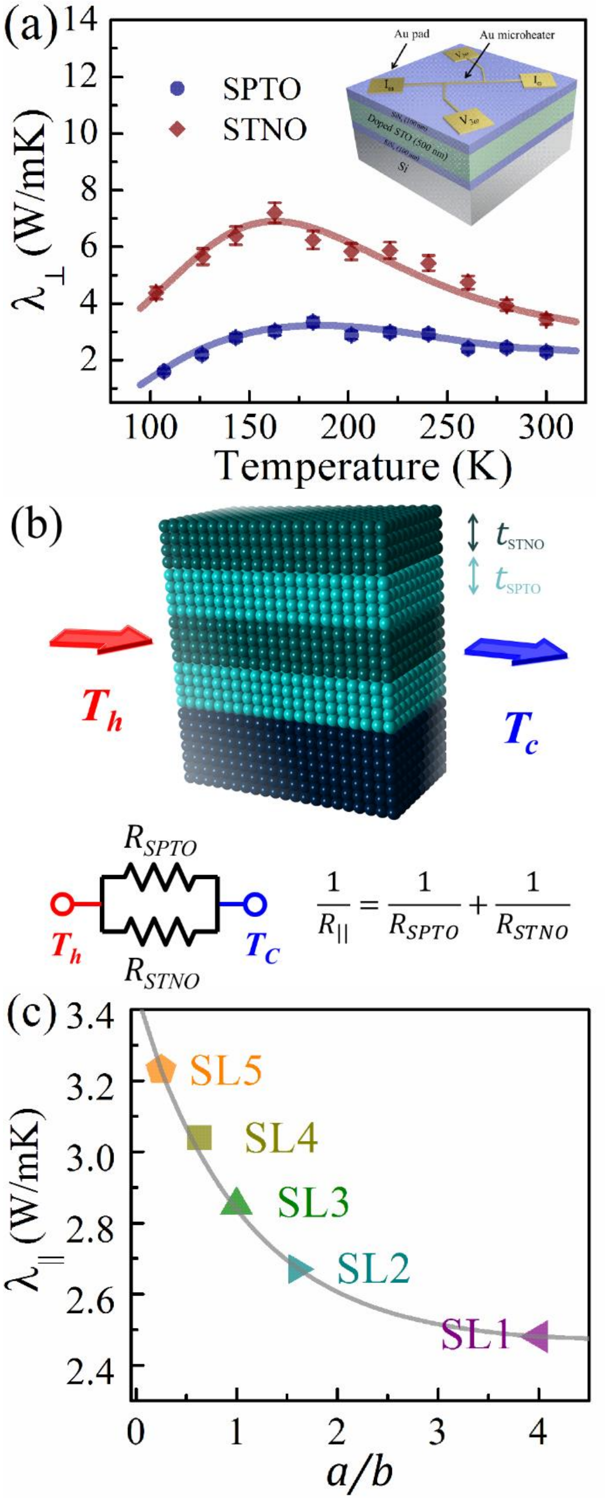

Figure 7.6. (a) The temperature dependence of the cross-plane thermal conductivity of SPTO and STNO films, and the inset to (a) shows a schematic diagram of the sample used in 3ω measurement. (b) A schematic representation of in-plane heat flow in SLs where continuum analysis is used to extract the in-plane thermal conductivity of SLs by treating SPTO and STNO layers as resistors thermally connected in parallel. (c) Calculated in-plane thermal conductivity of SLs at room temperature.

We estimate $\lambda_{\|}$ of SLs using continuum analysis [44] from the room-temperature $\lambda_{\perp}$ of SPTO and STNO films. In this analysis, if the alternative SPTO and STNO layers in SLs are assumed to be continuous and perfectly contacted, they can be regarded as thermal resistances which are thermally connected in parallel as illustrated in Figure 7.6(b). Then, one can calculate $\lambda_{\|}$ of SLs using the equation [44-46]:

$$\lambda_{\|} = \frac{(a/b)\lambda_{SPTO} + \lambda_{STNO}}{(a/b)+1}. \tag{7.3}$$

The calculated room-temperature $\lambda_{\|}$ of SLs as a function of a/b ratio is plotted in Figure 7.6(c). $\lambda_{\|}$ of SLs decreases with a/b as $\lambda_{SPTO} < \lambda_{STNO}$. If the electronic contribution (λ_e) to λ is calculated using Wiedemann-Franz relation $\lambda_e = L_0 \sigma T$, where L_0 is Lorenz number (taken as 2.45×10^{-8} W Ω K^{-2}) [47], it is possible to calculate the lattice contribution (λ_l) to λ using the relation $\lambda_l = \lambda - \lambda_e$. The calculated values of λ_l show that STNO film (0.82 W m^{-1} K^{-1}) has lower λ_l than SPTO film (2.28 W m^{-1} K^{-1}) which can be attributed to the higher dopant concentration in STNO than SPTO, which act as phonon scattering centers. Usually, λ_l of crystalline films decreases at temperatures above Debye temperature (θ_D=513 K for STO) [48], and hence, by applying σ values to Wiedemann-Franz law and using the room-temperature λ_l, one can extract a higher estimate to the total thermal conductivity of all samples at high temperatures. In fact, the actual λ_l will be even lower, if the scattering of the long-wavelength phonons [39, 40] at the interfaces of the alternative SPTO and STNO layers in SLs structure is also taken into account [44]. It has been reported [23] that even flat interfaces in SLs can induce more scattering events in the in-plane heat flow compared to perfect epitaxial films or single crystal bulk materials without interfaces. Therefore, a lower estimate of ZT dependence on T can be found, by taking the calculated values of $\lambda_{\parallel}$, and it is plotted in Figure 7.7(a). It is worthy to note that SLs (3–5) exhibit ZT values higher than STNO film, which demonstrates the advantage of using SLs over single films (SPTO and STNO) in enhancing the TE performance of STO system. A maximum ZT of 0.46 was obtained, for SL3, at 1000 K. Figure 7.7(b) shows a timeline of the maximum reported ZT of STO-based materials (including bulk, thin films, and SLs) in the past decade along with the present value we obtained.

Table 7.1. Measured and calculated transport properties along with the lattice constants of SPTO, STNO films, and $[\mathrm{SPTO}_a|\mathrm{STNO}_b]_{20}$ SLs. All properties are found at 300 K unless it is stated.

Sample	Structure	Layers ratio a/b	Lattice constant (Å)	$\boldsymbol{\sigma}$ (S cm^{-1})	$\lvert\boldsymbol{S}\rvert$ (μV K^{-1})	$\boldsymbol{PF}$ (W K^{-1} m^{-1})	λ (W K^{-1} m^{-1})	ZT	$ZT_{1000\ \mathrm{K}}$
SPTO	film	-	3.906	18	221	0.03	2.29	0.01	0.01
SL1	$[\mathrm{SPTO}_8\vert\mathrm{STNO}_2]_{20}$	4	3.925	160	112	0.06	2.48	0.02	0.06
SL2	$[\mathrm{SPTO}_8\vert\mathrm{STNO}_5]_{20}$	1.6	3.937	1806	75	0.21	2.67	0.08	0.26
SL3	$[\mathrm{SPTO}_8\vert\mathrm{STNO}_8]_{20}$	1	3.942	2586	61	0.29	2.85	0.11	0.46
SL4	$[\mathrm{SPTO}_5\vert\mathrm{STNO}_8]_{20}$	0.63	3.951	2776	60	0.31	3.04	0.1	0.44
SL5	$[\mathrm{SPTO}_2\vert\mathrm{STNO}_8]_{20}$	0.25	3.956	2983	58	0.32	3.23	0.1	0.43
STNO	film	-	3.960	3504	52	0.29	3.42	0.09	0.43

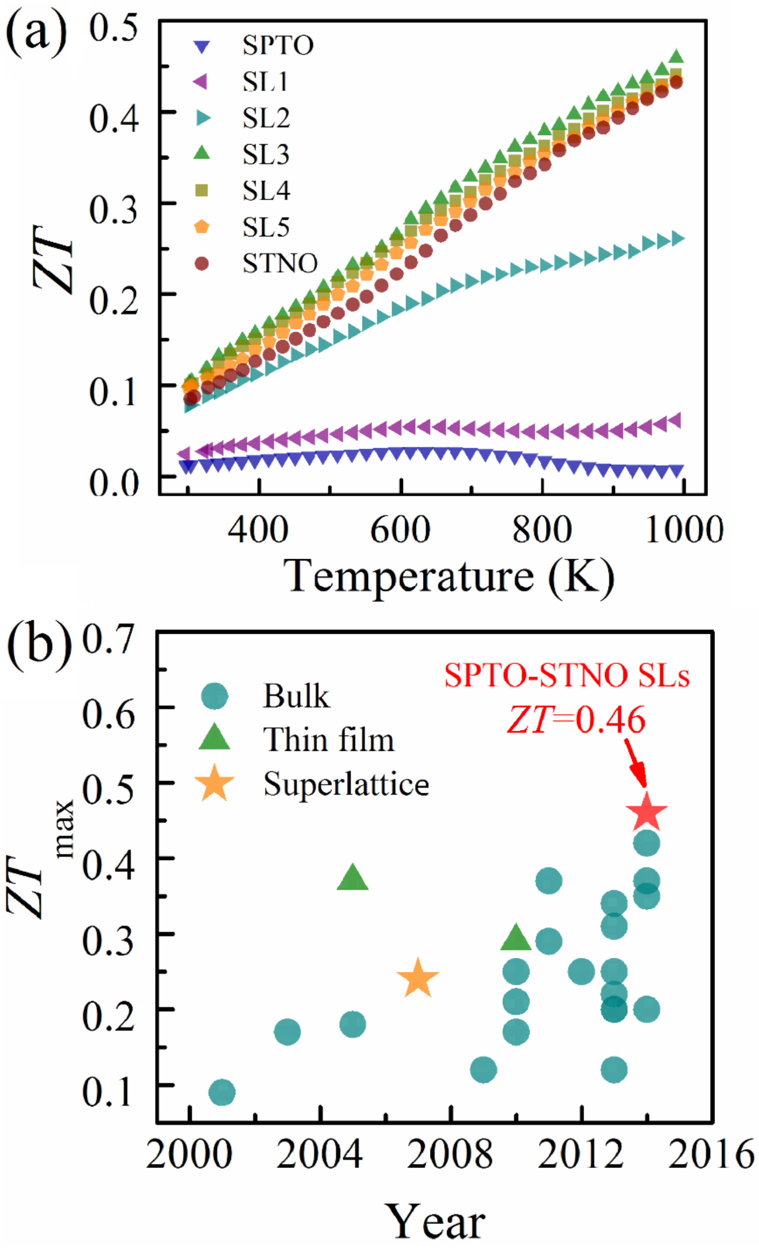

Figure 7.7. (a) Thermoelectric figure of merit of films and SLs as a function of temperature. (b) A timeline of the maximum values of figure of merit for STO systems known up to date,[11, 14, 34, 38, 49-68] SPTO-STNO SLs exhibit the best ***ZT*** of 0.46 as compared to other STO systems.

7.5 Conclusions

We report the thermoelectric properties of epitaxial Pr^{3+} and Nb^{5+} doped $SrTiO_{3-\delta}$ superlattices on $LaAlO_3$ substrate. Excellent thermal stability of the superlattices is demonstrated by preserving the crystal structure and reproducing the thermoelectric properties after 20 hours of measurements in Ar/H_2 ambient at a high temperature of 1000 K. An upper limit of in-plane thermal conductivity of superlattices is calculated from the thermal conductivities of SPTO and STNO single films by applying the continuum analysis. The superlattice which is composed of 20 $Sr_{0.95}Pr_{0.05}TiO_{3-\delta}/SrTi_{0.8}Nb_{0.2}O_{3-\delta}$ pairs, 8 unit cells of each layer, exhibits the best ZT of 0.46 at 1000 K compared to other $SrTiO_3$-based materials. The strategy of introducing oxygen vacancies as well as different extrinsic dopants (Pr^{3+} and Nb^{5+}), with different masses and ionic radii, at different lattice sites in SPTO and STNO layers, respectively, results in a substantial reduction of thermal conductivity via scattering a wider range of phonon spectrum without limiting the electrical transport and thermopower, and hence leading to an enhancement in the figure of merit (ZT).Our work demonstrates the importance of nano-structuring and rational design of SLs in improving ZT of metal oxides which are useful for high temperature energy harvesting applications.

7.6 References

1. H.J. Goldsmid, *"Theory of Thermoelectric Refrigeration and Generation"*, Springer Berlin Heidelberg, 7-21 (2010).
2. T.M. Tritt and M.A. Subramanian,*"Thermoelectric Materials, Phenomena, and Applications: A Bird's Eye View",* MRS Bulletin, 31, 188 (2006).
3. L.-D. Zhao, S.-H. Lo, Y. Zhang, H. Sun, G. Tan, C. Uher, C. Wolverton, V.P. Dravid, and M.G. Kanatzidis,*"Ultralow thermal conductivity and high thermoelectric figure of merit in SnSe crystals",* Nature, 508, 373 (2014).
4. K. Biswas, J. He, I.D. Blum, C.-I. Wu, T.P. Hogan, D.N. Seidman, V.P. Dravid, and M.G. Kanatzidis,*"High-performance bulk thermoelectrics with all-scale hierarchical architectures",* Nature, 489, 414 (2012).
5. H. Ohta,*"Thermoelectrics based on strontium titanate",* Materials Today, 10, 44 (2007).
6. D.G. Schlom, L.-Q. Chen, X. Pan, A. Schmehl, and M.A. Zurbuchen,*"A Thin Film Approach to Engineering Functionality into Oxides",* Journal of the American Ceramic Society, 91, 2429 (2008).
7. K. van Benthem, C. Elsässer, and R.H. French,*"Bulk electronic structure of $SrTiO_3$: Experiment and theory",* Journal of Applied Physics, 90, 6156 (2001).
8. B. Jalan and S. Stemmer,*"Large Seebeck coefficients and thermoelectric power factor of La-doped $SrTiO_3$ thin films",* Applied Physics Letters, 97, 042106 (2010).
9. J. Son, P. Moetakef, B. Jalan, O. Bierwagen, N.J. Wright, R. Engel-Herbert, and S. Stemmer,*"Epitaxial $SrTiO_3$ films with electron mobilities exceeding 30,000 $cm^2 V^{-1} s^{-1}$",* Nat Mater, 9, 482 (2010).
10. R. Moos and K.H. Härdtl,*"Electronic transport properties of $Sr_{1-x}La_xTiO_3$ ceramics",* Journal of Applied Physics, 80, 393 (1996).
11. S. Ohta, T. Nomura, H. Ohta, M. Hirano, H. Hosono, and K. Koumoto,*"Large thermoelectric performance of heavily Nb-doped $SrTiO_3$ epitaxial film at high temperature",* Applied Physics Letters, 87, 092108 (2005).
12. R. Perez-Casero, J. Perrière, A. Gutierrez-Llorente, D. Defourneau, E. Millon, W. Seiler, and L. Soriano,*"Thin films of oxygen-deficient perovskite phases by pulsed-laser ablation of strontium titanate",* Physical Review B, 75, 165317 (2007).
13. H. Muta, K. Kurosaki, and S. Yamanaka,*"Thermoelectric properties of reduced and La-doped single-crystalline $SrTiO_3$",* Journal of Alloys and Compounds, 392, 306 (2005).
14. H. Ohta, S. Kim, Y. Mune, T. Mizoguchi, K. Nomura, S. Ohta, T. Nomura, Y. Nakanishi, Y. Ikuhara, M. Hirano, H. Hosono, and K. Koumoto,*"Giant thermoelectric Seebeck coefficient of a two-dimensional electron gas in $SrTiO_3$",* Nat Mater, 6, 129 (2007).
15. R. Venkatasubramanian,*"Lattice thermal conductivity reduction and phonon localizationlike behavior in superlattice structures",* Physical Review B, 61, 3091 (2000).

16. Y. Kinemuchi, K.-i. Mimura, A. Towata, and K. Kato,*"Thermoelectric Properties of Rare Earth-Doped $SrTiO_3$ Nanocubes",* Journal of Electronic Materials, 42, 1 (2013).
17. H.C. N. Wang, H. He, W. Norimatsu, M. Kusunoki & K. Koumoto,*"Enhanced thermoelectric performance of Nb-doped $SrTiO_3$ by nano-inclusion with low thermal conductivity",* Scientific Reports, 3, 3449 (2013).
18. S.R.S. Kumar, M.N. Hedhili, D. Cha, T.M. Tritt, and H.N. Alshareef,*"Thermoelectric Properties of Strontium Titanate Superlattices Incorporating Niobium Oxide Nanolayers",* Chemistry of Materials, 26, 2726 (2014).
19. L. Kyu Hyoung, M. Yoriko, O. Hiromichi, and K. Kunihito,*"Thermal Stability of Giant Thermoelectric Seebeck Coefficient for $SrTiO_3$ /$SrTi_{0.8}Nb_{0.2}O_3$ Superlattices at 900 K",* Applied Physics Express, 1, 015007 (2008).
20. K.D. Coonley, B.C. O'Quinn, J.C. Caylor, and R. Venkatasubramanian,*"Thermal Stability of p-type Bi_2Te_3/Sb_2Te_3 and n-type $Bi_2Te_3/Bi_2Te_{2-x}Se_x$ Thermoelectric Superlattice Thin Film Devices",* MRS Online Proceedings Library, 793, Symposium S (2003).
21. C. Yu, M.L. Scullin, M. Huijben, R. Ramesh, and A. Majumdar,*"Thermal conductivity reduction in oxygen-deficient strontium titanates",* Applied Physics Letters, 92, 191911 (2008).
22. N.N. David A. Muller, Akira Ohtomo, John L. Grazul & Harold Y. Hwang,*"Atomic-scale imaging of nanoengineered oxygen vacancy profiles in $SrTiO_3$",* Nature, 430, 657 (2004).
23. G. Chen,*"Size and interface effects on thermal conductivity of superlattices and periodic Thin-film structures",* Journal of Heat Transfer, 119, 220 (1997).
24. D.G. Cahill,*"Thermal conductivity measurement from 30 to 750 K: the 3 omega method",* Review of Scientific Instruments, 61, 802 (1990).
25. T. Borca-Tasciuc, A.R. Kumar, and G. Chen,*"Data reduction in 3ω method for thin-film thermal conductivity determination",* Review of Scientific Instruments, 72, 2139 (2001).
26. X. Wang, Q. Hu, L. Li, and X. Lu,*"Effect of Pr substitution on structural and dielectric properties of $SrTiO_3$",* Journal of Applied Physics, 112, 044106 (2012).
27. A. Duran, E. Martinez, J.A. Diaz, and J.M. Siqueiros,*"Ferroelectricity at room temperature in Pr-doped $SrTiO_3$",* Journal of Applied Physics, 97, 104109 (2005).
28. W. Luo, W. Duan, S.G. Louie, and M.L. Cohen,*"Structural and electronic properties of n-doped and p-doped $SrTiO_3$",* Physical Review B, 70, 214109 (2004).
29. R.D. Shannon,*"Revised effective ionic radii and systematic studies of interatomic distances in halides and chalcogenides",* Acta Crystallographica Section A, 32, 751 (1976).
30. G.-z. Zhu, S. Lazar, A.P. Knights, and G.A. Botton,*"Atomic-level 2-dimensional chemical mapping and imaging of individual dopants in a phosphor crystal",* Physical Chemistry Chemical Physics, 15, 11420 (2013).

31. S. Lee, G. Yang, R.H.T. Wilke, S. Trolier-McKinstry, and C.A. Randall,*"Thermopower in highly reduced n-type ferroelectric and related perovskite oxides and the role of heterogeneous nonstoichiometry",* Physical Review B, 79, 134110 (2009).
32. D. Zou, Y. Liu, S. Xie, J. Lin, and J. Li,*"Effect of strain on thermoelectric properties of* $SrTiO_3$*: First-principles calculations",* Chemical Physics Letters, 586, 159 (2013).
33. P. Pichanusakorn and P. Bandaru,*"Nanostructured thermoelectrics",* Materials Science and Engineering: R: Reports, 67, 19 (2010).
34. S. Ohta, T. Nomura, H. Ohta, and K. Koumoto,*"High-temperature carrier transport and thermoelectric properties of heavily La- or Nb-doped* $SrTiO_3$ *single crystals",* Journal of Applied Physics, 97, 034106 (2005).
35. S.R.S. Kumar, A.Z. Barasheed, and H.N. Alshareef,*"High Temperature Thermoelectric Properties of Strontium Titanate Thin Films with Oxygen Vacancy and Niobium Doping",* ACS Applied Materials & Interfaces, 5, 7268 (2013).
36. P. Fan, Z.-h. Zheng, Z.-k. Cai, T.-b. Chen, P.-j. Liu, X.-m. Cai, D.-p. Zhang, G.-x. Liang, and J.-t. Luo,*"The high performance of a thin film thermoelectric generator with heat flow running parallel to film surface",* Applied Physics Letters, 102, 033904 (2013).
37. R. Funahashi, S. Urata, K. Mizuno, T. Kouuchi, and M. Mikami,*"*$Ca_{2.7}Bi_{0.3}Co_4O_9/La_{0.9}Bi_{0.1}NiO_3$ *thermoelectric deviceswith high output power density",* Applied Physics Letters, 85, 1036 (2004).
38. T. Okuda, K. Nakanishi, S. Miyasaka, and Y. Tokura,*"Large thermoelectric response of metallic perovskites:* $Sr_{1-x}La_xTiO_3$*",* Physical Review B, 63, 113104 (2001).
39. Z. Zheng, X. Chen, B. Deng, A. Chernatynskiy, S. Yang, L. Xiong, and Y. Chen,*"Phonon thermal transport through tilt grain boundaries in strontium titanate",* Journal of Applied Physics, 116, 073706 (2014).
40. N. Choudhury, E. Walter, A. Kolesnikov, and C.-K. Loong,*"Large phonon band gap in perovskites: First-principles lattice dynamics and inelastic neutron scattering",* Physical Review B, 77, 134111 (2008).
41. P.-P. Shang, B.-P. Zhang, Y. Liu, J.-F. Li, and H.-M. Zhu,*"Preparation and Thermoelectric Properties of La-Doped* $SrTiO_3$ *Ceramics",* Journal of Electronic Materials, 40, 926 (2011).
42. H.C. Wang, C.L. Wang, W.B. Su, J. Liu, Y. Zhao, H. Peng, J.L. Zhang, M.L. Zhao, J.C. Li, N. Yin, and L.M. Mei,*"Enhancement of thermoelectric figure of merit by doping Dy in* $La_{0.1}Sr_{0.9}TiO_3$ *ceramic",* Materials Research Bulletin, 45, 809 (2010).
43. O. Dong-Wook, J. Ravichandran, C.-W. Liang, W. Siemons, B. Jalan, C.M. Brooks, M. Huijben, D.G. Schlom, S. Stemmer, L.W. Martin, A. Majumdar, R. Ramesh, and D.G. Cahill,*"Thermal conductivity as a metric for the crystalline quality of SrTiO3 epitaxial layers",* Applied Physics Letters, 98, 221904 (2011).

44. K. Termentzidis, P. Chantrenne, and P. Keblinski,*"Nonequilibrium molecular dynamics simulation of the in-plane thermal conductivity of superlattices with rough interfaces",* Physical Review B, 79, 214307 (2009).
45. J.O. Sofo and G.D. Mahan,*"Thermoelectric figure of merit of superlattices",* Applied Physics Letters, 65, 2690 (1994).
46. V.B. Antonyuk, A.G. Mal'shukov, Z. Ma, and K.A. Chao,*"Thermoelectric figure of merit for parallel transport in superlattices",* Applied Physics Letters, 79, 3791 (2001).
47. E. Flage-Larsen and Ø. Prytz,*"The Lorenz function: Its properties at optimum thermoelectric figure-of-merit",* Applied Physics Letters, 99, 202108 (2011).
48. M. Ahrens, R. Merkle, B. Rahmati, and J. Maier,*"Effective masses of electrons in n-type $SrTiO_3$ determined from low-temperature specific heat capacities",* Physica B: Condensed Matter, 393, 239 (2007).
49. G.H. Zheng, Z.X. Dai, H.B. Li, H.Q. Wang, Y.Q. Li, X.F. Xu, B.T. Huang, Y.Q. Ma, and G. Li,*"Improving the Thermoelectric Properties of $Sr_{0.9}La_{0.1}TiO_3$ by Ag Addition",* Journal of Low Temperature Physics, 174, 128 (2014).
50. L. Li, Y. Liu, X. Qin, D. Li, J. Zhang, C. Song, and L. Wang,*"Enhanced thermoelectric performance of highly dense and fine-grained $(Sr_{1-x}Gd_x)TiO_{3-\delta}$ ceramics synthesized by sol–gel process and spark plasma sintering",* Journal of Alloys and Compounds, 588, 562 (2014).
51. G.H. Zheng, Z.H. Yuan, Z.X. Dai, H.Q. Wang, H.B. Li, Y.Q. Ma, and G. Li,*"Improvement of the Thermoelectric Properties of $(Sr_{0.9}La_{0.1})_3Ti_2O_7$ by Ag Addition",* Journal of Low Temperature Physics, 173, 80 (2013).
52. Y. Wang, C. Wan, X. Zhang, L. Shen, K. Koumoto, A. Gupta, and N. Bao,*"Influence of excess SrO on the thermoelectric properties of heavily doped $SrTiO_3$ ceramics",* Applied Physics Letters, 102, 183905 (2013).
53. T. Teranishi, Y. Ishikawa, H. Hayashi, A. Kishimoto, M. Katayama, and Y. Inada,*"Thermoelectric Efficiency of Reduced $SrTiO_3$ Ceramics Modified with La and Nb",* Journal of the American Ceramic Society, 96, 2852 (2013).
54. J. Liu, C.L. Wang, Y. Li, W.B. Su, Y.H. Zhu, J.C. Li, and L.M. Mei,*"Influence of rare earth doping on thermoelectric properties of $SrTiO_3$ ceramics",* Journal of Applied Physics, 114, 223714 (2013).
55. M.H. Lee, J.-S. Rhyee, M. Vaseem, Y.-B. Hahn, S.-D. Park, H. Jin Kim, S.-J. Kim, H.J. Lee, and C. Kim,*"Thermoelectric properties of $SrTiO_3$ nano-particles dispersed indium selenide bulk composites",* Applied Physics Letters, 102, 223901 (2013).
56. A.V. Kovalevsky, A.A. Yaremchenko, S. Populoh, A. Weidenkaff, and J.R. Frade,*"Enhancement of thermoelectric performance in strontium titanate by praseodymium substitution",* Journal of Applied Physics, 113, 053704 (2013).
57. F. Dang, C. Wan, N.-H. Park, K. Tsuruta, W.-S. Seo, and K. Koumoto,*"Thermoelectric Performance of $SrTiO_3$ Enhanced by Nanostructuring Self-Assembled Particulate Film of Nanocubes",* ACS Applied Materials & Interfaces, 5, 10933 (2013).

58. J. Liu, C.L. Wang, H. Peng, W.B. Su, H.C. Wang, J.C. Li, J.L. Zhang, and L.M. Mei,*"Thermoelectric Properties of Dy-Doped $SrTiO_3$ Ceramics",* Journal of Electronic Materials, 41, 3073 (2012).
59. H.C. Wang, C.L. Wang, W.B. Su, J. Liu, Y. Sun, H. Peng, and L.M. Mei,*"Doping Effect of La and Dy on the Thermoelectric Properties of $SrTiO_3$",* Journal of the American Ceramic Society, 94, 838 (2011).
60. H.C. Wang, C.L. Wang, W.B. Su, J. Liu, H. Peng, Y. Sun, J.L. Zhang, M.L. Zhao, J.C. Li, N. Yin, and L.M. Mei,*"Synthesis and thermoelectric performance of Ta doped $Sr_{0.9}La_{0.1}TiO_3$ ceramics",* Ceramics International, 37, 2609 (2011).
61. Y. Wang, K. Lee, H. Hyuga, H. Kita, H. Ohta, and K. Koumoto,*"Enhancement of thermoelectric performance in rare earth-doped $Sr_3Ti_2O_7$ by symmetry restoration of TiO_6 octahedra",* Journal of Electroceramics, 24, 76 (2010).
62. N. Wang, H. Li, Y. Ba, Y. Wang, C. Wan, K. Fujinami, and K. Koumoto,*"Effects of YSZ Additions on Thermoelectric Properties of Nb-Doped Strontium Titanate",* Journal of Electronic Materials, 39, 1777 (2010).
63. N. Wang, L. Han, H. He, Y. Ba, and K. Koumoto,*"Effects of mesoporous silica addition on thermoelectric properties of Nb-doped $SrTiO_3$",* Journal of Alloys and Compounds, 497, 308 (2010).
64. J. Ravichandran, W. Siemons, D.W. Oh, J.T. Kardel, A. Chari, H. Heijmerikx, M.L. Scullin, A. Majumdar, R. Ramesh, and D.G. Cahill,*"High-temperature thermoelectric response of double-doped $SrTiO_3$ epitaxial films",* Physical Review B, 82, 165126 (2010).
65. Y. Wang, K.H. Lee, H. Ohta, and K. Koumoto,*"Thermoelectric properties of electron doped $SrO(SrTiO_3)_n(n=1,2)$ ceramics",* Journal of Applied Physics, 105, 103701 (2009).
66. H. Muta, K. Kurosaki, and S. Yamanaka,*"Thermoelectric properties of rare earth doped $SrTiO_3$",* Journal of Alloys and Compounds, 350, 292 (2003).
67. A.M. Dehkordi, S. Bhattacharya, J. He, H.N. Alshareef, and T.M. Tritt,*"Significant enhancement in thermoelectric properties of polycrystalline Pr-doped $SrTiO_{3-\delta}$ ceramics originating from nonuniform distribution of Pr dopants",* Applied Physics Letters, 104, 193902 (2014).
68. A.V. Kovalevsky, A.A. Yaremchenko, S. Populoh, P. Thiel, D.P. Fagg, A. Weidenkaff, and J.R. Frade,*"Towards a high thermoelectric performance in rare-earth substituted $SrTiO_3$: effects provided by strongly-reducing sintering conditions",* Physical Chemistry Chemical Physics, 16, 26946 (2014).

Chapter 8.

Summary and Future Perspectives

In this chapter, the main conclusions and achievements of this work are summarized. There are some remaining challenges that need to be studied and solved in order to establish a complete understanding of TE properties of oxide thin films, and to improve research in this direction. Furthermore, the chapter discusses the future perspectives that could be done to enhance the TE properties of oxide thin films. This dissertation highlights the potential of TE oxides in energy harvesting applications from waste heat recovery at high temperatures. After optimizing their TE performance, oxides are expected to replace the heavy-metal-alloys, the traditional TE materials, since oxides are non-toxic, abundant, and stable in high temperature regimes. A comprehensive study of oxide (STO and ZnO) thin films and superlattices by PLD has been done, and several approaches were followed in order to improve their TE performance.

The fundamentals of TEs and recent progress in the field were presented. All physical parameters which describe *ZT* were discussed to understand the main factors lead to higher TE efficiency. Time-evolution of *ZT* in the past six decades was presented, and a comprehensive literature review on TE research done on STO and ZnO was collected. Afterword, the experimental procedures used in the fabrication and characterization of thin films and superlattices were discussed. The experimental setup used for measuring the electrical conductivity, Seebeck coefficient, thermal conductivity, and carrier concentration was also discussed. The main characterization tools used in this work were presented.

It was shown that the laser fluence in PLD process determine the TE properties of the La^{3+} doped $SrTiO_3$ (SLTO) thin films. XRD patterns obtained from these films confirm that the films are epitaxially grown on LAO substrate. Furthermore, it was concluded that oxygen vacancies can be tuned by varying the fluence of the ablating laser. The concentration of oxygen vacancies plays a vital role in determining the TE properties of the films. Film grown at highest laser fluence (7 J cm^{-2} $pulse^{-1}$) exhibits the highest TE power factor.

It was also demonstrated that the TE properties of highly oriented Al^{3+} doped zinc oxide (AZO) thin films can be improved by controlling their crystal orientation. The crystal orientation of the AZO films is changed by changing the temperature of the laser deposition process on LAO <001> substrates. The change in surface termination of the LAO substrate with temperature induces a change in AZO film orientation. The anisotropic nature of electrical conductivity and Seebeck coefficient in different crystal orientations of the AZO films shows a favored TE performance in c-axis oriented films.

The effect of additional B-site doping to A-site doped STO on the TE properties of epitaxial STO films was presented. The additional B-site doping enhances the electrical conductivity, but at the expense of Seebeck coefficient. However, introducing different dopants on both sites of the STO, with different masses and ionic radii, reduces the lattice thermal conductivity of STO significantly by adding more densely and strategically distributed phononic scattering centers that attack a wider phonon spectra. The additional B-site doping limits the trade-off relationship between electrical conductivity and total thermal conductivity of A-site doped STO, leading to an improvement in room-temperature thermoelectric figure of merit, ZT.

Finally, the TE properties of STO superlattices, composed from alternative layers of Pr^{3+} doped $SrTiO_{3-\delta}$ (SPTO) and Nb^{5+} doped $SrTiO_{3-\delta}$ (STNO) fabricated by PLD, were presented. Excellent stability is established for these superlattices by maintaining the crystal structure and reproducing the TE properties after long-time (20 hours) annealing at high temperature (~1000 K). The introduction of oxygen vacancies as well as extrinsic dopants (Pr^{3+} and Nb^{5+}), with different masses and ionic radii, at different lattice sites in SPTO and STNO layers, respectively, results in a substantial reduction of thermal conductivity via scattering a wider range of phonon spectrum without limiting the electrical transport and thermopower, and hence leading to a prominent enhancement in ZT.

Several investigations can be performed in the future to further improve the TE properties of STO- and ZnO-based materials. For STO-based materials, one possible approach is to study the effect of double-doping on one lattice site of a doped STO material (e.g. Pr and La doped $SrTi_{0.8}Nb_{0.2}O_{3-\delta}$), and measure the corresponding change in the TE properties of STO films and superlattices. Introducing more extrinsic dopants may reduce the thermal conductivity more, and may improve the electrical conductivity at the same time, and hence improving ZT. For oxide superlattices, it would be interesting to study the effect of introducing different thicknesses of the constituting, alternative layers. Tuning the thicknesses of these layers controls the density of the interfaces, and hence more phonon modes could be scattered compared to the case of using one thickness value. In this approach, one may tune the total thermal conductivity of the superlattices as a function of interface density, and find the optimum condition for the lowest thermal conduction. Moreover, in oxide superlattices, it would be also motivating to discover the effect of incorporating more than one lattice type. For instance, (0001) oriented oxides with hexagonal lattice can be grown epitaxially with (111) oriented oxides with cubic lattice, which can facilitate the electrical transport due to epitaxy, and reduce lattice thermal conductivity by scattering phonons due to the presence of inhomogeneous lattices. Finally, investigating the above perspectives in oxide TE research requires suitable capabilities and instruments to properly measure all of the physical parameters needed for a good estimate of ZT.

ACCOMPLISHMENTS

List of Publications:

1. *"Laser energy tuning of carrier effective mass and thermopower in epitaxial La doped $SrTiO_3$ thin films"*
   AI Abutaha, SR Sarath Kumar, HN Alshareef
   Applied Physics Letters, 100, 162106 (2012)

2. *"Crystal orientation dependent thermoelectric properties of highly oriented Al doped ZnO thin films"*
   AI Abutaha, SR Sarath Kumar, HN Alshareef
   Applied Physics Letters, 102, 053507 (2013)

3. *"Doping-site dependent thermoelectric properties of epitaxial strontium titanate thin films"*
   AI Abutaha, S.R. Sarath Kumar, AM Dehkordi, TM Tritt, HN Alshareef
   Journal of Materials Chemistry C, 2, 9712 (2014)

4. *"Enhanced Thermoelectric Figure of Merit in Thermally Robust, Nanostructured Superlattices based on $SrTiO_3$"*
   AI Abutaha, S.R. Sarath Kumar, Kun Li, AM Dehkordi, TM Tritt, HN Alshareef
   Chemistry of Materials, 27, 2165 (2015)

5. *"Integrating Carbon Nanotubes to Silicon by means of Vertically Aligned Carbon Nanotube Field-effect Transistors"*
   Jingqi Li, Qingxiao Wang, Weisheng Yue, Zaibing Guo ; LIANG LI, Chao Zhao Xianbin Wang; **AI Abutaha**, H. N. Alshareef, Xixiang Zhang
   Nanoscale, 6, 8956 (2014)

6. *"Modeling the transport properties of epitaxially grown thermoelectric oxide thin films using spectroscopic ellipsometry"*
   SR Sarath Kumar, **AI Abutaha**, MN Hedhili, HN Alshareef
   Applied Physics Letters, 100, 052110 (2012)

7. *"Effect of oxygen vacancy distribution on the thermoelectric properties of La doped $SrTiO_3$ epitaxial thin films"*
   SR Sarath Kumar, **AI Abutaha**, MN Hedhili, HN Alshareef
   Journal of Applied Physics, 112, 115104 (2012)

8. *"Vertically aligned carbon nanotube field-effect transistors"*
   Jingqi Li, C Zhao, Q Wang, Q Zhang, Z Wang, X Zhang, **AI Abutaha**, HN Alshareef
   Carbon, 50, 4628 (2012)

Conferences:

- *"Laser energy tuning of carrier effective mass and thermopower in epitaxial La doped $SrTiO_3$ thin films"* (Poster)
  Materials Research Society (MRS) Fall Meeting and Exhibit, Boston, USA (Nov 25–30, 2012)
  AI Abutaha, SR Sarath Kumar, HN Alshareef

- *"Crystal Orientation dependent thermoelectric properties of highly oriented Al doped ZnO thin films"* (Oral Presentation)
  International Conference on Thermoelectrics (ICT), Kobe, Japan (Jun 29–July 4, 2013)
  AI Abutaha, S.R. Sarath Kumar, and H. N. Alshareef

- *"Enhanced thermoelectric properties of $SrTiO_3$-based superlattices"*
  Materials Research Society (MRS) Fall Meeting and Exhibit, Boston, USA (Nov 30–Dec 5, 2014)
  AI Abutaha, SR Sarath Kumar, HN Alshareef

Awards:

- Dow Sustainability Innovation Student Challenge Award (SISCA) 2014
  1st place "Grand Prize Winner"

- Sustainability at my School 2014
  Competition held in Materials Research Society (MRS) Fall Meeting
  3rd place